PRECISE POSITIONING USING THE ELECTROSTATIC GLASS MOTOR

THÈSE N^{O} 2638 (2002)

PRÉSENTÉE À LA FACULTÉ SCIENCES ET TECHNIQUES DE L'INGÉNIEUR

SECTION DE MICROTECHNIQUE

ÉCOLE POLYTECHNIQUE FÉDERALE DE LAUSANNE

POUR L'OBTENTION DU GRADE DE DOCTEUR ÈS SCIENCES TECHNIQUES

PAR

Roland MOSER

ingénieur en microtechnique diplômé EPF
de nationalité suisse et originaire d'Untereggen (SG)

acceptée sur proposition du jury:

Prof. H. Bleuler, directeur de thèse
Dr A. Cassat, rapporteur
Prof. N. de Rooij, rapporteur
Prof. T. Higuchi, rapporteur
Prof. M. Jufer, rapporteur

Lausanne, EPFL
2002

Meinen Eltern in Dankbarkeit

Acknowledgements

First of all, I would like to thank my thesis director Prof. Dr. Hannes Bleuler for the confidence he placed in me by accepting me as his doctoral student, and for the independence I enjoyed during my stay at his laboratory.
I am deeply obliged to Prof. Dr. Toshiro Higuchi from the University of Tokyo for the hospitality I enjoyed at his laboratory during one year and for the fruitful discussions about electrostatic glass motors, which made this thesis possible.

I am grateful to the other members of the thesis jury, Prof. Dr. Marcel Jufer, Prof. Dr. Nico de Rooij and Dr. Alain Cassat for their interest, time and valuable comments.

I would like to thank everyone at the Bleuler-lab who made these three years so enjoyable and contributed through suggestions, long discussions and diploma / semester projects.

Thank you to Julieanne Kohler for the correction of the English text.

And, last but not least, thanks to the members of the atelier. They did many pieces for me, always in excellent quality and in due time.

The present thesis would not have been possible without the generous support of the Japanese education ministry and the Gebert-Rüf foundation (Basel, Switzerland).

Abstract

Precise positioning over a long stroke is required in various fields. Important advances in the field of electromagnetic motors, piezoelectric actuators and bearing technology allow nanometric and sub-arc-second resolution for linear or rotary actuators, respectively. Alas, these devices are rather complex, therefore expensive, and require sophisticated assembly techniques for the delicate components. Furthermore, their operation range is often limited to some fractions of a millimeter or a couple of degrees.

For some applications the stiffness of the positioning stage is of minor importance. Compactness, cost-effectiveness (simple structure), ripple-free displacements and rotations and the absence of magnetic fields are the design objectives. Potential applications requiring such specifications are typically the positioning of optical elements such as mirrors and lenses and the handling of wafers during electron-beam operations.

This thesis presents a novel approach to precise positioning, by exploiting the electrical properties of glasses. Charges are arranged via application of an electrostatic field. This polarization has an extraordinary long rise and decay time constant in the order or several tens of seconds and can be used to drive the glass. It was verified experimentally that what we call the 'electrostatic glass motor' is operating at the speed of the applied field, although being a kind of induction motor. It features a perfect ripple-free movement over a very broad speed range. The precision of the movement depends on the resolution of the motor field generator and is entirely decoupled form mechanical precision aspects.

In the present report, the principle of the electrostatic glass motor is presented. An analytical model, describing the forces and torques of such motors is proposed and verified experimentally. A rotary positioning device, allowing sub-arc second open loop resolution has been designed, realized and characterized. An open-loop resolution of 0.3 arc-seconds and a speed range ranging from 40 rpm down to 0.3 arc-sec/sec, and this over an unlimited displacement range, indicate the promising potential of the presented concept.

Models and design rules for electrostatic glass positioning devices have been established and allow, within the scope of future works, the definitions of linear and multi-axis devices.

Résumé

Le positionnement précis sur une grande plage est requis dans de multiples champs d'applications. D'importantes avancées dans le domaine des moteurs électromagnétiques, piézoélectriques et des paliers permettent des résolutions nanométriques ou 'sub-arc secondique' pour des déplacements linéaires ou rotatifs, respectivement. Jusqu'à présent, ces appareils sont plutôt complexes, donc chers, et demandent, pour les composants délicats, des techniques d'assemblage sophistiquées. En plus, leur plage d'opération est souvent limitée à quelques fractions de millimètre ou quelques degrés.

Pour certaines applications, la rigidité du stage de positionnement n'est pas d'une importance primordiale. Une structure compacte et simple (donc potentiellement bon marché), un déplacement lisse sans sauts et l'absence de champs magnétiques sont requis. Des applications potentielles qui appellent à de telles spécifications sont typiquement le positionnement d'éléments optiques comme des miroirs et des lentilles, et la manipulation des wafers pendant le traitement par faisceau d'électrons.

Cette thèse présente une nouvelle conception du positionnement précis, en exploitant les propriétés électriques des verres. Des charges sont arrangées par application d'un champ électrostatique. Cette séparation des charges a une constante de décroissance extrêmement lente, de l'ordre de plusieurs dizaines de secondes et va être utilisé pour entraîner le verre. Il a été vérifié éxperimentalement que ce qu'on appèle un 'moteur électrostatique en verre' fonctionne d'une manière synchrone avec la vitesse du champ appliqué. Son mouvement est parfaitement lisse, ne présent aucune irrégularité, et ceci sur une plage de vitesse très vaste. La précision du mouvement dépend de la résolution du champ statorique et est ainsi totalement découplée des aspects des tolérances mécaniques. Dans le présent rapport, le principe du moteur électrostatique en verre est présenté. Un modèle analytique décrivant les forces et couples d'un tel moteur est proposé et vérifié expérimentalement. Un appareil de positionnement rotatif permettant une résolution au-dessous de l'arc seconde en boucle ouverte a été conçu, réalisé et caractérisé. Une résolution en boucle ouverte de 0.3 arc-seconde et une plage de vitesse de 40 rpm jusqu'à 0.3 arc-sec/sec, indique le potentiel prometteur du concept présenté.

Contents

I. Introduction

1.1 Motivation

This thesis aims to provide a detailed description of electrostatic glass motors and their application to precise positioning. The term 'precise positioning' is understood nowadays to refer to resolutions less than one micrometer (10^{-6}m) for linear displacements and under one arc-second ($2{,}78 \cdot 10^{-4}$ degree) for rotations.

Electrostatic glass motors are an exciting new actuator concept of stunning simplicity and utmost interest for various concrete applications. The physical effect of non-contact induction of charges with a very long time constant in the order of minutes or hours on glass is well known and manifests itself as 'absorption current' during charging of a glass-capacitor [37]. However, the idea to use induced charges to move a glass object is quite recent. Higuchi [46]-[48] proposed various concepts for active electrostatic contact-less levitation of glass plates, as well as levitation combined with propulsion and fast rotation of disc shaped glass rotors. The observations of the progressive propulsion smoothness (due to the charge dynamics) and the remarkably broad speed range led to the idea to use the electrostatic glass motor for positioning purposes, the starting point of the present thesis.

The challenge is twofold: First, the electrostatic glass motor has to be 'understood'. A model satisfactorily close to reality has to be established in order to allow the design of the final actuator. This model is, by preference, analytical. Given the highly complex structure of glasses, the model is expected to be fitted by experimental data.

Second, based on the previous findings, an operational positioning actuator has to be designed and realized. In consideration of the problems of linear actuators (impossibility to perform long time measurements), a rotary prototype is preferred. The commercially available driver electronics composed of high voltage amplifiers and function generators are prohibitively expensive and encumbering and need to be redeveloped in order to obtain one compact bench-top device. The actuator is supposed to be controlled by a commercial PC without any additional hardware, so driver software and communication between computer and actuator have to be developed as well.

1.2 Structure of the thesis

Chapter 1, the introduction, describes the state of the art in precise rotary positioning and reviews the historical development and physical principle of electrostatic actuation. The related scale laws and the Paschen-effect are discussed as well.

Chapter 2 presents the physics of electrostatic glass motors. The special dielectric properties of glasses, properties that are responsible for the functioning of electrostatic glass motors are discussed, leading to a description of the obtainable motor forces. The structure of electrostatic glass motors that transform these forces into linear and rotary movements and the resulting synchronous movement are explained.

An analytical model of the actuator is proposed in Chapter 3, describing all involved forces and torques. Analytical simplification provides a more compact design-tool and a good approximation of the exact expression over the whole operation range.

Experimental verification of the analytical model is the topic of chapter 4, determining the experimental parameters that characterize the glass and that allow fitting the model to reality. Furthermore, the best glass blend and the optimal motor electrode were determined, as well as the influence of the humidity.

The verified model and the additional experimental characterizations allowed the design of a prototype, design that is explained in detail in chapter 5.

The realized prototype was successfully operated and its performances are presented in chapter 6.

The presented thesis is resumed and concluded in chapter 7, followed by a brief discussion of the future work.

1.3 State of the Art

1.3.1 Hydraulic and pneumatic actuators

One expects hydraulic and pneumatic actuators in big machines where the applied forces are relatively important. However, recently, these types of actuators have also been utilized for micro-mechanisms and precise positioning.

The main advantages of the hydraulic actuator are its high energy density and a very high rigidity. The German company Piezomechanik GmbH introduced an actuator featuring a resolution of 50nm over a range of 400μm. Figure 1.1 shows this manually actuated hydraulic micrometer screw:

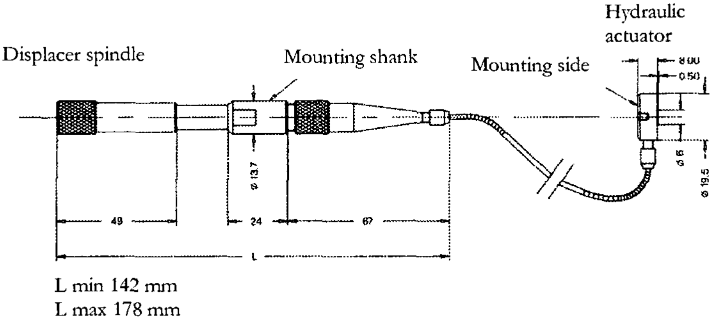

Figure 1.1 Hydrap actuator (Source: Website Piezomechanik GmbH)

Pneumatic actuators are normally reserved for full-range-mechanisms like robot-grippers. Badano et al. [4] achieved a sub-micrometric resolution over 2 mm range for multiple degrees of freedom due to important advances in adaptive nonlinear control of pressure dynamics in electro-pneumatic devices.

Higuchi et al. [58] recently proposed a novel pneumatic actuator, the air impact drive, in which the impact is generated by air pressure, allowing nanometric displacement of objects weighing several kilograms.

No rotary hydraulic or pneumatic positioning devices have been reported to date.

1.3.2 Electromechanical actuators

Electromechanical systems are definitively the most widely used solution. Their main advantages are the satisfactory performance, reliability and their availability. However, when dimensions are reduced and space is limited, they lose some of their interest. Their peak-performance being developed at high speed, most of the electromechanical actuators need gearboxes to obtain the necessary torque. Using a gearbox, the resolution becomes a function of the backlash and the flexibility of the transmission. As a typical example of electromagnetic stepper motor actuators, figure 1.2 shows two products from Melles Griot, a leading company in nano-positioning.

Figure 1.2 NANOROTOR and NANOROLL stepper motor actuators. The NANOROLL actuator owes its high resolution to an additional open loop piezo actuator. (Source: Website MELLES GRIOT Inc.)

Direct drives are another electromagnetic approach that successfully counters most of inconveniences of stepper motor actuators but they need additional position sensors, resulting in linear and rotary axes allowing sub-micrometric and sub-arc second positioning at very high speeds. Figure 1.3 shows the components of linear direct drives:

Figure 1.3 Principle of linear direct drive (Source: Website ETEL SA)

Voice coil actuators offer a very high resolution for linear displacements. They find wide applications in machine tools but are difficult to miniaturize.

1.3.3 Ultrasonic actuators

Ultrasonic actuators are friction-force actuators, like inchworm-actuators, impact-drive actuators and stick-and-slip actuators.

They are based on the generation of mechanical vibrations on the contact surface between stator and rotor. This vibration leads to a deformation of elliptic shape, which moves the rotor through friction with the stator. Figure 1.4 depicts the principle of rotary ultrasonic actuators and some commercially available stages from the German company Physik Instrumente.

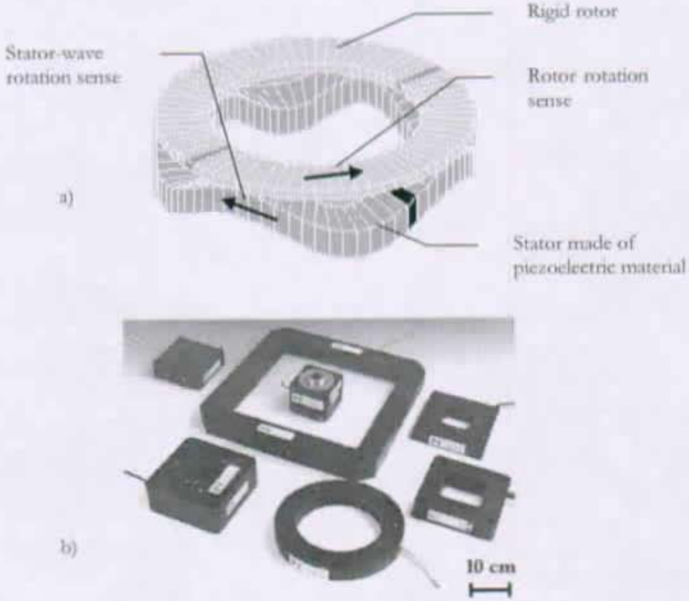

Figure 1.4 a) Principle of rotary ultrasonic motor drive b) Translation and rotation positioning stages (Source: Website Physik Instrumente)

The ring ultrasonic motor causes the stator to vibrate, creating energy that rotates the rotor. Piezoelectric ceramic elements, which expand and contract when voltage is applied are chosen for the stator material. The word "ultrasonic" derives from the frequency of the AC charge applied to the stator.

Ultrasonic rotary positioning devices are chosen when space is limited, a large torque is required and the operation speed is not too high.
Rotary ultrasonic actuators offer unlimited stroke, and blocking at rest in any position since the rotor is in tight contact with the stator by means of a preload. For linear actuators, velocity ranges from 0.01 mm/sec to 100 mm/sec for commercially available actuators. Load capacity ranges from 4 kg to 100 kg. For rotary actuators, sub-arc second resolution can be achieved when position feedback is used.
The most widely used ultrasonic motors feature the described progressive wave principle, as described by Osakabe [79]. They found commercial applications in the focusing of camera lenses, sold by the Japanese enterprise Canon. Other ways to generate an ellipsoidal movement have been proposed by Ragulskis [85], Péclat [83] and Ikuta [42], but are not adequate for miniaturization.

1.3.4 Inch-worm actuators

This type of 'walking' mechanism is constituted of three active parts, one for elongation and two for blocking. Figure 1.5 shows the principle:

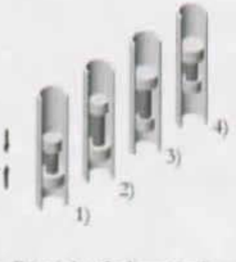

1) Blocking lower piezo
2) Elongation middle piezo
3) Blocking upper piezo
4) Retraction middle piezo

Figure 1.5 Principle of a linear inch-worm actuator. Δ indicates the displacement

Several experimental rotary setups have been proposed, for example by Bexell et al. [6]. Commercially available rotary actuators are sold by the American company Burleight.
Figure 1.6 shows one of their products, together with an experimental prototype for unlimited rotation range (Duong et al. [24]).
The performances of the Burleight product are: Rotation range of ±15°, resolution better than one 0.3 arc second. The rotary inchworm developed by Duong is capable of providing continuous and unlimited rotation. The maximum angular step is 0.37°. Maximum rotational

speed is 22.7 deg/s at 75 Hz operating frequency. The open loop resolution is 8 arc-seconds.

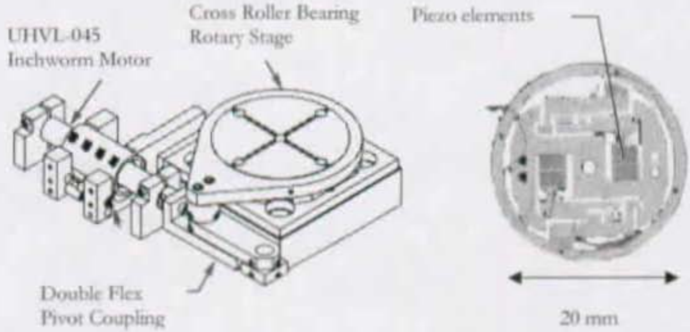

Figure 1.6 a) Burleight UHVL-RS Rotary Stage (Dimensions 175 x 75 x 35 mm) b) Unlimited rotary range inchworm actuator, experimental prototype

1.3.5 Impact drive actuators

These actuators are based on the force developed by an accelerated mass. Two unequal masses are suddenly elongated, and then slowly contracted. This movement asymmetry, together with friction, allows a step-by-step displacement. Figure 1.7 shows the principle:

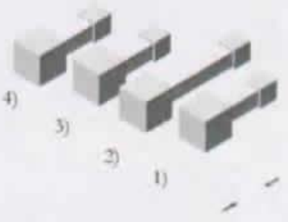

1) Start position
2) Rapid elongation, first displacement
3) Slow contraction, sudden stop
4) Final position

Figure 1.7 Principle of impact drive actuator

A number of variations of this actuation principle have been proposed. Rotary impact drive actuators are rarer, Büchi [12] proposed a micro-robot capable of moving in three degrees of freedom, including a rotation along its main axis. He used conventional linear impact actuators arranged in a triangle. Morita [71] developed a truly rotary impact drive using arc segmented piezo elements:

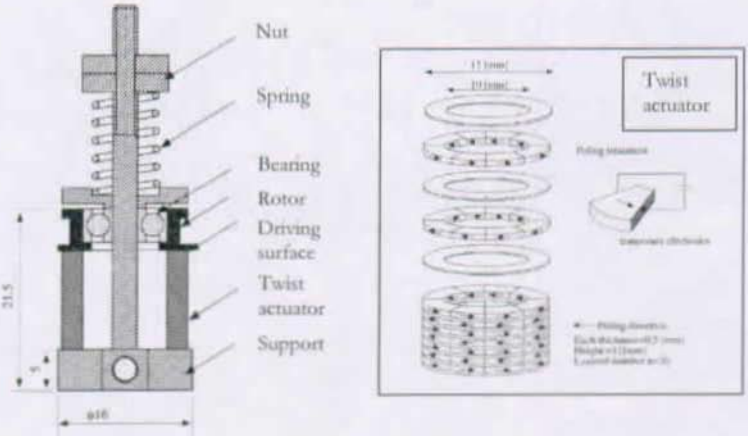

Figure 1.8 Rotary impact drive actuator

Revolution speed of this actuator is around 30 rpm and the resolution about one arc-second.

1.3.6 Stick and slip actuators

This principle can be seen as a special case of the impact drive actuator. In the case of the 'stick and slip', one of the two masses is zero or neglectable compared to the other one (see figure 1.7). Hack [35] proposed a rotary stick slip actuator with rotation top speeds under one rpm. The major disadvantage of stick slip actuators is the different behavior for forward and reverse motion and the need for polished surfaces to allow continuous and accurate motion.

All four presented friction-force actuators (ultrasonic, inch-worm, impact drive and stick-slip) have inherent tribological problems: They require a certain surface quality on rotor and stator and do wear.

1.3.7 Electrostatic actuators

Since the present thesis deals with a kind of electrostatic actuator, the state of the art and some historical aspects are discussed in more detail than in the previously presented actuation principles.

Experiments with electrostatic machines date back to the early days of occidental renaissance research efforts. The first reported 'machine' was realized by Otto von Guericke in 1663 [34] (he also performed the famous 'Magdeburg-experiment' on vacuum) and consisted of a sulphur globe frictioned by hand which could be removed and used as a charge source for electrostatic experiments.
Relative recent historical researches confirm that the discovery of electric conduction should be bestowed to Stephen Gray (1667 – 1736), whose extraordinary experimental results have been partly suppressed by Isaac Newton, the president of the royal academic society, for mainly personal reasons [16].
Generation of charges was the main objective for the following two centuries and resulted in sophisticated generators, powered by water or manpower to generate high voltages. Figure 1.9 shows some milestones of early electrostatic engineering:

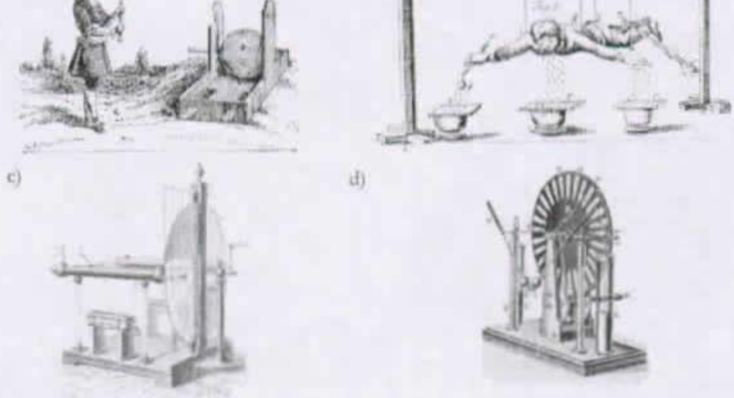

Figure 1.9 a) von Guericke's charged ball (1663) b) One of Gray's conduction experiments (1779) c) Ramsden friction machine (1766) d) Wimshurst machine (1882)

Gray observed electric conductivity through silk threads. He even went as far as to suspend pupils of the house by cords and electrified them, sometimes even drawing sparks from the human body. Figure 1.9b shows that the electric force of a rubbed glass could be sent, through a wire, to the body of a person.

Jesse Ramsden (1735 – 1800), English designer and manufacturer of mathematical and astronomical instruments, invented an electrostatic generator based on friction.

James Wimshurst (1832-1903), British physicist, invented the non-friction electrostatic generator that was named after him.

Electrostatic machines that convert energy into motion are normally seen as a field of research reserved for the sub-millimetric world, where electromagnetic actuators are no longer efficient. Since electrostatic motors can be realized using 2D structures (flat electrodes) and electromagnetic motors commonly need 3D structures (coils), they are particularly well suited for batch-fabricated micromotors made from mono-crystalline semiconductor substrate. Figure 1.10 shows typical examples:

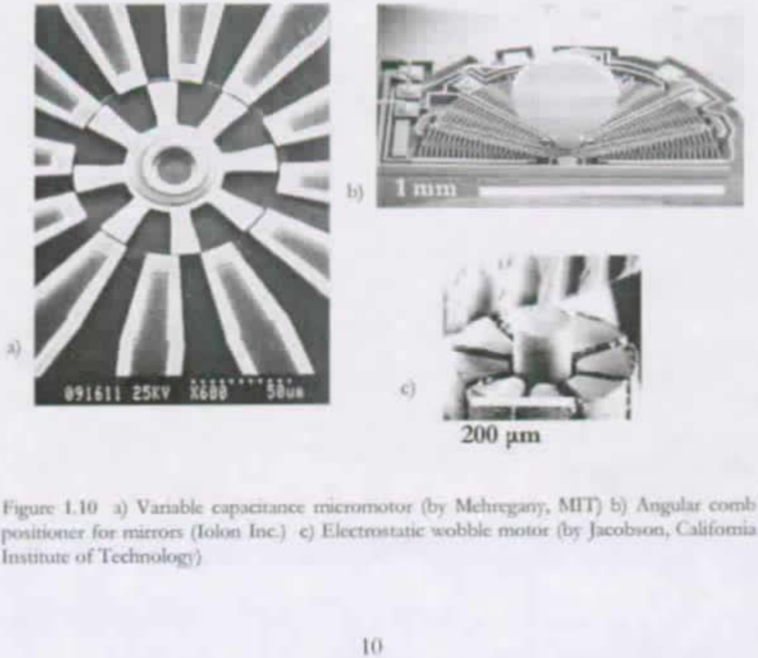

Figure 1.10 a) Variable capacitance micromotor (by Mehregany, MIT) b) Angular comb positioner for mirrors (Iolon Inc.) c) Electrostatic wobble motor (by Jacobson, California Institute of Technology)

The torques of the shown examples are typically in the nNm-range. Macroscopic electrostatic drives that have the potential for concurrence electromechanical solutions are still very rare. Yamamoto et al. [100] proposed a stacked, multi-layered linear actuator, coined the "Dual Excitation Multiphase Electrostatic Drive", where up to 50 sheets of flexible printed electrodes are mutually attracted or repelled. High electric field strength and therefore high force density is achieved by imersion of the electrode sheets into dielectric fluid (3M: Fluorinert FC-77) to prevent insulation breakdown of air. This combination gives absolutely remarkable performances for an electrostatic machine: Linear acceleration up to 120 g with maximum speed of 0.6 m/s and the possibility to develop 130 N linear thrust-force. Figure 1.11 shows the principle of the described actuator:

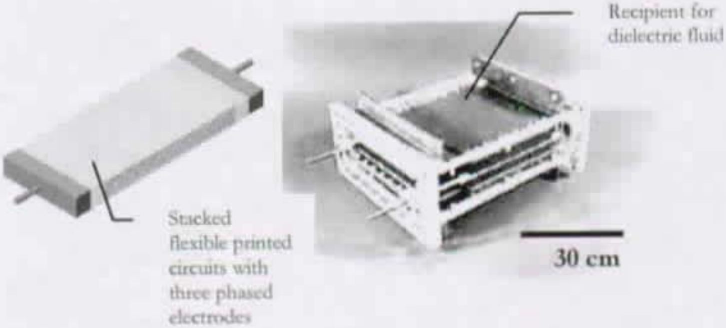

Figure 1.11 Principle and photograph of a macroscopic electrostatic actuator, the Dual Excitation Multiphase Electrostatic Drive

Macroscopic rotary electrostatic motors have been extensively studied by Ubink [97], Kooy [57] and Bollée [9]. They focused on asynchronous machines or they equipped both, rotor and stator, with electrodes to ensure synchronous movements. The asynchronous machines feature a thin conductive coating on a dielectric cylindrical rotor. The stator field being much faster than the rotor, these actuators gain their torque via the resistive losses of the induced charges. These concepts might find adequate applications, but for cost effective precise positioning, neither asynchronous behavior (need of additional sensors) nor electrodes or grooves on the disc (inherent speed ripple) are realistic options.

1.3.8 Synthesis

Nowadays, precise rotary positioning with resolutions under one arc second is feasible and available. The adequate actuators are proposed by the specialized industry and find broad applications in precision instrumentation and research. Masses down to a microscopic mirror can be rotated by using the corresponding appropriate actuation principle.
However, the actual systems have often limited operation and speed ranges, are encumbering, depend on precisely machined parts, rely on friction and wear. It will be shown that the electrostatic glass actuator has some unmatched features, such as an absolutely ripple-free rotation, unlimited operation range and a very broad speed range. This, together with its simple and compact structure, gives it a separate place among its counterparts and opens the door to new applications, in spite of the relatively weak forces it produces.

1.4 Electrostatic actuators

1.4.1 The inverse square law

Electrostatic theory is based on the single experimental postulate that electric charges exert forces on each other, which vary directly as the product of the strengths of the charges and inversely as the square of their distance of separation. Thus if q and q' are chosen to represent the strengths of two point charges, and r is the distance between them, the force which one charge exerts on the other may be expressed in the form

$$\vec{F} = K \cdot \frac{qq'}{r^2} \vec{1}_r \qquad K = \text{constant} \tag{1.1}$$

in which $\mathbf{1}_r$ is a unit vector along their connecting line. The two electric charges can be alike or opposite, causing the force to be repulsive or attractive. The inverse square law, as it is usually called, was first observed by Benjamin Franklin (1706 – 1790), who reported the phenomenon of electrostatic attraction. Henry Cavendish (1731 – 1810) provided a definitive demonstration [68], but unfortunately these highly original experiments were unknown to the scientific community since experimenters did not publish their findings. Credit and fame for the inverse square law were bestowed on Charles Augustin de Coulomb (1736 – 1806) who demonstrated the law of electric force using a torsion balance on which he measured the repulsive force between two like charges [19].

The mathematical formulation of the inverse square law follows from the general case of a probe charge *q* interacting with *N* other charges of the same value, a situation sketched in figure 1.12:

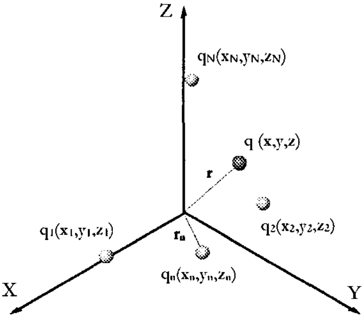

Figure 1.12 Notation for the inverse square law

The total force acting on the probe charge is the vector sum of all forces:

$$\vec{F} = \sum_{n=1}^{N} \vec{F}_n \qquad \text{with} \qquad \vec{F}_n = \frac{qq_n}{4\pi\varepsilon_0} \frac{\vec{r} - \vec{r}_n}{\left|\vec{r} - \vec{r}_n\right|^3} \tag{1.2}$$

Equation (1.2) is a mathematical statement of the inverse square law, and will hereafter be referred to as Coulomb's law. This equation is the cornerstone of all electrostatic and electromagnetic theory, and can be considered the fundamental postulate of electricity. The proportionality constant *K* equals $(4\pi\varepsilon_0)^{-1}$. Inclusion of 4π is known as rationalization and is done so that a factor of 4π will not appear in Maxwell's equations. The factor ε_0 is kind of a unit-adjustment parameter, called permittivity of free space, and its value in the MKS system is $8.854 \cdot 10^{-12}$ farads/m. This choice of ε_0 (dielectrical constant) permits charge to be measured in coulombs when distance is measured in meters and force in newtons.

1.4.2 Electrostatic energy

When it is assumed that an infinitesimal small charge Δq interacts with an arrangement of N static charges and that Δq does not affect the spatial distribution of the field (since it has very little value), then the force acting on the probe is

$$\Delta\vec{F} = \frac{\Delta q}{4\pi\varepsilon_0}\sum_{n=1}^{N} q_n \frac{\vec{r}-\vec{r}_n}{\left|\vec{r}-\vec{r}_n\right|^3} \tag{1.3}$$

and the vector

$$\vec{E} = \frac{\Delta\vec{F}}{\Delta q} = \frac{1}{4\pi\varepsilon_0}\sum_{n=1}^{N} q_n \frac{\vec{r}-\vec{r}_n}{\left|\vec{r}-\vec{r}_n\right|^3} \qquad [\mathrm{V/m}] \tag{1.4}$$

is variously called the electric force, the electric intensity or the electric field strength.

By implication, if a charge q of arbitrary size is placed in a region with field strength E it experiences the force

$$\vec{F} = q\vec{E} \tag{1.5}$$

It can be demonstrated [28] that the energy density of an electrostatic system can be written as

$$w = \frac{1}{2}\varepsilon_0 E^2 \tag{1.6}$$

The concept of energy storage in an electrostatic system may be illustrated by the fact that energy is required to assemble a system of charges into a given distribution.

An important example for electrostatic actuators is the parallel plate capacitor, as shown in figure 1.13:

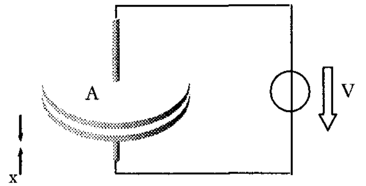

$$C = \varepsilon_0 \frac{A}{x} \qquad (1.7)$$

Figure 1.13 Parallel plate capacitor with equation for capacitance

The **stored energy** is calculated from the energy density by integration over the concerned volume. If the field is uniform, we can write

$$W = \frac{1}{2}\varepsilon_0 E^2 V \qquad (1.8)$$

For the case of the plate capacitor shown in figure 1.11 (the fringe field can be neglected), expression (1.8) becomes

$$W = \frac{1}{2}\varepsilon_0 E^2 Ax = \frac{1}{2}\left(\frac{\varepsilon_0 A}{d}\right)E^2 x^2 = \frac{1}{2}CV^2 \qquad (1.9)$$

1.4.3 Electrostatic forces

Electrostatic forces on charged particles can be calculated directly, and forces on charge distributions, like the ones found on the plates of a charged capacitor, can be calculated with force densities, or stress tensors, but these methods all require a detailed knowledge of the fields within or on the surface of the region of interest. This information is often unavailable, especially when the shape of the electrostatic actuator is complex. In fact, only the potentials on the electrodes are usually given, so it would be far more useful to have a way to calculate the force from these electrode potentials.

Fortunately, there is such a method [99], based on the conservation of energy. It can be used only for conservative devices, but most electrostatic devices, which produce forces, are conservative or can be treated as such by appropriate modifications of the model.

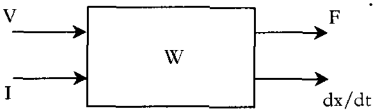

Figure 1.14 Energy flows to and from an electrostatic device

This idealized 'black box' system could also be seen as Bond-graph system [10] [14]. Bond-graphs are a powerful tool for describing dynamic models. The systems can have two types of ports: power ports and signal ports. Power ports specify both an effort variable and a flow varible. In the mechanical domain a powerport would for example be described by force (effort) and velocity (flow). Signal ports specify only one variable, which can either be a flow, an effort or a mathematical variable.

Since the system of figure 1.14 is considered to be conservative (no losses) this is a lumped device, energy can flow in or out only at specific terminals.

The total energy stored inside the device changes as a result of these flows:

$$\frac{dW}{dt} = VI - F\frac{dx}{dt} \tag{1.10}$$

In a capacitor the current is always given in terms of the stored charge as

$$I = \frac{dq}{dt} \tag{1.11}$$

so power conservation (equation 1.10) can be written as

$$\frac{dW}{dt} = V\frac{dq}{dt} - F\frac{dx}{dt} \tag{1.12}$$

or, by integration over a short time interval, we can write conservation of energy as

$$dW = Vdq - Fdx \tag{1.13}$$

The presented method is also not adequate for systems that contain energy sources, since these also will violate conservation of energy. Electrets, for example, contain a source of charge that, if not separated from the conservative system, can give erroneous results.
Electrostatic actuators can mostly be modeled as a capacitor system. A capacitor with given electrode spacing x and charge q (see figure 1.13), will always have a definite energy, which depends on these variables:

$$W = W(q,x) \tag{1.14}$$

Changes in this energy are given by the chain rule of differentiation as

$$dW = \left.\frac{\partial W}{\partial q}\right|_x dq + \left.\frac{\partial W}{\partial x}\right|_q dx \tag{1.15}$$

This purely mathematical statement is very similar to the physical statement of equation (1.13). Since both statements are true, and the independent variables x and q can be selected at will, the corresponding coefficients of equations (1.13) and (1.15) are identical and, by keeping the charge constant, we can write the expression we use to calculate the forces exerted by a lumped electrostatic device.

$$F = -\left.\frac{\partial W}{\partial x}\right|_q \tag{1.16}$$

Introducing expression 1.9 for the stored energy in a capacitor, we find for the force acting on the plates of a charged capacitor

$$F = -\frac{1}{2}V^2 \cdot \frac{\partial C}{\partial x} \tag{1.17}$$

Using the concrete example of a parallel plate capacitor as shown in figure 1.13, we find

$$F = \frac{A\varepsilon_0 V^2}{2x^2} \tag{1.18}$$

The attracting force is proportional to the square of the applied voltage and inverse proportional to the square of the gap between the electrodes. Figure 1.16 shows a concrete example:

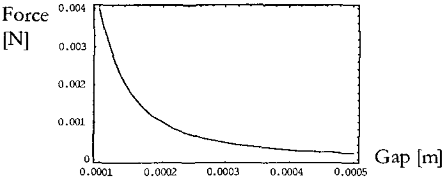

Figure 1.15 Attraction force between capacitor plates, A=1cm^2, V = 300V

1.4.4 Scale laws

Another strong argument in favor of electrostatics is scale laws. It is well known that electrostatic actuators are advantageous when one goes for small-scale applications.

As a reminder, scale laws reduce physical properties to a characteristic length Γ. So, for some familiar physical properties, we can write:

Mass	$M \sim \Gamma^3$
Resistance	$R \sim \Gamma^{-1}$
Capacitance	$C \sim \Gamma$
RC-time constant	$\tau \sim \Gamma^0$ = constant
Inductance	$L \sim \Gamma$

Table 1 Scale dependency of some physical properties

The energy density of the magnetic field is

$$w_{mag} = \frac{B^2}{2\mu} \tag{1.19}$$

with B the magnetic induction and μ the permeability.

For an electric field, the energy density is

$$w_{estat} = \frac{\varepsilon_0 E^2}{2} \tag{1.20}$$

Reducing the efficiency to the ratio of output energy and the input energy, we find

$$\eta_{mag} = \frac{E_{diss}}{E_{mech}} \propto \frac{\Gamma^{-2}\Gamma^{3}}{\Gamma^{-1}} = \Gamma^{2} \tag{1.21}$$

for the electromagnetic efficiency. This efficiency is strongly decreasing with size. The use of a permanent magnet in the electromagnetic system helps, it can be found that, for most cases (not considering the effect of the current density):

$$\eta_{mag}\Big|_{magnets} = \frac{E_{dicc}}{E_{mech}}\Bigg|_{magnet} \propto \Gamma \tag{1.22}$$

and, for the electrostatic actuator

$$\frac{E_{diss}}{E_{mech}} \propto \frac{\Gamma}{\Gamma} = \Gamma^{0} = \mathit{INVARIANT} \tag{1.23}$$

In other words, the efficiency of the electrostatic actuator does not change with size (a valuable advantage for miniaturization) while it decreases with Γ for a magnetic system with a permanent magnet and even with Γ^2 without permanent magnet.

Equations (1.19) and (1.20) indicate the maximal obtainable force densities. Putting B_{max} = 1 Tesla, we obtain $w_{mag,max}$ = 10^6 [pa] (10 bar). For the electrostatic actuator, this maximal value cannot be determined easily, since the maximal value of E depends strongly on the electrode shape, inter-electrode distance and the atmospheric pressure. At sea level at 1 bar pressure, E_{max} = $3 \cdot 10^6$ [V/m], so $w_{estat,max}$ = 15 [pa] (0.15 mbar). Given the small inertias at small scale and the invariance of the efficiency (1.23), electrostatic actuators are often more advantageous, despite the smaller force density. This force density can drastically be improved by changing the inter-electrode gap or the pressure, as reported by Paschen [82].

Paschens' law describes the relationship between breakdown-voltage on one hand and the product of gas-pressure and electrode-gap on the other hand. For usual technical applications, this relationship is linear: As mentioned earlier, breakdown voltage in air at 1 bar is around 3 [kV/mm]. At atmospheric pressure (1bar, 10^5 pascal), the breakdown voltage decreases linearly with the distance between two opposite electrodes. However, if the distance between the two electrodes gets in the order of the micrometer, the breakdown voltage increases.
Figure 1.16 sketches the breakdown voltage versus the inter-electrode distance:

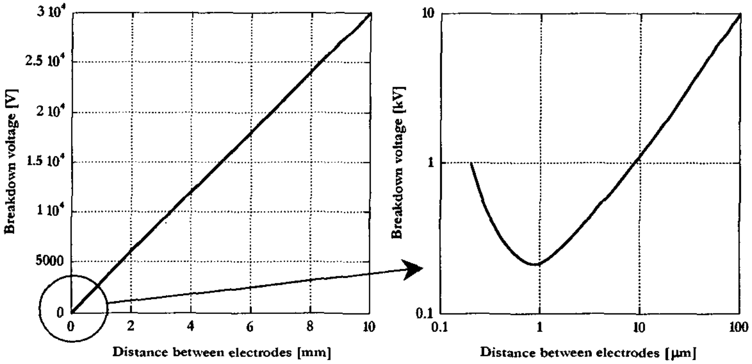

Figure 1.16 Breakdown voltage versus inter-electrode distance at atmospheric pressure

In a gas, an ionized molecule is attracted by an electrode and ionizes other molecules (avalanche effect). In the absence of molecules, no electrostatic breakdown occurs. This absence of molecules can be achieved by a small gap (figure 1.16) or low gas pressure. So, for small gaps (or low pressure), the breakdown voltage significantly increases.
Paschens' law states that the breakdown voltage is dependant on the product of atmospheric pressure and the gap between two electrodes. It can be seen that the energy density can be improved by modifying the atmospheric pressure.

Figure 1.17 plots Paschens' law for air:

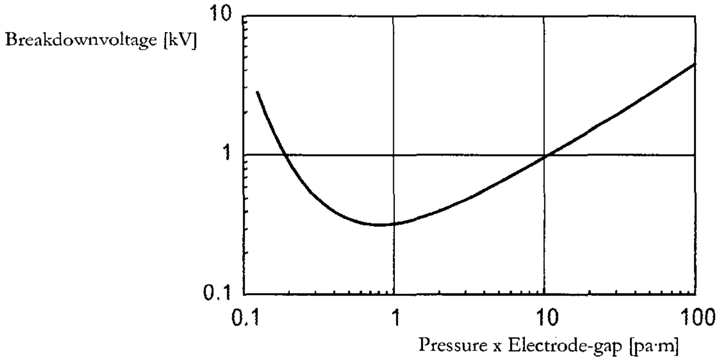

Figure 1.17 Paschens' law for air

In other words, one gains energy density with an electrostatic actuator for small scales or low pressure. The physical limit is the field emission ($E=10^9$ [V/m]) where the electrons would be directly extruded from matter. So the physical limit for the electrostatic energy density is $w_{estat,max}= 1000$ [pa].

II. Electrostatic glass motors

2.1 Dielectric properties of glasses

A dielectric material reacts to an electric field differently than free space because it contains charge carriers that can be displaced, and charge displacements within the dielectric can neutralize a part of the applied field. The principal characteristic of a capacitor is that an electrical charge Q can be stored. The charge is expressed by

$$Q = CV \tag{2.1}$$

where V is the applied voltage and C is the capacitance. The voltage is directly proportional to the amount of charge stored.
If a dielectric material of permittivity ε is inserted between the electrodes, the capacitance is modified

$$C = C_0 \frac{\varepsilon}{\varepsilon_0} = C_0 \kappa \tag{2.2}$$

where ε_0 is the permittivity of vacuum, C_0 the capacitance without dielectric and κ is the relative permittivity or relative dielectric constant. It follows from (2.1) and (2.2) that we can write for a capacitor containing a dielectric

$$V = \frac{Q / \kappa}{C_0} \tag{2.3}$$

That is, only a fraction of the total charge, the free charge Q/κ sets up an electric field, a voltage toward the outside; the remainder, the bound charge, is neutralized by polarization of the dielectric. Polarization of a dielectric results in an induction of charges, charges which change the electrostatic equilibrium between the electrodes, as suggested by (2.3). In presence of dielectric matter, the Gauss theorem becomes

$$\oint \left(\varepsilon_0 \vec{E} + \vec{P} \right) d\vec{A} = \vec{Q} \tag{2.4}$$

constituting a general result. The vector ***P***, called the polarization vector, is characterizing the dielectrics' properties. It represents the dipolar moment per volume unit of a specific dielectric. One can formulate the Gauss theorem for dielectrics with the help of the electric displacement vector ***D***:

$$\oint \vec{D} d\vec{A} = \vec{Q} \qquad \text{with} \quad \vec{D} = \varepsilon_0 \vec{E} + \vec{P} \tag{2.5}$$

For the case of a parallel plate capacitor, (2.5) can be simplified to

$$D = \frac{Q}{A} \tag{2.6}$$

A being the surface of the electrodes. The vector ***P*** of (2.5) can be written as

$$P = N\tau \tag{2.7}$$

where N is the number of dipoles per unit volume and τ is the average dipole moment.
Combining (2.7) with (2.5) and (2.1), we find for a parallel plate capacitor:

$$C = \frac{Q}{V} = \frac{DA}{V} = \frac{(\varepsilon_0 E + P)A}{V} \tag{2.8}$$

With $D=\varepsilon E$, so (2.7) takes the familiar form

$$C = \frac{\varepsilon EA}{V} = \frac{\varepsilon A}{x} \tag{2.9}$$

In an ideal capacitor the electric charge adjusts itself instantaneously to any change in voltage. Since the variation of polarization with time parallels the variation of charge with time, polarization should adjust itself instantaneously. In practice, however, there is an inertia-to-charge movement that shows up as a relaxation time for charge transport. This is exactly analogous to the time required for elastic strain to follow an applied stress. This dependence of the dielectric constant on frequency is shown in figure 2.1:

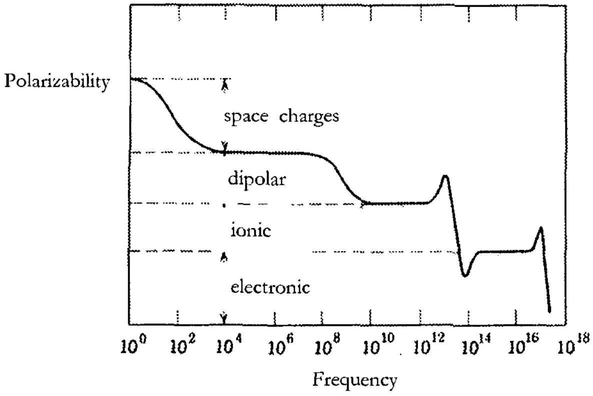

Fig. 2.1 Frequency dependence of several contributions to the polarizability of dielectrics (taken from [37])

The electronic polarization is the only process sufficiently rapid to follow AC fields at the frequency of visible light; as a result the index of refraction, for example, depends only on this process. Ionic polarization processes are able to follow an applied high-frequency field and contribute to the dielectric constant at frequencies up to the infrared region of the spectrum. Orientation and space charge polarization have relaxation times bound to lower frequencies.

During charging, for example, if the rate of change of the polarization with time is assumed proportional to the difference between its final value and its actual value

$$\frac{d(P_t - P_I)}{dt} = \frac{1}{\tau}\left[(P_F - P_I) - (P_t - P_I)\right] \tag{2.10}$$

then

$$P_t - P_I = (P_F - P_I)\left(1 - e^{-t/\tau}\right) \tag{2.11}$$

Here P_t is the polarization at time t, P_I is the instantaneous polarization on applying the field, P_F is the final value of the polarization, and τ is a constant having the dimension of time. For illustration, figure 2.2 sketches the behavior of a real dielectric.

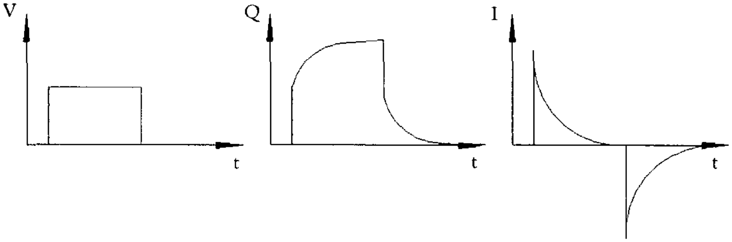

Fig. 2.2 Schematic behavior of charge buildup and current flow in a real dielectric

The dynamics of the charges are linked to the polarization dynamic through (2.8). The constant τ is called a relaxation time and is a measure of the time lag of the system. The response of most real dielectric materials to an applied field is not well represented by a single relaxation time. Rather, distributions of relaxation times are required to describe the experimental data [55].

The usual experimental description of the polarization phenomenon passes via the so-called 'absorption current': For a potential V applied to a simple capacitor with capacitance C in a circuit with external resistance R (there is always some resistance in the measuring circuit), the current I for an ideal dielectric is:

$$I = \frac{V}{R} e^{-t/RC} \tag{2.12}$$

where t is the time. This is called a displacement or polarization current. Many ceramic insulators, including glasses, have in addition to a large, rapid changing current, given by (2.12), and a small steady current, associated with their finite resistance, a current of intermediate magnitude which decays over periods of seconds to minutes or longer at room temperature [55]. This intermediate current is termed the absorption current I_a. Figure 2.3 shows the absorption current during charge and discharge of a capacitor for a soda-lime-silicate glass taken from the literature:

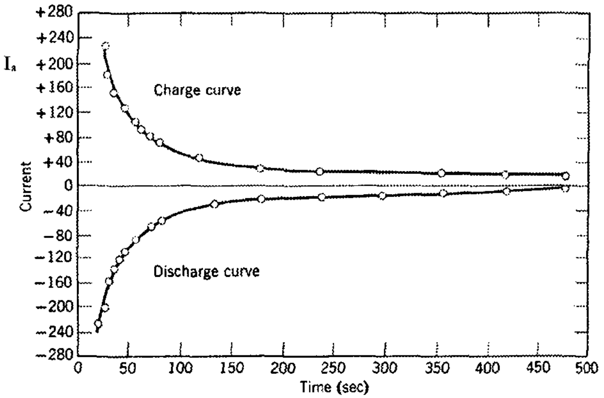

Fig. 2.3 Absorption current during charging and discharge of soda-lime-silicate glass (taken from [55]), experimental parameters are unknown, as well as the unit on the current axis.

As for the dynamics of polarization, the variation of the absorption current with time is not well represented by a single exponential function but requires a series of exponentials for its description:

$$I_a = \Lambda_1 \exp\left(-\frac{t}{\tau_1}\right) + \Lambda_2 \exp\left(-\frac{t}{\tau_2}\right) + \Lambda_3 \exp\left(-\frac{t}{\tau_3}\right) + \ldots \qquad (2.13)$$

A_i being constants. The number of relaxation times τ required to describe the data is reported to be associated with local structural variations, and corresponding variations of local potential barriers in the glass [55].

As the temperature increases, the time dependence of the absorption current shortens, and it is not commonly observed in DC measurements at temperatures above approximately 300°C. The absorption current in a rapidly cooled glass is about four times as large as in a well-annealed specimen of the same glass.

What does this mean for a capacitance with a glass dielectric between its electrodes? If, after instantaneous polarization, the capacitor current has a slow component with the allure of (2.13), and since

$$I = \frac{dQ}{dt} \tag{2.14}$$

we can describe the allure of the capacitance-variation with time:

$$Q = CV \Rightarrow \frac{dQ}{dt} = \frac{dC}{dt}V \Rightarrow \frac{dC}{dt} = \frac{dQ}{dt} \cdot \frac{1}{V}$$

$$\frac{dC}{dt} = \left(\Lambda_1 \exp\left(-\frac{t}{\tau_1}\right) + \Lambda_2 \exp\left(-\frac{t}{\tau_2}\right) + \Lambda_3 \exp\left(-\frac{t}{\tau_3}\right) + \ldots \right) \cdot \frac{1}{V} \tag{2.15}$$

The variation of capacitance with time has the same allure as the variation of charge with time. Therefore, the variation of polarization with time also has the same allure, based on (2.8).

Since the integral of an exponential function is also an exponential function and the integral of a sum is the sum of the integrals, equations (2.15), (2.11) and (2.8) become

$$C(t) = \frac{(\varepsilon_0 E + P(t))A}{V} =$$

$$\frac{\left(\varepsilon_0 E + P_I + (P_F - P_I)\left(1 - \left(\Omega_1 \exp\left(-\frac{t}{\tau_1}\right) + \Omega_2 \exp\left(-\frac{t}{\tau_2}\right) + \ldots\right)\right)\right)A}{V} \tag{2.16}$$

Ω_i being constants. For the sake of simplification, we keep only the first member of the exponential sum, to write a compact expression for the capacitance. Then, (2.16) becomes:

$$\boxed{C(t) = C_I + (C_F - C_I)\left(1 - \Omega \exp\left(-\frac{t}{\tau}\right)\right)} \tag{2.17}$$

Figure 2.4 sketches the allure of (2.17):

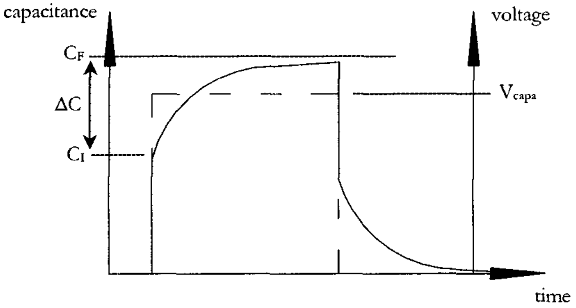

Fig. 2.4 Capacitance versus time for an applied voltage step. The voltage at the electrodes is kept constant.

C_I denotes the capacitance that occurs immediately when the voltage is switched on. C_F is the final capacitance after several hours of charging. So it is possible to induce relatively stable charges into glass objects by application of an electrostatic field. By charging for a sufficient long time, a capacity increase of ΔC (see figure 2.4) can be obtained.

2.2 Lateral restriction force

Consider the experiment depicted in figure 2.5:

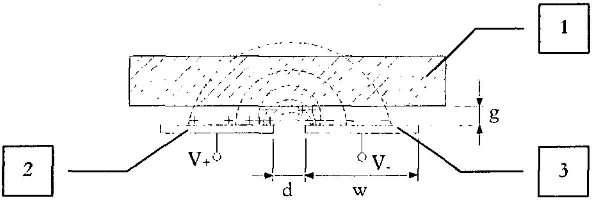

Fig. 2.5 Electrostatic system composed of a glass plate facing two capacitor electrodes

A glass plate **1** is fixed at constant gap *g* over two electrodes, on one we apply a positive potential V_+ **2**, on the other a negative potential V_- **3**. The two electrodes have a width *w* and a mutual gap *d*. This system forms a capacitance, function of time, as described by (2.17). Equation (1.17) allows us the computation of the attraction force between the electrodes and the glass plate:

$$F_Z = -\frac{1}{2}V^2\frac{dC(t)}{dz} = -\frac{1}{2}V^2\left(\frac{dC_I}{dz} + \frac{d(C_F - C_I)\left(1-\Omega\exp\left(-\frac{t}{\tau}\right)\right)}{dz}\right) \tag{2.18}$$

This force can be decomposed into a sum of two forces, the first summand in (2.18) describes the force due to the instantaneous polarization, the second one the force due to the slow relaxation time of glasses. If the electrodes move parallel to the glass surface, a lateral restriction force arises, like sketched in figure 2.6.

The fundamental phenomenon that makes the electrostatic glass motor work is the presence of this lateral restriction force. Only the component of the attraction force F_z due to the slow relaxation time, the second member of (2.18), contributes to the lateral restriction force F_x. The system can be viewed as an electret machine, with unstable charges on the glass surface. Like an electret device, the movement is synchronous, the displacement speed of the glass plate equals the displacement speed of the electrodes.

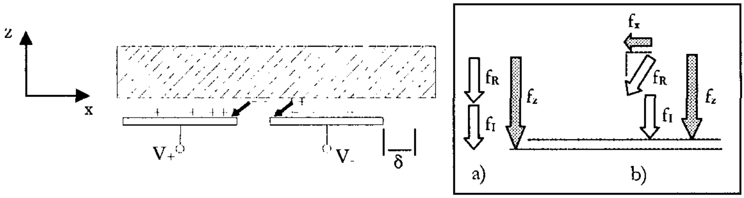

Fig. 2.6 Generation of lateral restriction force if the electrodes move parallel to the glass plate. The inlet shows the vectors of the involved forces a) after charging without displacement b) after a parallel displacement *δ*.

During charging (figure 2.6 a), the attraction force F_z is continuously increasing (2.18) due to the force F_R which is linked to the glasses' slow relaxation time. The instantaneous force F_I remains constant. If the electrodes move parallel to the glass plate with a displacement δ while the air-gap is maintained (figure 2.6), then a lateral restriction force $F_{x'}$ due to the stable induced charges occurs. The instantaneous force F_I does not contribute to this restriction force.
Trigonometry leads to

$$F_{X'} = F_R \sin\left(\frac{\delta}{g}\right) \tag{2.19}$$

And the attraction force F_z is diminished by a complementary ratio

$$F_{Y'} = F_I + F_R \cos\left(\frac{\delta}{g}\right) \tag{2.20}$$

It becomes clear that, for actuators making use of the lateral restriction forces, glasses with a large ΔC (see figure 2.4) are interesting.
If the glass could move parallel to the electrodes without any friction (by means of an air-bearing or the like) and without load, it would lag slightly behind the moving electrodes, but follow them synchronously. A point on the glass plate would always see the same potential, so the glass plate will remain charged as long as the potential is applied to the electrodes.

2.3 Structure of electrostatic glass motors

The electrostatic glass motor consists basically of a glass rotor, "sandwiched" by one or two electrodes. The electrodes form a three-phase array in such a way that they, driven by mutually phase-shifted excitations, produce a moving electrostatic field. These excitations are sinusoids or step waves. The proposed structure is sketched in figure 2.7, with indication of the various parameters that characterize an electrostatic glass motor. A glass rotor **1** is mounted by means of a bearing **2** in a way that there is no contact with the electrodes **3**. If there are two electrode plates (two side drive), then the upper and lower electric field have to move in the same direction. The determining parameters for the lateral restriction forces (and torques) are, for the linear drive, the width of the electrode tracks w, the gap between two neighboring electrode tracks d, the air-gap between glass and motor electrodes g and the surface of the glass rotor A.

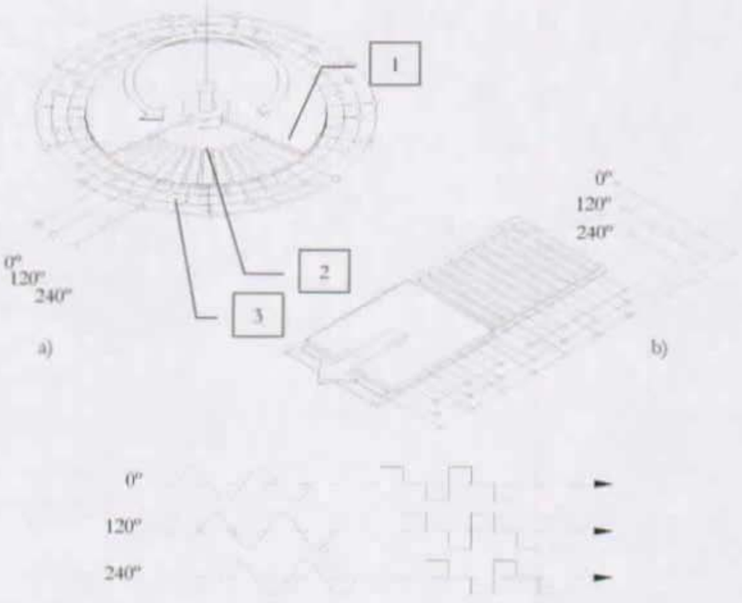

Fig. 2.7 Structure of electrostatic glass motors. a) Rotary single side drive, b) rotary double side drive, c) linear single side drive.

For the rotary drive, these parameters are the number of electrode tracks n, the width of the electrode tracks at its minimum w_{min}, the outer radius R_{out} which equals the maximum radius of the electrode-stripes and inter-track gap d. Obviously, the geometric parameters of the electrodes are not mutually independent. The performances are further influenced by the ambient humidity, temperature, as well as the electrical properties of the blend of glass used and the potential difference applied to the electrodes.

Three different sequences can be distinguished during the operation of an electrostatic glass motor (figure 2.8):

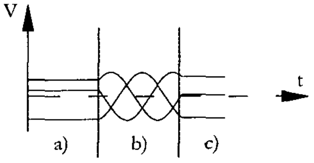

Fig. 2.8 *Different sequences for charging, driving and stopping the rotor.*

The first sequence a) charges the glass rotor in order to build up stable charges, as described in the previous sections. After several seconds of charging, the field begins to move b) and the motor operates synchronously. If the motor is to be stopped, the three sine waves have to be frozen into DC again c), the motor can now be restarted at any time, since, during its operation, the glass charges remain under the same potential (synchronous movement), so depolarization does not arise until the voltages are completely shut down.

2.3 Synchronous movement

As explained previously, the electrostatic glass motor operates synchronously. During charging, the electrostatic field seen by the glass rotor is not sinusoidal. The induced polarization, therefore charge-distribution, is peak-shaped and concentrated in the glass regions that face the inter-electrode gap *d*. During operation, the moving field is seen as a static field by the synchronously moving rotor and can be approximated by a perfect sinusoidal wave. The glass will re-polarize under the new field conditions and, with a time constant identical to the one described in equation (2.17), will feature a sinusoidal charge distribution.

Figure 2.9 shows the charge distribution in the glass over a three-phased electrode pattern, simulated using the surface charge method [21].

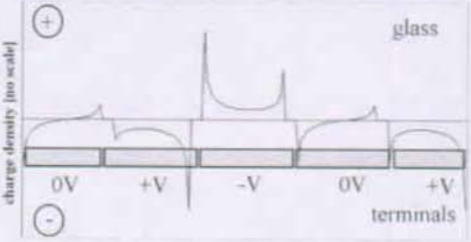

Fig. 2.9 Schematic plot of the glass charge distribution due to a three phase electrostatic field (no scale). The encircled signs indicate the positive and negative net polarization.

The synchronous propulsion is possible over a very broad speed range. Even if the field moves slowly enough to give the charges the possibility to rearrange themselves, a usable force would be observed [72]. For a field speed approaching zero, the capability of the electrostatic glass motor to drive a load tends to zero, too.

Figure 2.10 sketches the variation of charge densities for a slow moving field.

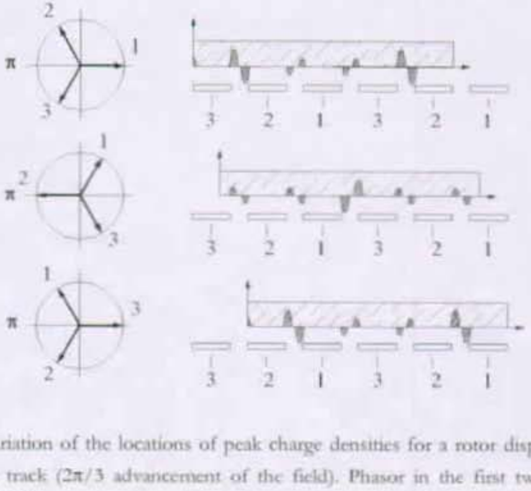

Fig. 2.10 Variation of the locations of peak charge densities for a rotor displacement of one electrode track ($2\pi/3$ advancement of the field). Phasor in the first two quadrants indicates a positive voltage. Accordingly, charge distributions 'below' the glass surface represent negative net polarization of the glass

The charge densities are modeled after figure 2.9, with peak amplitudes twice as high between plus and minus electrodes than in all the other possible cases. Indicated on the left-hand side is the phase evolution of the three channels and on the right-hand side is the corresponding position of the glass rotor. The absence of grooves or electrodes on the glass ensures ripple free displacement.

The advancement of the moving electrostatic field is easy to observe. Consider a digital function generator that is triggered by an external clock, in the absence of which it holds the last output voltage at DC level. Assuming that the rotor follows exactly the field, it is sufficient to count the clock impulses by knowing the rotors location. The rotor speed is a function of the clock frequency.

Figure 2.11 presents the open loop control scheme for the proposed device:

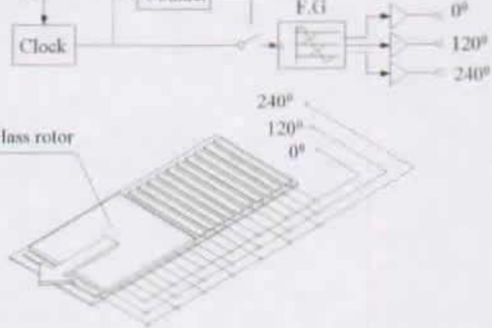

Fig. 2.11 Open loop control scheme. *F.G* indicates a three-channel function generator with mutually locked phases. The arrow indicates the direction of motion.

The parameter *f* stands for the frequency of the clock, therefore the speed of the glass rotor. The rotor position is controlled via the parameter *k*, which is a function of the desired displacement and the geometric dimensions of the electrode. The parameter *k* is the number of desired displacement steps. Once the desired number of clock impulses is delivered to the function generator, the clock will be interrupted, and the system is brought to rest by freezing the sinusoidal excitations into DC voltage.

For the determination of *k*, consider figure 2.12:

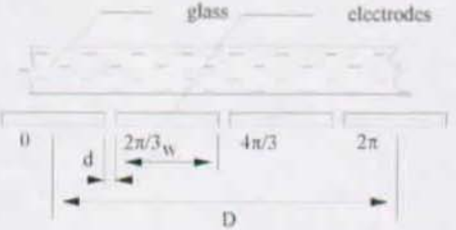

Fig. 2.12 Geometric electrode parameters for a three-phase excitation, used for the determination of the displacement-unit parameter k.

Let n [bit] be the resolution of the function generator output. The output voltage will then have 2^n distinct voltage levels if the function generator is driven at its full range. The distance D denotes the width of one set of electrodes (figure 2.16). If the applied field moves 360°, the rotor follows and makes a displacement of D, since the movement is synchronous. During this displacement, $2 \cdot 2^n$ voltage steps are applied by the function generator.

In the case of a linear actuator:

By approximating the sine wave with a ramp wave, we may write for the resolution ζ:

$$\zeta \approx \frac{D}{2 \cdot 2^n} \qquad [\mathrm{m}] \qquad (2.21)$$

Be v the speed of the glass rotor, and f the clocks' frequency in Hertz, so:

$$v = \zeta \cdot f \qquad [\mathrm{m/s}] \qquad (2.22)$$

Let δ be the intended rotor displacement. The coefficient k follows from (2.21):

$$k = \frac{\delta}{\zeta} \tag{2.23}$$

In the case of rotary actuator:
Let *m* be the number of poles on the rotor electrode (3 electrode tracks form one pole), and *n* the resolution of the function generator, then a similar reasoning as for the linear case leads to rotary resolution

$$\zeta \approx \frac{360}{m \cdot 2^n} \qquad [\,^\circ\,] \tag{2.24}$$

or

$$\zeta \approx \frac{360 \cdot 3600}{m \cdot 2^n} \qquad [\text{ arc sec }] \tag{2.25}$$

of course equation (2.23) stays valid for the rotary case.

The electrodes can be realized by printed circuit technology, so the precision of the geometrical dimensions (figure 2.12) is ensured.
The absence of grooves (variable capacitance motor) or fixed charges (electret motor) ensure that the motor has no other equilibrium positions than those dictated by the applied moving field, i.e. if a perfectly sinusoidal field is applied, a perfectly sinusoidal rotor charge distribution is expected. The interaction between these two sources should result in a ripple free displacement.

III. Analytical Model

3.1 Introductory remarks

3.1.1 Active motor surface

The electrostatic glass actuator has some appreciable advantages over its electromagnetic alternatives, when a disc shaped rotor has to be powered and the space for the motor is limited.
Figure 3.1 shows the concept of powering the disc rather than its axis:

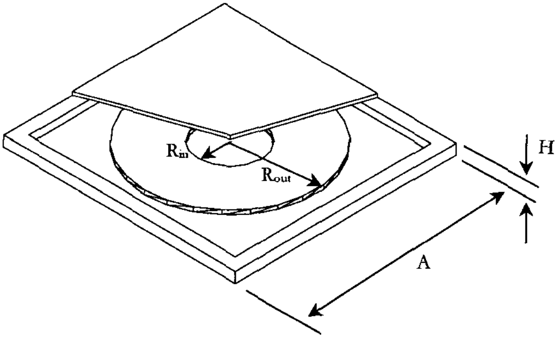

Fig. 3.1 Problem of powering a disc shaped rotor in a limited volume of dimensions *AxH*

For an axis-powered device, such as most electromechanical motors, the active motor area is

$$Area_{axis} = H \cdot 2\pi \cdot R_{in} \tag{3.1}$$

Whereas for a disc surface powered device, the active area can be written as

$$Area_{disc} = 2\pi \cdot \left(R_{out} - R_{in} \right) \tag{3.2}$$

Within reasonable boundaries, expression (3.2) is always larger than expression (3.1). For targeted applications with disc radii under 10 cm, the ratio is approximately ten.

3.1.2 Stacking motor layers

Consider an electrostatic glass motor composed out of *n* electrode-glass layers as sketched in figure 3.2:

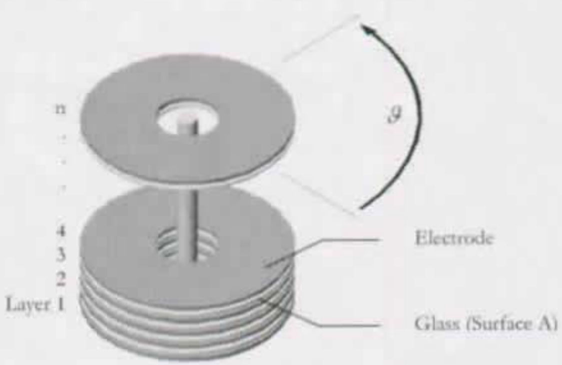

Fig. 3.2 Stacked glass-electrode layers on a motor axis

The resulting torque T_n is proportional to the total surface of the discs:

$$T_n \propto n \cdot K \cdot A \qquad K = \text{constant} \tag{3.3}$$

The inertia with respect to the rotation axis is

$$I_n = n \cdot \frac{1}{2} m R^2 \qquad \text{with} \qquad m = \pi R^2 h \rho \tag{3.4}$$

h being the necessary thickness of the glass rotor to ensure maximal restriction forces and ρ the density of the glassy rotor.
Setting the surface A to $A=\pi R^2$ (approximation of a plain disc), (3.2), (3.3) and (3.4) leads to:

$$\ddot{\vartheta} = \frac{2K}{R^2 h \rho} \tag{3.5}$$

The obtainable acceleration is independent from the number of stacked glass-electrode pairs. Thereby, stacking motor layers is a valid approach to torque-augmentation.

3.2 Forces and torques

3.2.1 Attraction forces

The Ansatz for an analytical model is that if we can maximize F_g, the attraction force between glass rotor and electrode substrate due to the slow relaxation time, for a static field, we also maximize the lateral restriction force F_x. The task is to determine the parameters *d*, *w* and *g* as well as the according potential difference between two electrodes to develop a maximal attraction force per unit surface.

Figure 3.3 shows a numerical simulation of the flux lines between two opposite electrodes, again with all the relevant geometrical parameters and its model approximation:

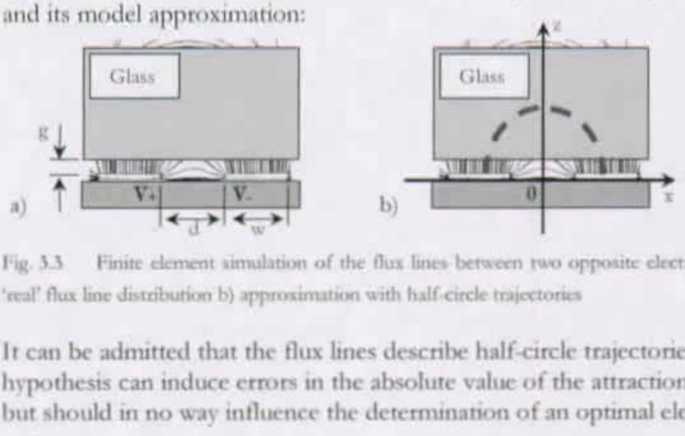

Fig. 3.3 Finite element simulation of the flux lines between two opposite electrodes. a) 'real' flux line distribution b) approximation with half-circle trajectories

It can be admitted that the flux lines describe half-circle trajectories. This hypothesis can induce errors in the absolute value of the attraction force, but should in no way influence the determination of an optimal electrode pattern.

The force calculation is performed using the method of the virtual displacement (energy method), as explained in section 1.4.3.

The capacitance of our system is composed of various capacitances, mutually connected in parallel and series, as shown in figure 3.4.
We assume that the air-gap g and the inter-electrode gap d are chosen in such a way that $g < d$. This assumption represents the situation where all flux lines pass through the glass (figure 3.4).

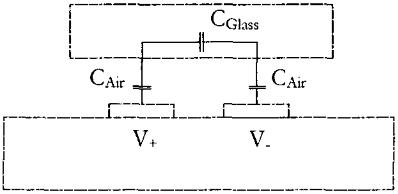

Fig. 3.4 Model of the capacitances that change with the airgap g for the case of $g < d$

Choosing the coordinate system of figure 3.3b, the capacitance of figure 3.4 can be computed by using the infinitesimal capacitance $dC(x)$

$$dC(x) = \frac{L}{\frac{\gamma_a}{\varepsilon_a} + \frac{\gamma_g}{\varepsilon_g}} dx \tag{3.6}$$

where γ_a and γ_g designate the trajectories in air and glass, respectively. The permittivities of air and glass are ε_a and ε_g. L denotes the length of an electrode track. Equation (3.6) is the approximation of a parallel plate capacitor with dielectric and air between its terminals.

Geometrical approximation leads to

$$\gamma_a(x) \approx 2g \tag{3.7}$$

The trajectory in the glass is the complement to a half circle circumference

$$\gamma_g(x) \approx \pi x - 2g \tag{3.8}$$

Equations (3.6), (3.7) and (3.8) lead to

$$dC(x) = \frac{L\varepsilon_a\varepsilon_g}{2g\left(\varepsilon_g - \varepsilon_a\right) + \pi\varepsilon_a x}\,dx \tag{3.9}$$

Integration over the range $x \in [d/2\,,\ d/2 + w]$ leads to

$$C = \frac{L\varepsilon_g}{\pi}\ln\left(\frac{4g\left(\varepsilon_g - \varepsilon_a\right) + \pi\varepsilon_g\left(d + 2w\right)}{4g\left(\varepsilon_g - \varepsilon_a\right) + d\pi\varepsilon_g}\right) \tag{3.10}$$

The attraction force F_Z can now be computed. The voltage V and distance d are not independent, the breakdown field at sea level being around 3 [MV/m]. Application of (1.17) leads to

$$F_Z = \frac{4LV^2 w\varepsilon_a\varepsilon_g\left(\varepsilon_a - \varepsilon_g\right)}{\left(\pi\varepsilon_a\left(d + 2w\right) - 4g\left(\varepsilon_a - \varepsilon_g\right)\right)\left(d\pi\varepsilon_a + 4g\left(\varepsilon_g - \varepsilon_a\right)\right)} \tag{3.11}$$

As seen in section 2.1 and 2.2, it is the slow relaxation time of glasses that allows the propulsion of the rotor. Equation (2.10) describes the evolution of polarization with time, while equation (2.16) approximates the evolution of the capacitance with time. In order to introduce this effect into the expression of F_Z, we replace the constant ε_g by a time dependent function. Based on equation (2.15), two approximations seem promising:

$$F_Z = \frac{4LV^2 w\varepsilon_a\Psi(t)\left(\varepsilon_a - \Psi(t)\right)}{\left(\pi\varepsilon_a\left(d + 2w\right) - 4g\left(\varepsilon_a - \Psi(t)\right)\right)\left(d\pi\varepsilon_a + 4g\left(\Psi(t) - \varepsilon_a\right)\right)} \tag{3.12}$$

with $$\Psi(t) = \varepsilon_I + \left(\varepsilon_F - \varepsilon_I\right)\cdot\left(1 - \exp\left(-\frac{t}{\tau}\right)\right) \tag{3.13}$$

or $$\Psi(t) = \varepsilon_I + \left(\varepsilon_H - \varepsilon_I\right)\cdot t^{1-\alpha} \tag{3.14}$$

Approximation (3.13) is based on equation (2.15), retaining just one exponential term. This approximation needs an experimentally determined asymptotic value. Approximation (3.14) is proposed by Umé [98], for the representation of electrostatic fields in nonlinear matter, for the case where the asymptotic limit does not exist or is not known. His model is based on a hyperbolic function (as seen in equation 3.14), with the following allure (figure 3.5):

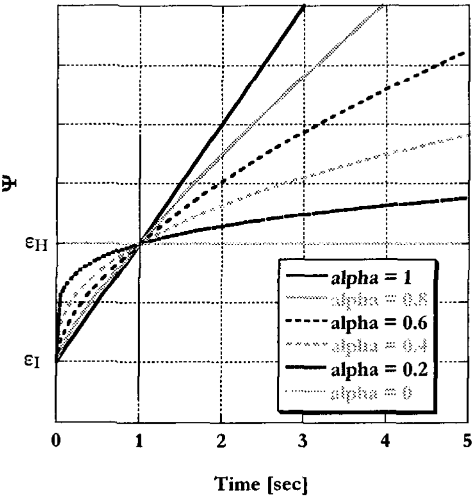

Fig. 3.5 Behavior of the dielectric constant function Ψ versus time for different power coefficients a

Since glass is one of the most complex technical materials (amorphous structure, sometimes with crystalline regions, with a great variety of additional components with a great variety of concentrations), the parameter τ (3.13) and the parameters a and ε_H (3.14) are expected to be determined experimentally.

The parameter ε_I of equation (3.14) is the 'normal' dielectric constant of the glass, determined by an AC capacitive measurement. The indices I and F indicate, analog to figure 2.4, *instantaneous* and *final*, respectively. Extending this concept to the attraction force, or more generally to the force density, we find the situation of figure 3.6 (based on a experimental measure). The force density f_R is due to the slow polarization phenomenon of glasses and adds itself to the instantaneous force density f_I.

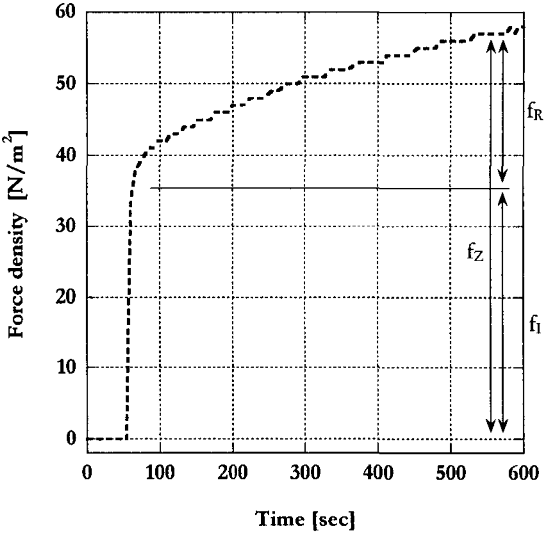

Fig. 3.6 Measurement of attraction force-density between soda-lime glass and electrode. f_R indicates the force density due to the slow relaxation time of glasses. (d=300μm, w=300μm), applied potential 1000 V, air-gap g = 100μm, RH = 30 %

As discussed previously, only f_R contributes to the lateral restriction force. If we continue to argument using forces, and not force densities, we can write for the instantaneous force F_I:

$$F_l = \frac{4LV^2 w\varepsilon_a\varepsilon_l(\varepsilon_a - \varepsilon_l)}{(\pi\varepsilon_a(d + 2w) - 4g(\varepsilon_a - \varepsilon_l))(d\pi\varepsilon_a + 4g(\varepsilon_l - \varepsilon_a))} \tag{3.15}$$

The 'useful' force component F_R is expressed by

$$F_R = F_Z - F_l \tag{3.16}$$

3.2.2 Lateral restriction forces

If the rotor moves by δ, parallel to the electrode array, then the "air-gap" g necessary to describe the attraction forces is no longer a constant. The attraction force between charges decreases when separation between charges arises (equation 1.1). Trigonometry leads immediately to

$$g \Rightarrow \sqrt{g^2+\delta^2} \tag{3.17}$$

a term which replaces g in equations 3.12 – 3.16. The increase of the lateral restriction force due to the displacement leads to the expression for the lateral restriction force F_X:

$$F_X = \sin\left(\frac{\delta}{g}\right)\cdot F_R\Big|_{g\Rightarrow\sqrt{g^2+\delta^2}} \tag{3.18}$$

Equation (3.18) describes the lateral restriction force due to one pair of electrodes, such as the ones depicted in figure 3.4. Extending to three phased motor electrodes:

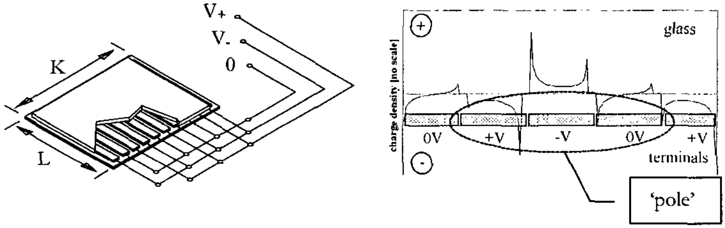

Fig. 3.7 Extension to three phased motor electrode

The number of electrode stripes for a given glass rotor of dimension K:

$$\frac{K}{3(w+d)} = n \in INTEGER \tag{3.19}$$

Each pole is constituted of a positive, a negative and a grounded electrode. Equation (3.17) describes the 'useful' force developed by a negative and a positive electrode. Multiplied by the number of poles ($m = n/3$), we obtain the total force due to all positive and negative electrodes. The influence of the grounded electrode must also be considered: Since the potential difference between positive and ground or negative and ground is half the potential difference between positive and negative, its contribution is one fourth (because of the square law) and we find for the lateral restriction force attributable to one pole:

$$F_{X,pole} = \left(1 + \frac{1}{4} + \frac{1}{4}\right) \cdot \sin\left(\frac{\delta}{g}\right) \cdot F_R\Big|_{g \Rightarrow \sqrt{g^2+\delta^2}} = \frac{3}{2} \cdot \sin\left(\frac{\delta}{g}\right) \cdot F_R\Big|_{g \Rightarrow \sqrt{g^2+\delta^2}} \tag{3.20}$$

and therefore for the lateral restriction force acting on the glass plate of figure 3.7:

$$F_{X,plate} = n \cdot F_{X,pole} = \frac{K}{2(w+d)} \cdot \sin\left(\frac{\delta}{g}\right) \cdot F_R\Big|_{g \Rightarrow \sqrt{g^2+\delta^2}} \tag{3.21}$$

3.2.3 Torque

Figure 3.8 shows the relevant parameters for a rotary electrostatic glass actuator:

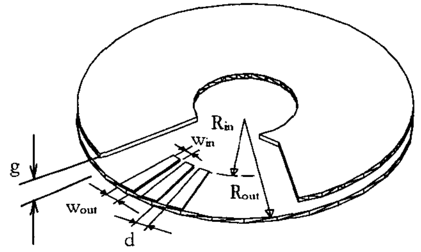

Fig. 3.8 Geometrical parameters of rotary electrostatic glass actuators

The outer radius of the glass disc R_{out}, which also represents the maximum radius of the electrode-stripes. The width of the electrode-stripes at its maximum w_{out} , its minimum w_{in} and the gap between two electrodes d. Also, the inner radius of the electrode R_{in} and the air-gap between the glass disc and the electrode g. Obviously, the geometric parameters of the electrode are not mutually independent.

We call the total number of electrodes n and the total number of poles (three electrodes form one pole for a three phased excitation) m. For illustration, figure 3.9 shows some possible electrode arrangements:

n = 180, m = 60 n = 90, m = 30 n = 30, m = 10

Fig. 3.9 Different electrode arrangements. Different voltages are indicated by different gray levels. The inner radius depends on the track density.

The gap d between two electrodes depends on the applied voltage. In order to have a maximal electric field and therefore a maximal torque, the gap d is close to the breakdown gap where electric breakthrough occurs. It can be observed that the length of the electrodes varies with their number. In other words, if one uses a few poles, the active electrostatic surface is greater than if one uses many poles.

Observing figure 3.8, it is obvious that the smallest possible terminal width w_{in} (function of the fabrication process and prevention of sparking–edge-effect breakthrough) links the gap d with the inner radius R_{in}:

$$2\pi R_{in} = n(d + w_{in}) \Rightarrow R_{in} = \frac{n(d + w_{in})}{2\pi} \tag{3.22}$$

Three electrodes form one pole. Be m the number of poles, we can write

$$m = \frac{n}{3} \tag{3.23}$$

Equation (3.21) describes the lateral restriction force due to one pole of linear geometry in function of a displacement *δ*.

For a circular geometry, the precise analytical result (if one takes into account the real shape of the electrodes) is too complex to be of any use, so some approximations have to be made:

- The electrode width *w* is constant over the whole radius, as well as the displacement *δ*.
- The value of *w* is set to the width at the middle of the active surface, as illustrated by figure 3.10:

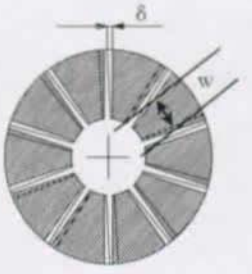

Fig. 3.10 Assumption that the relative displacement rotor-stator δ and the electrode width are constant over the whole radius

The length of the electrode stripes *L* can be written as

$$L = R_{max} - R_{min} = R_{max} - \frac{n(d + w_{e})}{2\pi} \tag{3.24}$$

We define now the linear force density f_R as follows:

$$f_R = \frac{F_R}{L} \tag{3.25}$$

Using the same reasoning as in equations 3.20 and 3.21, this time integrating over the radius, we find for the torque:

$$dT(r)=\left(\frac{n}{3}+\frac{1}{4}\cdot\frac{n}{3}+\frac{1}{4}\cdot\frac{n}{3}\right)rf_{\mathrm{R}}\cdot dr\cdot\sin\left(\frac{\delta}{g}\right)$$
$$=\sin\left(\frac{\delta}{g}\right)\cdot\frac{nf_{\mathrm{R}}r}{2}dr \tag{3.26}$$

$$T=\int_{Rin}^{Rout} dT(r)\cdot dr \tag{3.27}$$

Combining equations 3.13 to 3.27, the torque can finally be computed

$$dT=\sin\left(\frac{\delta}{g}\right)\frac{nf_{\mathrm{R}}r}{2}dr=\frac{1}{2}\sin\left(\frac{\delta}{g}\right)\left(\frac{F_Z-F_I}{\mathrm{L}}\right)r\cdot dr \tag{3.28}$$

with

$$F_Z=\frac{4\mathrm{L}V^2w\varepsilon_a\Psi(t)\left(\varepsilon_a-\Psi(t)\right)}{\left(\pi\varepsilon_a(d+2w)-4\sqrt{g^2+\delta^2}\left(\varepsilon_a-\Psi(t)\right)\right)\left(d\pi\varepsilon_a+4\sqrt{g^2+\delta^2}\left(\Psi(t)-\varepsilon_a\right)\right)}$$

$$\Psi(t)=\varepsilon_I+\left(\varepsilon_H-\varepsilon_I\right)\cdot t^{1-\alpha}$$

$$F_I=\frac{4\mathrm{L}V^2w\varepsilon_a\varepsilon_I\left(\varepsilon_a-\varepsilon_I\right)}{\left(\pi\varepsilon_a(d+2w)-4\sqrt{g^2+\delta^2}\left(\varepsilon_a-\varepsilon_I\right)\right)\left(d\pi\varepsilon_a+4\sqrt{g^2+\delta^2}\left(\varepsilon_I-\varepsilon_a\right)\right)}$$

$$\Rightarrow T=\frac{\left(\mathrm{R}_{out}-\mathrm{R}_{in}\right)^2}{4\mathrm{L}}\cdot\left(F_Z-F_I\right)\sin\left(\frac{\delta}{g}\right)=\frac{\mathrm{R}_{out}-\mathrm{R}_{in}}{4}\cdot\left(F_Z-F_I\right)\sin\left(\frac{\delta}{g}\right)$$

$$\boxed{\Rightarrow T=\frac{\mathrm{R}_{out}-\dfrac{n\left(d+w_{in}\right)}{2\pi}}{4}\cdot\left(F_Z-F_I\right)\sin\left(\frac{\delta}{g}\right)} \tag{3.29}$$

3.2.4 Simplification

The “exact” analytical model (some approximations and hypothesizes have been made in figure 3.3 and equations (3.7), (3.8) and (3.9)) is based on the difference between the total attraction force and the instantaneous attraction force, as stated by equation (3.17):

$$\begin{aligned} &F_R = F_Z(t,\delta) - F_I \\ &T(t,\delta) \propto F_R \\ &F_X(t,\delta) \propto F_R \end{aligned} \tag{3.30}$$

The torque T (rotary actuator) and lateral force F_X (linear actuator) are proportional to this difference, as suggested by equations (3.21) and (3.29). The exact expression for F_R is:

$$F_R = 4LV^2 w\varepsilon_a \left(\begin{array}{c} \dfrac{\left(\varepsilon_I + (\varepsilon_H - \varepsilon_I)\cdot t^{1-\alpha}\right)\left(\varepsilon_a - \left(\varepsilon_I + (\varepsilon_H - \varepsilon_I)\cdot t^{1-\alpha}\right)\right)}{\left(\pi\varepsilon_a(d+2w) - 4\sqrt{g^2+\delta^2}\left(\varepsilon_a - \left(\varepsilon_I + (\varepsilon_H - \varepsilon_I)\cdot t^{1-\alpha}\right)\right)\right)} \cdot \\ \dfrac{1}{\left(d\pi\varepsilon_a + 4\sqrt{g^2+\delta^2}\left(\left(\varepsilon_I + (\varepsilon_H - \varepsilon_I)\cdot t^{1-\alpha}\right) - \varepsilon_a\right)\right)} - \\ \dfrac{\varepsilon_I(\varepsilon_a - \varepsilon_I)}{\left(\pi\varepsilon_a(d+2w) - 4\sqrt{g^2+\delta^2}(\varepsilon_a - \varepsilon_I)\right)\left(d\pi\varepsilon_a + 4\sqrt{g^2+\delta^2}(\varepsilon_I - \varepsilon_a)\right)} \end{array} \right) \tag{3.31}$$

not quite an agreeable expression to work with. Since all components have a similar order of magnitude, equation (3.31) cannot be simplified as it is.

A mathematical approach shall help to condense (3.31):

First, the various permittivities are multiples of ε_a

$$\begin{aligned} &\varepsilon_I = \phi \cdot \varepsilon_a \\ &\varepsilon_H = \eta \cdot \varepsilon_a \end{aligned} \tag{3.32}$$

applied to (3.31):

$$F_Z = 4LV^2 w\varepsilon_a \left(\begin{array}{c} \dfrac{\left(\phi + (\eta - \phi)\cdot t^{1-\alpha}\right)\left(1 - \phi - (\eta - \phi)\cdot t^{1-\alpha}\right)}{\left(\pi(d + 2w) + 4\sqrt{g^2 + \delta^2}\left(-1 + \phi + (\eta - \phi)\cdot t^{1-\alpha}\right)\right)} \cdot \\ \dfrac{1}{\left(d\pi + 4\sqrt{g^2 + \delta^2}\left(-1 + \phi + (\eta - \phi)\cdot t^{1-\alpha}\right)\right)} - \\ \dfrac{\phi(1 - \phi)}{\left(\pi(d + 2w) + 4\sqrt{g^2 + \delta^2}(-1 + \phi)\right)\left(d\pi + 4\sqrt{g^2 + \delta^2}(-1 + \phi)\right)} \end{array} \right) \tag{3.33}$$

Which is not much better than (3.31). Further transformations lead to an expression of the form

$$F_Z = K\frac{(a + bx)(c + dx)}{(e + fx)(g + hx)} \tag{3.34}$$

with

$$\begin{aligned} &x = t^{1-\alpha} \\ &K = 4LV^2 w\varepsilon_a \\ &a = \phi \\ &b = \eta - \phi \\ &c = 1 - \phi \\ &d = \phi - \eta \\ &e = 2\pi w + \pi d + 4\sqrt{g^2 + \delta^2}(\phi - 1) \\ &f = 4\sqrt{g^2 + \delta^2}(\eta - \phi) \\ &g = \pi d + 4\sqrt{g^2 + \delta^2}(\phi - 1) \\ &h = 4\sqrt{g^2 + \delta^2}(\eta - \phi) \end{aligned}$$

Equation (3.34) admits a horizontal asymptote.

With the intention to simplify (3.34), the following polynomial fraction formulation is proposed:

$$F_Z = K\underbrace{\frac{(a+bx)(c+dx)}{(e+fx)(g+hx)}}_{\psi(x)} \approx K\underbrace{\frac{A+Bx}{C+Dx}}_{\theta(x)} \tag{3.35}$$

We impose the following conditions to the approximation *θ(x)*:

1. *θ(x)* passes through 0 for $x=0$:

$$\begin{aligned}&\psi(0)=\theta(0)=0\\ &\Rightarrow A=0\\ &\Rightarrow \theta(x)=\frac{Bx}{C+Dx}=\frac{x}{\frac{C}{B}+\frac{D}{B}x}\end{aligned} \tag{3.36}$$

2. *θ(x)* and *ψ(x)* have the same derivation at $x=0$:

$$\begin{aligned}&\psi'(0)=\theta'(0)=0\\ &\Rightarrow \frac{bceg+daeg-acfg-aceg}{e^2g^2}\overset{A=0}{=}\frac{B}{C}\end{aligned} \tag{3.37}$$

3. *θ(x)* and *ψ(x)* pass through the same point at $x=T$:

$$\begin{aligned}&\psi(T)=\theta(T)\\ &\Rightarrow \frac{(a+bT)(c+dT)}{(e+fT)(g+hT)}\overset{A=0}{=}\frac{BT}{C+DT}\\ &\Rightarrow \frac{D}{B}=\frac{(e+fT)(g+hT)}{(a+bT)(c+dT)}-\frac{1}{T}\frac{C}{B}\end{aligned} \tag{3.38}$$

Combining (3.36), (3.37) and (3.38), we find for the approximated function *θ(x)*:

$$\theta(x)=\frac{Kx}{\frac{e^2g^2}{bceg+daeg-acfg-aceg}\left(1-\frac{x}{T}\right)+\frac{(e+fT)(g+hT)}{(a+bT)(c+dT)}x} \tag{3.39}$$

After introduction and elementary simplification based on orders of magnitude ($w \ll \eta$ etc.), (3.39) becomes an approximation of F_R:

$$F_R = \frac{4LV^2 w \varepsilon_a t^{1-\alpha}}{\frac{\pi^2(\eta-\phi)}{2\phi-1}\left(1-\frac{t^{1-\alpha}}{T}\right)+\frac{\pi\left(\pi(\eta-\phi)-8T\sqrt{g^2+\delta^2}(\eta-\phi)\right)}{T\left(T(\eta-\phi)+2\phi\right)}t^{1-\alpha}} \tag{3.40}$$

An expression that is rather compact compared to (3.31) or (3.33) and that approaches these equations quite well, as shown in figure 3.11. Compared are the "exact" model (3.31), its approximation (3.40), their mutual difference and the ratio *Model / Approximation* from $t \in [0, 200]$ seconds, describing the dynamic of the force due to the induced charge during the first 200 seconds.

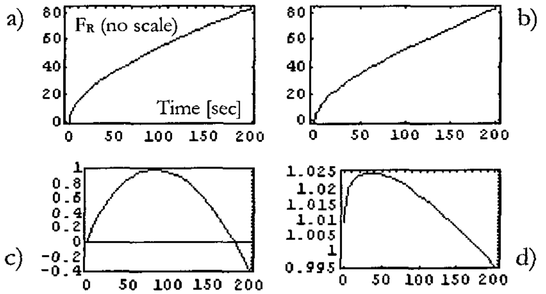

Fig. 3.11 Validation of model approximation. a) Exact model, b) Simplified model, c) Difference between model and simplification, d) Ratio of model and simplification

The force axis is not to scale, since the parameters ε_H and ε_I need to be determined experimentally and differ from glass to glass. For the comparison of figure 3.11, the parameters were arbitrary since they do not influence the allure of the force dynamic.

Equation (3.40) allows a compact formulation of the forces and torques that drive electrostatic glass motors.

For the linear actuator, the lateral force F_x, as a function of a lateral displacement due to the applied moving field becomes (by introducing (3.21)):

$$F_{X,plate} = \frac{\dfrac{K}{2(w+d)} \cdot \sin\left(\dfrac{\delta}{g}\right) \cdot 4LV^2 w \varepsilon_a t^{1-\alpha}}{\dfrac{\pi^2(\eta-\phi)}{2\phi-1}\left(1-\dfrac{t^{1-\alpha}}{T}\right)+\dfrac{\pi\left(\pi(\eta-\phi)-8T\sqrt{g^2+\delta^2}(\eta-\phi)\right)}{T\left(T(\eta-\phi)+2\phi\right)}t^{1-\alpha}} \tag{3.41}$$

This is the force a glass plate of dimensions *L* x *K* experiences when it is displaced by *δ*.

For the rotary actuator, the torque *T*, as a function of a rotary displacement due to the applied moving field becomes (by introducing (3.29)):

$$T = \frac{\dfrac{R_{out}-\dfrac{n(d+w_{in})}{2\pi}}{4} \sin\left(\dfrac{\delta}{g}\right) 4LV^2 w \varepsilon_a t^{1-\alpha}}{\dfrac{\pi^2(\eta-\phi)}{2\phi-1}\left(1-\dfrac{t^{1-\alpha}}{T}\right)+\dfrac{\pi\left(\pi(\eta-\phi)-8T\sqrt{g^2+\delta^2}(\eta-\phi)\right)}{T\left(T(\eta-\phi)+2\phi\right)}t^{1-\alpha}} \tag{3.42}$$

Experimental validation of these findings is the goal of the following chapter.

3.3 Viscoelastic creep

The physics that allow the propulsion of a glass rotor are linked to a very slow charge-creep through the glass. It was already mentioned in section 2.2 that in literature this phenomenon is compared to elastic strain to follow an applied stress (Hooks law is a simplified description of such phenomena).

In the direction parallel to the rotor plate, a similar phenomenon is also introducing a kind of viscoelasticity into the system (figure 3.12):

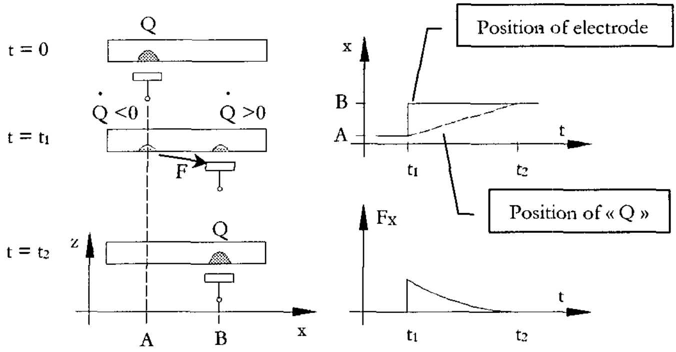

Fig. 3.12 Viscoelastic behavior of the electrostatic glass motor

On the left hand side of figure 3.12 is schematized the case of a live electrode facing a glass plate. The electrode is kept in place for some tens of seconds, so charges will appear of the glass (designated by *Q*). This charge dynamic and the resulting attraction force in *z*-direction are accurately described by equation (3.29).

In the presented model, the charges were supposed to be static, once they have been induced. Static in terms of position on the glass rotor, so the rotor was supposed to follow perfectly synchronously the moving field. Measurements confirmed the accordance between rotation speed and field speed, thus validated this hypothesis for most applications. In very precise positioning, however, the impact of this hypothesis should not be underestimated:
If the live electrode is displaced from place *A* to place *B* (see figure 3.12), and the glass plate remains at its initial position, then the charges at the old position *A* will start to decrease and the glass region now opposite to the electrode (at position *B*) is subjected to an increase of charges (schematized by "*dQ/dt*" and arrows indicating decrease and increase, respectively). The net result of these charge dynamics is, that the force component in *x* direction (the force that makes the electrostatic glass motor work), is decreasing. After some time the charge at the old location *A* completely disappeared and the identical quantity of charges is now at location *B*. The exponential nature of the charge dynamics (equation 2.12), which are responsible for forces in *z* direction, lead to the assumption that this force decrease in *x* direction behaves exponential, as well. The "center of inertia" of the induced charges

follows the electrode, but slowly. Figure 3.12 sketches at the right hand side the evolution of the charge position with time, and the evolution of the exploitable force, F_x, with time.

Observing the force and position variations, it can be concluded that the glass-charges behave very much like a Maxwell fluid [31]. Reemploying the analogy of stress analysis, the glass motor seems to have the capability of unlimited deformation under finite stress. Its response immediately after load application is elastic with a certain modulus.

Viscoelastic behavior (the observed material exhibits properties characteristic of both a solid and a fluid) is phenomenologically modeled by Hookean springs and Newtonian dashpots (figure 3.13):

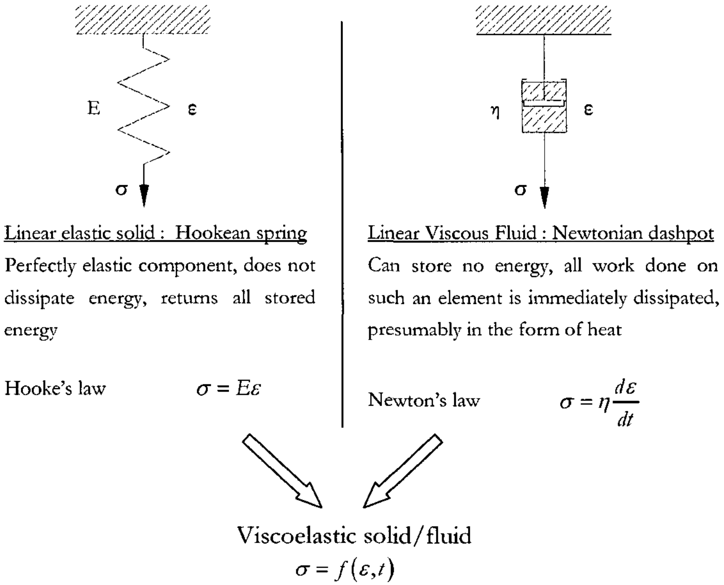

Linear elastic solid : Hookean spring

Perfectly elastic component, does not dissipate energy, returns all stored energy

Hooke's law $\sigma = E\varepsilon$

Linear Viscous Fluid : Newtonian dashpot

Can store no energy, all work done on such an element is immediately dissipated, presumably in the form of heat

Newton's law $\sigma = \eta \dfrac{d\varepsilon}{dt}$

Viscoelastic solid/fluid

$\sigma = f(\varepsilon, t)$

Fig. 3.13 Basic elements for viscoelactic analysis

The traditional stress analysis variables have been used: ε designates strain [%], E the Young modulus [N/m^2], σ the stress [N/m^2] and η the viscosity [Ns/m^2].
These elements, connected in series (Maxwell models) or in parallel (Voigt models), provide a black-box treatment of the differential equations and corresponding mechanical analogs which can be used to describe time dependant behavior.

The Maxwell fluid element consists of a Hookean spring and a Newtonian dashpot combined in series. Both are subjected to the same stress, and the total strain in the Maxwell element is equal to the sum of the strains in the spring and dashpot (figure 3.14):

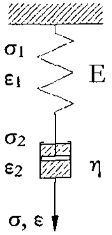

Equilibrium $\sigma_1 = \sigma_2 = \sigma$

Strain compatibility $\varepsilon = \varepsilon_1 + \varepsilon_2$

Governing equation $\dot{\varepsilon} = \dfrac{\dot{\sigma}}{E} + \dfrac{\sigma}{\eta}$ (3.43)

Fig. 3.14 Maxwell fluid element

The two viscoelastic phenomena are creep (and creep recovery) and stress relaxation. By creep we understand the delayed time-dependant relaxation that follows an initial instantaneous elastic deformation when a viscoelastic material is subjected to an instantaneous load. It is the property that is of interest for the electrostatic glass motor, since it determines the 'relative' creep between the moving electrostatic field and the moving glass rotor. This phenomena is difficult to measure, since in the case of electrostatic glass motors, no physical elongation is the manifestation of creep, but the movement of charges. However, there is a way to quantify the creep: The characteristic parameters of the Maxwell fluid model (Young modulus and viscosity) can be determined by measuring the stress relaxation. Stress relaxation involves the instantaneous application of strain, which is held steady whilst the stress in the material is observed. Under these conditions the stress increases instantaneously and then relaxes slowly over a period of time to some steady-state value. Stress relaxation is easily measurable using a dynamometer.

The Maxwell model solution for stress relaxation (assumption of a constant strain) becomes for equation (3.42):

$$\frac{\dot{\sigma}}{E}+\frac{\sigma}{\eta}=0 \tag{3.44}$$

Integration (given $\sigma = E\cdot\varepsilon_0$ at $t = 0$)

$$\sigma = E\varepsilon_0 \exp(-\frac{t}{\tau}) \quad \text{with} \qquad \tau=\frac{\eta}{E} \tag{3.45}$$

The Young modulus E is easily determined once the applied strain is known (the instantaneous stress leads directly to E through Hook's law). Since the time constants of the charge dynamics and of the stress relaxation must be identical, equation (3.41) and equation (3.44) allow the determination of the viscosity.

The resulting creep is determined as follows: The Maxwell model solution for creep (assumption of a constant stress) becomes for equation (3.42):

$$\dot{\varepsilon}=\frac{\sigma_0}{\eta} \tag{3.46}$$

Integration with respect to time leads to

$$\varepsilon=\frac{\sigma_0}{\eta}t+const \tag{3.47}$$

When $t = 0$, $\varepsilon = \sigma_0 / E$, therefore

$$\varepsilon=\frac{\sigma_0}{\eta}t+\frac{\sigma_0}{E} \tag{3.48}$$

Which is the creep between glass rotor and motor field, measured in percent, in function of time.

The analogy between viscoelastic materials and our electrostatic glass motor is presented in figure 3.15 for the phenomenon of stress relaxation:

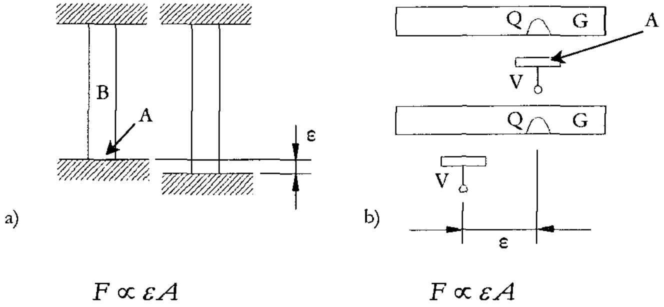

Fig. 3.15 Analogy of stress relaxation for a) viscoelastic materials and b) the electrostatic glass motor.

In the case of a viscoelastic bar B, the force that acts inside the specimen once it is stretched by an amount ε is proportional to the bar surface A (and on the material properties, of course). On the other hand, the force that acts on a glass plate G once it is shifted by an amount ε is proportional to the electrode surface A (and of the applied voltage).
The term of force F [N] is used in this context. The concept of stress σ [N/m^2] cannot be matched directly, due to the different nature of the involved surfaces. However, by multiplication with the electrode surface A, equations (3.43) to (3.37) can be adapted to electrostatic glass motors. Stress (force) relaxation becomes:

$$F(t) = AE\varepsilon_0 \exp(-\frac{t}{\tau}) \text{ with } \tau = \frac{\eta}{E} \qquad \text{[N]} \qquad (3.49)$$

And creep can be written as:

$$\varepsilon(t) = \frac{1}{A}\left(\frac{F_0}{\eta}t + \frac{F_0}{E}\right) \qquad [\%] \qquad (3.50)$$

3.4 Synthesis

The analytical models established in this chapter lead to the complete dynamic model of the electrostatic glass motor, sketched in figure 3.16:

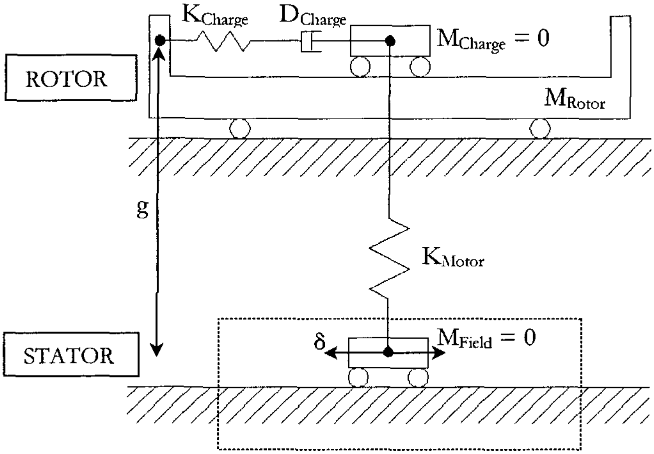

Fig. 3.16 Coupled oscillator modeling the electrostatic glass motor.

Inside the dashed box is represented the motor field. Its lateral displacement δ, forces the rotor (supported on a supposed frictionless bearing) to follow suit via the mutual attraction force due to K_{Motor}. (can be derived from equation (3.29) or, simplified, from equation (3.41)).

The force F_X due to K_{Motor} is the force that acts on the Maxwell fluid element on the rotor. Experiments on stress relaxation allow the determination of K_{Charge} (via the "Young modulus" of glass charges), and the damping coefficient D_{Charge} can be computed using the fact that the time constant of stress relaxation equals the one of charge induction (equation 3.29), allowing the determination of the "viscosity" of glass charges.

Note that figure 3.16 is schematic. In reality, the M_{Rotor}-wagon would have an infinite extension (circular geometry).

IV. Experimental verification

4.1 Force measurement setup

Force measurements involving inherently unstable square laws, such as those that govern electrostatic and electromagnetic attraction, need an actively regulated dynamometer guaranteeing a constant air-gap. A flexible hinge structure regulated by a voice coil magnetic bearing was chosen. Figure 4.1 sketches the experimental setup:

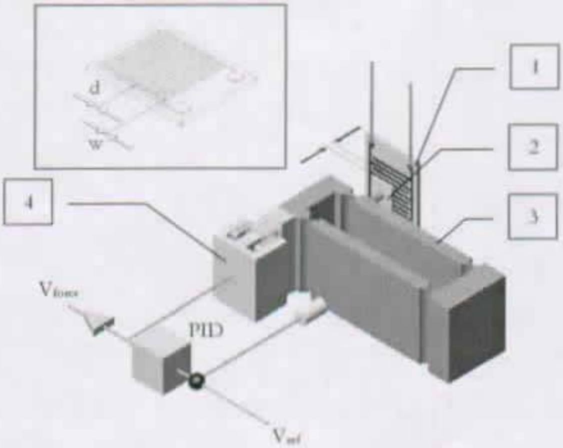

Fig.4.1 Active regulated force sensor. The inlet shows the parameters of the test electrodes.

A two phased electrode **1** fabricated with standard printed circuit board techniques is facing the glass specimen **2**, mounted with a gap *g* between electrode and glass. This glass specimen is mounted on the flexible hinge structure **3**, which is actuated by a voice coil actuator **4**. Regulated by a standard PID feedback loop, the applied control signal is proportional to the electrostatic attraction force. The voltage applied to the electrode are kept at DC level. The electrode surface is 4 cm^2, the glass specimen surface 1 cm^2. A photo of the realized force sensor is shown in figure 4.2:

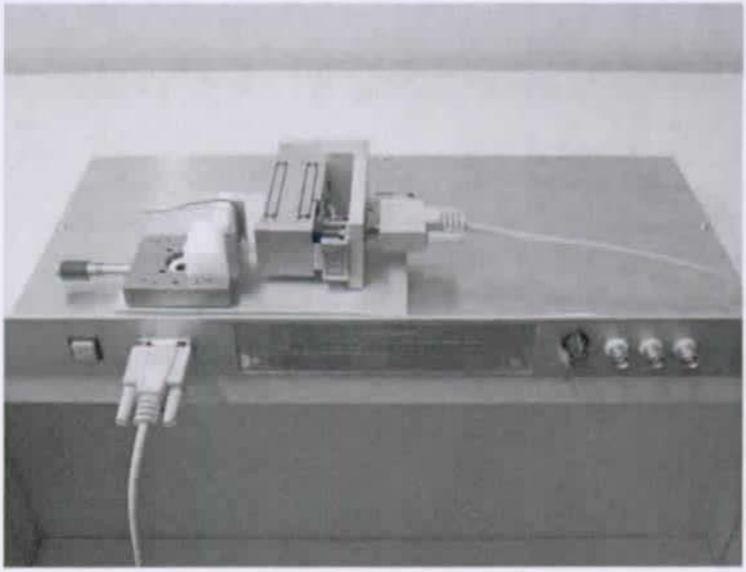

Fig.4.2 Photo of the force sensor with its control box. The dSPACE regulator is not shown.

The force sensor was used in two different configurations: For the measurement of F_R, the setup is identic to the one of figure 4.2. For the measurement of F_X, a linear drive was added in order to deplace the glass specimen parallel to the electrode.

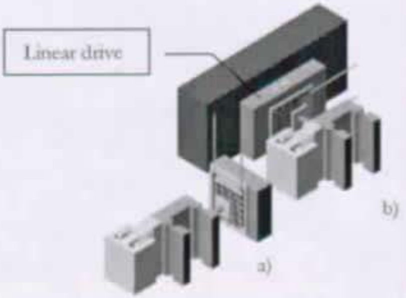

Fig.4.3 a) Measurement of F_R b) measurement of F_X

4.2 Attraction force experiments

4.2.1 Electrode configuration

Twenty different electrode configurations have been tested. Track width *w* and inter-track distance *d* varied from 0.2 mm to 0.8 mm. The developed forces are compared to the attraction force produced by a plain copper plate at a potential of 1000 Volt. Figure 4.4 plots the measurements:

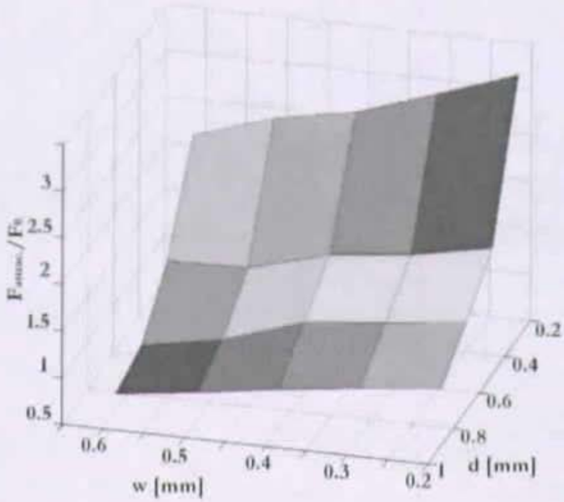

Fig.4.4 Determination of optimal electrode parameters. The reference F_0 indicates the attraction force produced by a plain copper sheet. Soda-lime glass. Applied voltage 1000V.

It can be seen that the electrode with the thinnest tracks and the highest track density produces the biggest attraction force, up to three times higher than the force produced by a plain conductor. This important result shows the importance of the track boundaries for the electrostatic glass motor. If the target is a conductor, the plain electrode would produce the maximal attraction force. In the case of a glass target, for a maximal attraction force, the thinnest possible tracks are advantageous.

4.2.2 Charge dynamics for different glass blends

Preliminary measurements (figure 3.6) showed that the final polarization state of a soda-lime glass specimen was not reached after more than 10 minutes. Lacking an asymptotical value, we use the model of (3.14) to describe the charge dynamics of different glass blends. The model describes the physical reality very well:

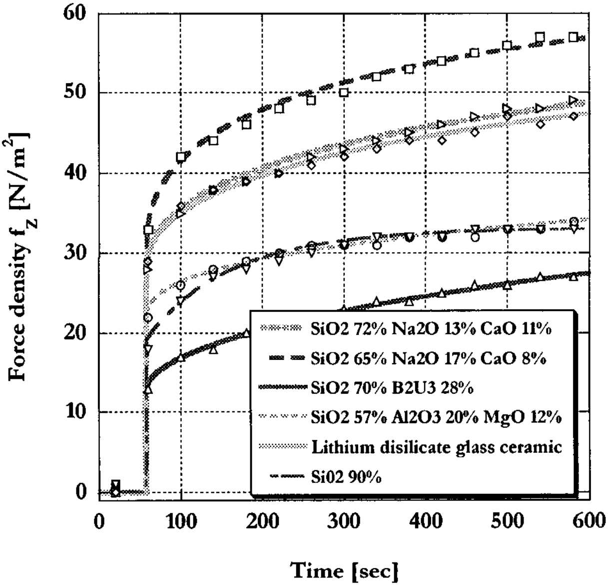

Fig.4.5 Model versus measurement for the most common glass blends. Measurement of attraction force-density fz between common glass blends and electrode (d=300μm, w=300μm), applied potential 1000 V, air-gap g = 100μm, RH = 30 %

Of course the simplified model (equation 3.40) describes reality just as well. The tested glass types are representative for the most common blends. Leaded glass is missing, but the impossibility to produce thin wafers out of this blend disqualified it for motor applications. The parameters ε_l, ε_H and α have been determined for each glass type and are given in table 4.1:

Type of glass	α	ε_I	ε_H
SiO_2 72% Na_2O 13%	0.5	4	4.11
SiO_2 65% Na_2O 17%	0.45	4.51	4.63
Glass Ceramic	0.5	4	4.1
SiO_2 57% Al_2O_3 20%	0.65	3	3.16
SiO_2 90%	0.6	3	3.12
SiO_2 70% B_2U3 28%	0.45	2.3	2.35

Tab.4.1 Model parameters for the measured glass blends

The relevant force component for the motor function, F_R, is represented in figure 4.6 as a force density f_R:

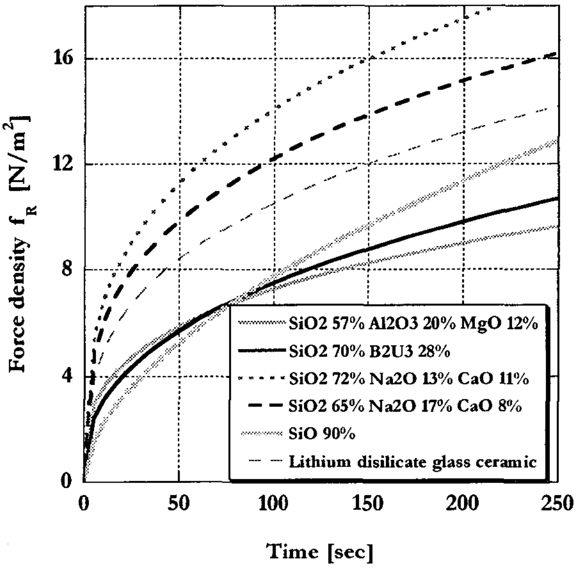

Fig.4.6 Dynamic of f_R for the most common glass blends. Electrode (d=300μm, w=300μm), applied potential 1000 V, air-gap g = 100μm, RH = 30 %

A comparison between the tested glass blends is given in figure 4.7. The reference is the Lithium disilicate glass ceramic from the Japanese company OHARA, since this material is commercially available in the form of standard discs for hard disc drives.

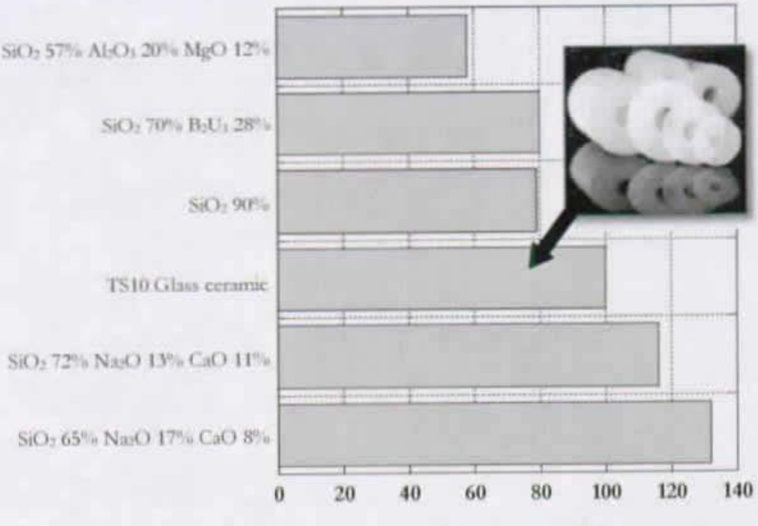

Fig.4.7 Comparison between the measured glass blends. Reference is the OHARA glass ceramic 'TS10'. The inlet shows the commercially available hard disc substrates made of TS10.

We conclude that, by using a blend of Soda-lime glass, the motor forces can be augmented by 30%, compared to the commercial TS-10 material. Soda-lime glass is easily machinable and comes in various thicknesses (down to 0.13 mm for microscope object cover plates).

4.2.3 Influence of the glass rotor thickness

The influence of the glass rotor thickness is a parameter that was not included into the model. Equation (3.14) and following developments are based on the assumption of an infinite thick glass rotor. We carried out two experiments to determine the influence of the glass thickness on the produced attraction force. The first test consisted of measuring the attraction force as a function of the thickness for soda-lime glass; the attraction force was measured after 100 seconds of charging for all specimens.

Figure 4.8 shows the results, as well as exponential fits. Three different electrode types were measured.

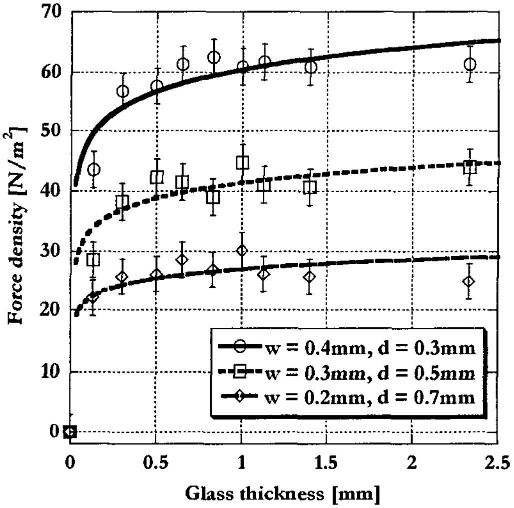

Fig.4.8 Attraction force density versus glass thickness for three different electrodes. The superimposed curve fits suggest an exponential allure.

As intuition suggests, the force tends asymptotically towards a limit with growing glass thickness. For electrodes that are interesting for motor applications, glass rotors thicker than 0.5 mm seem not to further improve the attraction force.

The second experiment investigated whether the charge dynamics of the glass rotor are influenced by the glass thickness. We measured the attraction force versus time by using only one electrode (*d* = 300 μm, *w* = 300 μm). Figure 4.9 plots the measurements. It can be seen that the charge dynamics are effectively influenced by the glass thickness. With increasing glass thickness, the polarization progresses faster, thus the motor force occurs sooner, as well. Again, a rotor thickness over 0.5 mm seems not to be interesting for our application. Thicker rotors only increase inertia, but are not polarized any faster.

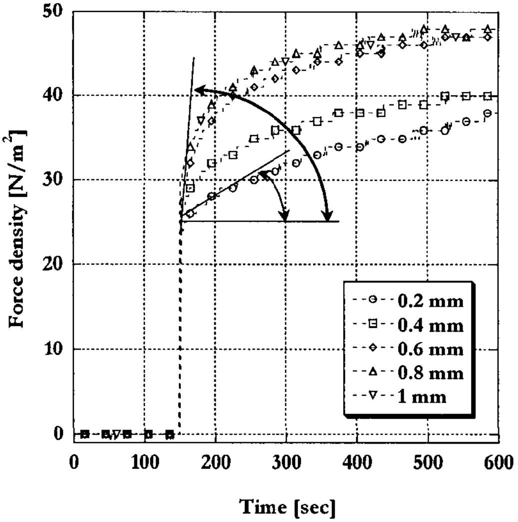

Fig.4.9 Attraction force density versus time for different rotor thickness. The voltage is applied at *t* = 150 sec.

4.2.4 Influence of air-gap

Electrostatic attraction is governed by an inverse square law, analog to the electromagnetic attraction. The special geometry of the electrostatic glass motor does not intuitively lead to the inverse square relation; hence an experimental measurement is needed. Indeed, the model of equation (3.14), which so far has proved to be satisfactorily exact (figure 4.5), predicts an air-gap dependency of the form

$$F(g)=\frac{A}{(B+Cg)(D-Eg)} \tag{4.1}$$

here, *A*, *B*, *C* and *D* being constants. Figure 4.10 plots the measured influence of the air-gap against our model of equation (3.14) and, for comparison, a fitted curve of the form (*Constant*/*g*):

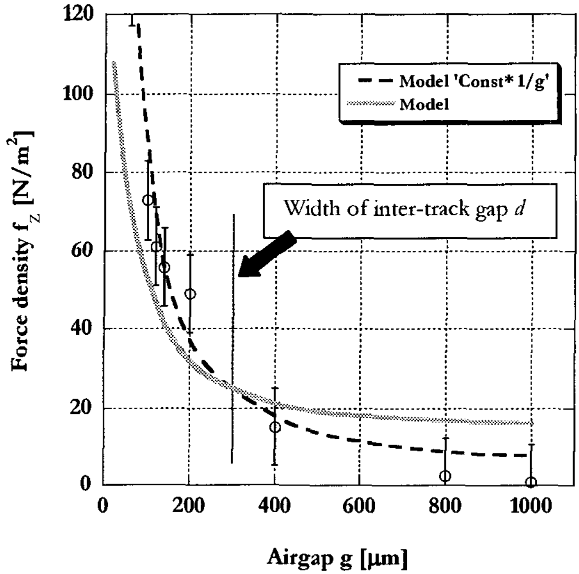

Fig.4.10 Attraction force density versus air-gap for soda-lime glass. The dashed line indicates the inter-track width of the electrode.

It can be seen that the amplitude and the allure given by our model (3.14) are close enough to the physical reality to present a valid tool for the design of electrostatic glass motors. We can explain the discrepancy between model and measure above 200µm air-gap by our model-hypothesis that the air-gap *g* is of about the same magnitude than the inter-track gap *d*.

It is important to note the influence of the air-gap is of the same order of magnitude as the influence of the glass blend. Hence, the flattest possible electrode substrate together with the smallest possible air-gap are imperative for maximizing the performance of the actuator.

4.2.5 Influence of humidity

The surface resistivity of glass is influenced by the humidity as are the charge dynamics and therefore the developed electrostatic attraction forces are a function of the humidity. The charge mobility on the disc increases with humidity, so there exists an optimal humidity with respect to the rotation speed as confirmed by experiment (figure 4.11):

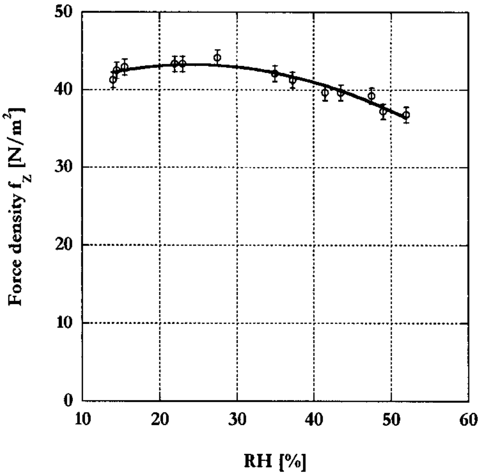

Fig.4.11 Influence of the air humidity on the attraction force density. Measure and second order polynomial fit.

It was observed that for the glass type used, the optimal soda-lime blend, a humidity of 25% seems to present the best balance between charge creation and charge mobility.

4.3 Restriction force experiment

4.3.1 Lateral restriction force

Equation (3.21) models the lateral restriction force if the field moves parallel to the glass rotor. In order to validate our model, we measured the lateral restriction force using a two-phased electrode (figure 4.1) and a modified experimental setup, still using the zero-displacement force sensor. This model seems to be satisfactorily accurate, as it can be seen in figure 4.12.

It can be seen that lateral force densities in the order of newtons per square meter can be obtained. The lateral restriction force equals zero for zero displacements and increases toward a maximum. If the applied motor load is too important (bearing losses, air friction, inertia etc.), the necessary force to drive the load will force the operating point over the maximum, the region where the lateral restriction force is decreasing. This is the point where the rotor loses the field and the synchronous machine stops.

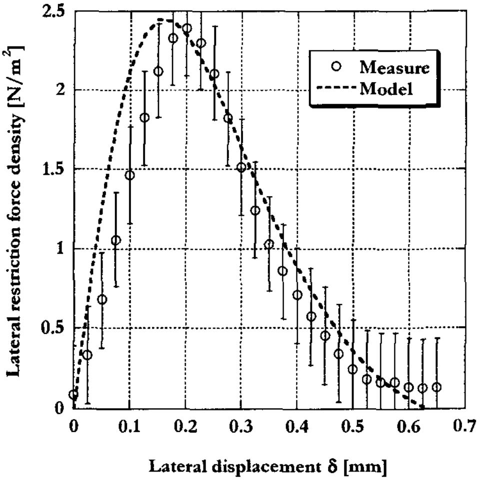

Fig.4.12 Verification of model for the lateral restriction force

4.3.2 Dynamic force / torque

The experimental setup used for the determination of the 'load force/torque' of the electrostatic glass motor is sketched in figure 4.13. By load torque we understand the quantity of torque that is not used for the rotation of the rotor, therefore apt to drive and additional load. It is not the absolute measure of the torque/force (proved to be adequately modeled by (3.21)) that is of interest (depending on glass blend, gap etc.) but the allure of the curve torque-versus-rotorspeed.

A rotary electrostatic glass motor (diameter 65mm) is mounted on a translation-stage. A cylinder mounted on the glass disc **1** is in contact with a thin thread, on both ends of which masses are attached. The heavier mass **4** is on the measure surface of a precision balance **5**, the lighter mass **3** hangs freely. By pushing the spinning disc along the indicated direction, friction is increased, dragging on the mass on the balance. Knowing the radius of the cylinder **1** and the value of gravity, the torque can be computed directly from the mass difference read on the precision balance. The correct value (the searched torque) is displayed when the rotor stops.

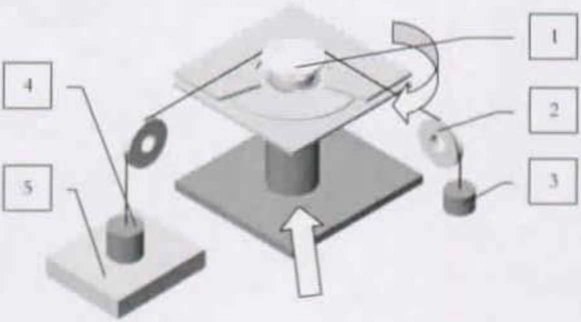

Fig. 4.13 Setup for torque measurement. The arrows indicate displacement and rotation sense.

Figure 4.14 plots the torque versus the rotation speed:

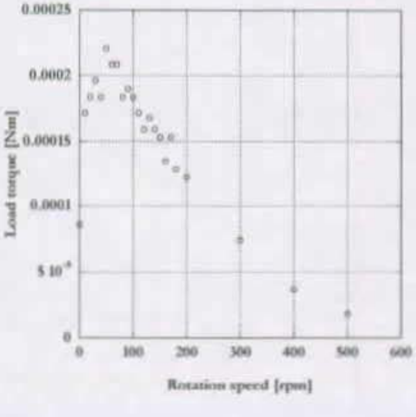

Fig. 4.14 Load torque versus rotation speed

The proposed method (figure 4.13) proved to be adequate for the measurement of small torques and is reported to be used in the DC motor industry for this purpose.

4.4 Visco-elastic creep experiment

The measurement of figure 4.12 (measurement of the lateral restriction force) is also determining all model parameters of figure 3.16, here recapitulated for the sake of convenience:

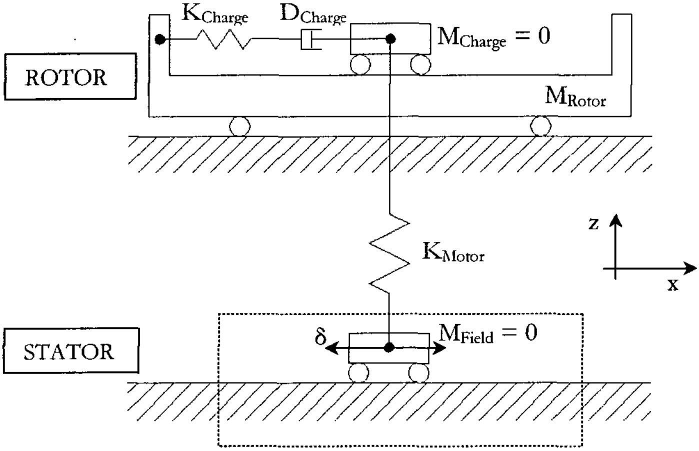

FIG. 4.15 Coupled oscillator modeling the electrostatic glass motor, recapitulation of figure 3.16

The attraction force modeled by the K_{Motor} spring is of course of negative stiffness (inverse square law of electrostatic attraction) but since the gap between glass disc and electrode is fix and we are interested in lateral displacement, the system actually behaves like if there were a positive-stiffness spring hence justifies this approximation.

The force in *x*-direction F_X that acts on the rotor when the stator field moves by an amount of δ can be directly read on the mounting part of graph 4.12, as indicated in figure 4.16.

This force F_X is also the force that acts on the Maxwell fluid element on the rotor. The spring element of the Maxwell fluid will immediately produce the same force (elastic equilibrium) therefore it can be stated that the stiffness of the Maxwell-spring (K_{Charge}) equals the curve of figure 4.12.

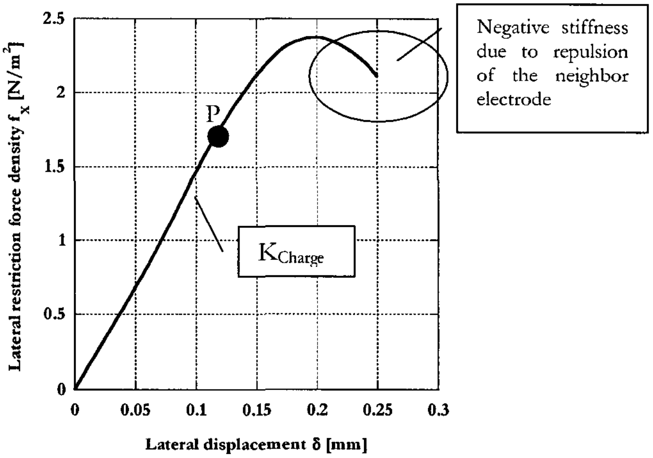

Fig. 4.16 Measure of stiffness per surface unit K_{Charge}, the point P indicates an arbitrary point.

The extension to stiffness per surface unit is explained by the fact that all forces depend on the surface of the glass rotor. The stiffness per surface for soda-lime glass can therefore be estimated to

$$k_{Charge} = 15 \cdot 10^3 \ [\mathrm{N}/(\mathrm{m}^2 \cdot \mathrm{m})] \qquad (4.2)$$

Following the reasoning of section 3.3, the viscosity (or damping) of the Maxwell fluid element can be determined:

The stress relaxation time constant of the visco-elastic model equals the time constant of the charge induction (see figure 3.12), measured in figure 4.5 and 4.6 for the most common glass blends. This time constant is estimated at

$$\tau = 150 \ [\mathrm{sec}] \qquad (4.3)$$

Value that is acceptable for most glass blends (see figure 4.6).

For a 'strain' of 0.1 mm (reminder: analogy to plastic material deformation, the field is displaced by 0.1 mm, equivalent to a strain applied to a bar), the immediate lateral stress-force per glass surface unit will be 1.5 N/m². The surface of the glass specimen is 1 cm², so equation (3.50) leads to the Young modulus per glass surface unit e_{Charge}:

$$e_{Charge} = \frac{k_{Charge}}{A} = 150 \cdot 10^6 \qquad [N/(m^2 \cdot m^2)] \qquad (4.4)$$

Or a ,Young modulus' E of 150 MPa if the glass rotor has a surface of 1m². In this case, K_{Charge} would be $15 \cdot 10^3$ [N/m].

Once the surface of the glass rotor is known, the viscosity can be computed. For a very large rotor of 1m² surface:

$$\eta_{Charge} = \tau E = 22.5 \cdot 10^9 \qquad [Ns/m^2] \qquad (4.5)$$

Of course 1m² big glass rotors are not realistic. The numerical application serves to give a first idea of the order of magnitude.

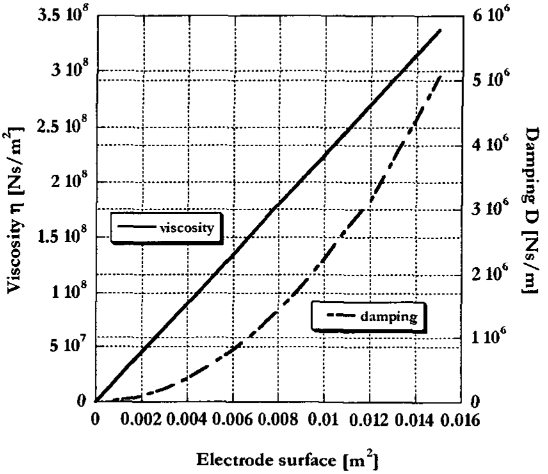

Fig. 4.17 Viscosity and damping versus electrode surface ($d = w = 300\mu m$, g = 100 μm, V = 1kV)

Figure 4.17 plots the viscosity η and the damping D versus the electrode surface for smaller and more realistic glass rotors in the order of several square centimeters. For the Young modulus E and the stiffness K, figure 4.18 plots the same calculation:

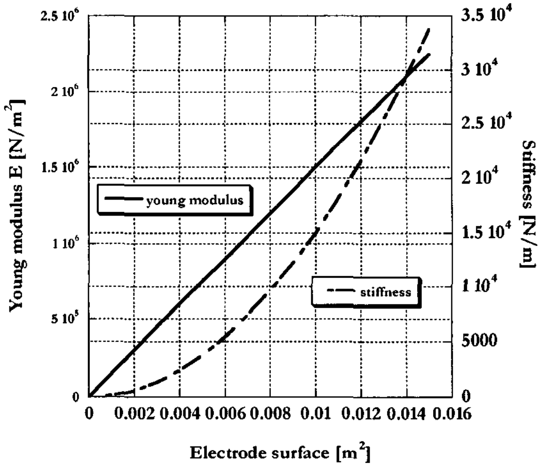

Fig. 4.18 Young modulus and stiffness versus electrode surface (d = w = 300µm, g = 100 µm, V = 1kV)

Table 4.2 compares the viscosity of a 1cm^2 big electrostatic glass actuator with other, familiar viscous materials:

Material	η [Ns/ m^2]
Air	$1.82\cdot10^{-5}$
Ethanol	$1.20\cdot10^{-3}$
Water 0°	$1.79\cdot10^{-3}$
Glycerin	1.48
Polycarbonate 220°	$0.8\cdot10^{4}$
1cm^2 Soda lime glass (*V*=1kV, *w*= *d*= 300um, *g*=100µm)	**$2.25\cdot10^{6}$**
Low viscosity epoxy 25°	$4\cdot10^{6}$
POM technical polymer	$1.44\cdot10^{11}$

Table. 4.2 Viscosity of a small electrostatic glass actuator compared to other viscous materials

These measurements allow the computation of the mutual creep between rotor and stator. Figure 4.19 plots the creep of a typical electrostatic glass actuator with a glass surface of 10cm^2:

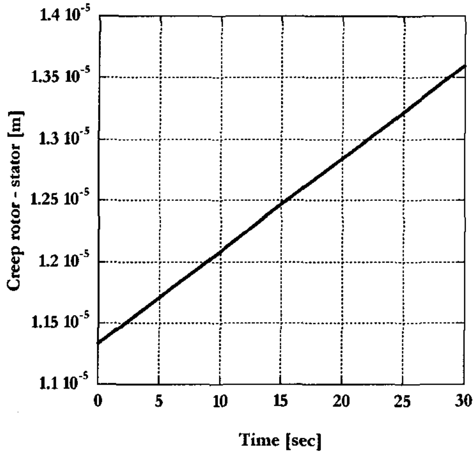

Fig. 4.19 Rotor – stator creep. Rotor – stator displacement δ = 120μm (d = w = 300μm, g = 100 μm, V = 1kV)

It can be concluded that if the described motor is running for 30 seconds (we have no information about the actual speed), and the external loads (air resistance, inertial acceleration etc.) force the rotor to lag 120μm behind the stator field (otherwise there would be no torque), then the glass rotor 'crept' about 2.4μm relatively to the stator field.

This creep is hindering open-loop precise positioning except in the case of a no-load condition (for example the positioning of mirrors or lenses mounted on the glass rotor). The effects of the creep could also be of importance for fast turning electrostatic glass actuators. This is briefly illustrated with the following numerical example: A 5 cm diameter rotary actuator spins at, say, 5000 rpm. Air friction and bearing losses impose a motor force (in the rotary case of course a torque) comparable to the working point P in figure 4.16. This motor must spin for approximately 500 hours (21 days, 3 weeks) until the mutual creep reached one revolution. Hence it is appropriate to speak of a synchronous actuator at least from the engineering point of view.

4.5 Discussion

The performed experiments validated the analytical model.

Using a custom developed actively regulated dynamometer, the delicate measurement of the weak electrostatic force could be performed. Different experimental setups allowed the measurement of the total attraction force and of the lateral restriction force (the moving motor field was simulated by lateral displacement of the test electrode). This allowed the determination of the characteristic permittivities of a set of the most common glass blends. In addition to the validation of the models, other, non-modeled influences, were put in evidence:

It was shown that soda-lime glass blends are most advantageous for motor applications.

Humidity plays a key role in the force-development of electrostatic glass motors. A maximum attraction force was observed for relatively dry air (30% RH).

The model implies an infinite thickness of the glass motor. As intuition suggests, in reality, thickness is an issue. The influence of the thickness was measured to decrease asymptotically, so that for motor applications, a rotor of about 0.5 mm thickness approaches the "infinity" hypothesis.

Being an inductive actuator (even though the induction time constant is so slow that one might think of a stepping motor actuator, there is a visco-elastic creep between rotor and stator (due to the creep of charges inside the glass rotor). This creep was modeled and measured and was shown to be neglectable for fast moving or rotating actuators, but becomes relevant for precise positioning applications, as soon as external loads act on the rotor. Closed loop positioning is the solution that allows the rejection of the errors induced due to this creep.

V. Implementations

5.1 Preliminary prototypes

5.1.1 65 mm single side with ball bearing

First verification of the rotation principle [73] with a commercially available 65mm diameter glass hard disc drive substrate made out of TS-10 ceramic from the Japanese company OHARA. Rotation was observed after application of three-phased sinusoidal and step wave excitations. The maximal rotation speed was around 4500 rpm.

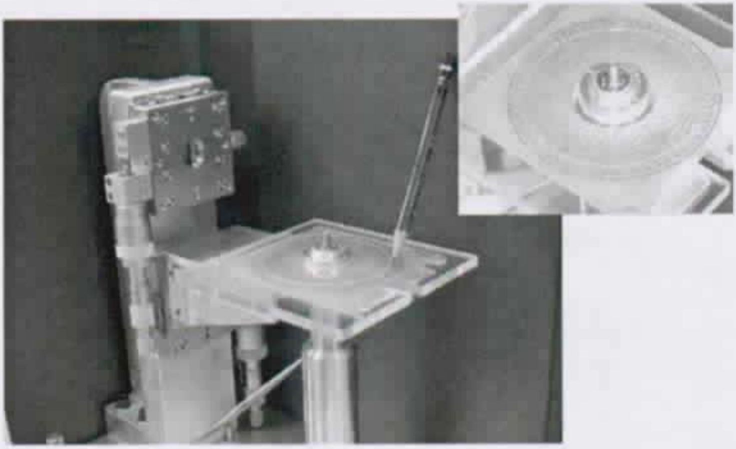

Fig. 5.1 65 mm motor, single side drive, with two ball bearings. Electrode with $n = 180$, $d = 400$ µm. The inlet shows the handmade electrode. Realized at the Higuchi Lab, University of Tokyo.

Using an optical speed probe, the synchronous rotation was confirmed. It was observed that, for a given high voltage supply, the torque (therefore the obtainable speed) can be augmented by 30% if a three-phased step excitation is chosen instead of sinusoidal waves. The resulting cogging on the other side disqualifies this solution for positioning purposes.

5.1.2 65 mm double side with ball bearing

The torque gain obtained by using two electrode arrays that sandwich the glass rotor was examined using the following experimental setup:

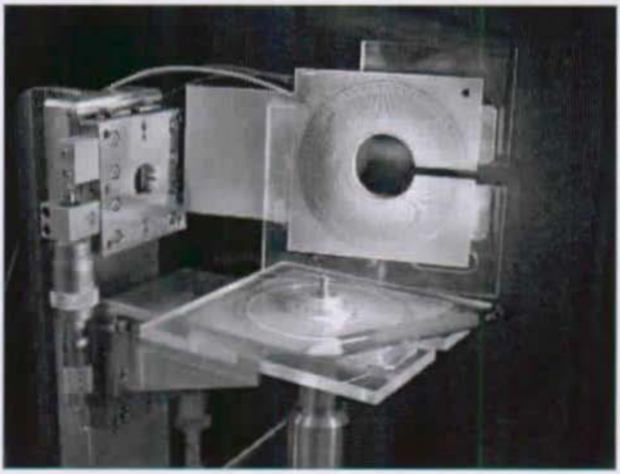

Fig. 5.2 65 mm motor, double side drive, with two ball bearings. Electrode with n = 180, d = 400μm. The motor has been opened for the photograph. Realized at the Higuchi Lab, University of Tokyo.

This motor can be powered in two different ways, the two fields being in phase or out of phase by 120 degrees. It was observed that, if the upper and the lower field are in phase, torque gains up to 100% are possible. On the other hand, if the two fields are out of phase, the torque of such a double side drive is about equal to the torque of the single side drive presented in the previous paragraph.

The maximal obtainable speed of this drive was around 7200 rpm. The dynamic torque in function of the rotation speed was measured and is at its maximum 400 μNm, torque comparable to a 7mm long and 3mm thick brushless DC motor.

The influence of humidity was measured for the first time and we observed a maximal rotation speed as a function of the ambient humidity, an indication of the strong dependency from this parameter.

5.1.3 One inch single side with ball bearing

Based on the previous prototypes, a one-inch single side disc motor was realized, in the context of a feasibility study for potential electrostatic glass motors for hard disc drives in portable devices. Figure 5.3 shows the experimental setup, together with a custom three channel high voltage amplifier:

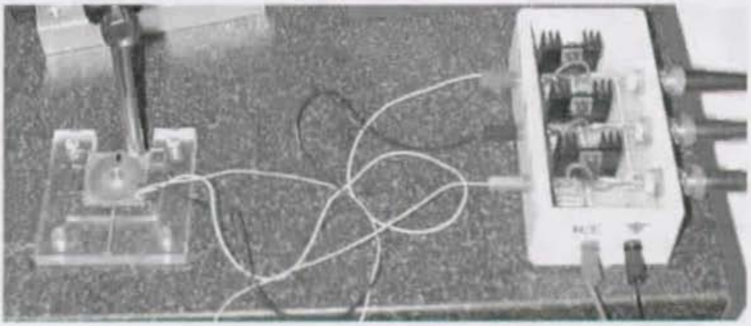

Fig. 5.3 One-inch motor, single side drive, with two ball bearings. Electrode with $n = 60$, $d = 400$ µm. Showed is also a custom three-channel high voltage driver.

This prototype showed that electrostatic glass motors are an interesting alternative to traditional electromagnetic solutions. Rotation speeds of up to 5200 rpm have been observed; the consumed power of the actuator was approximately 0.1 Watt. The simplicity and compactness of the electrostatic glass motor could be a decisive sales point for hard disc drives for handheld applications.

For cost effective miniature hard disc drives, the ball bearings would have to be replaced by a more precise and more compact solution. We proposed a ruby bearing, as used by the watch industry, to reduce the total high of a potential hard disc drive down to 3mm, the dimension of a commercially available flash memory card.

The glass blend used was again the glass ceramic TS-10, produced by the Japanese company OHARA.

5.1.4 65 mm single side with single point bearing

Replacing the ball bearings by a simpler and more cost-effective solution is not an easy task. Actively regulated contact-free suspension is complicated and needs extensive computing power. Static air bearings need external compressors and hydro-bearings are also somewhat encumbering for flat applications like portable hard disc drives. So we replaced the ball bearing with what we call a single point bearing [76]. A pivot (ideally a needle tip, in our prototype a steel ball) is located in a groove in the middle of the rotor. Figure 5.3 shows a prototype and the principle:

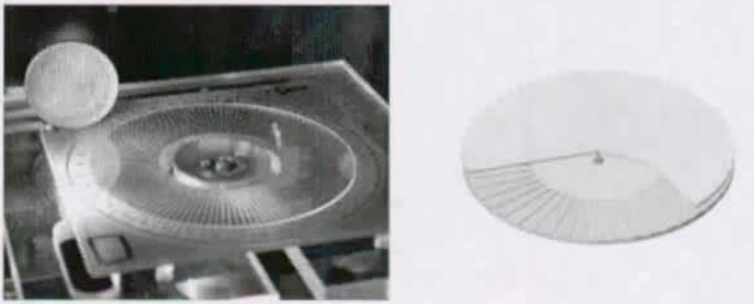

Fig. 5.4 65 mm motor, single side drive, with single point bearing. Electrode with $n = 180$, $d = 400$ µm. The drawing shows the principle. Realized at the Higuchi Lab, University of Tokyo.

With an accelerating rotor, a viscous air-film is established under the glass disc. At speeds of some thousands rpm, this viscous boundary layer is on the same order of magnitude as the air-gap between glass rotor and electrodes, say 100µm. This active air-bearing, together with the stabilizing effect of the gyroscopic momentum eliminated almost all axial run-outs that were due to the use of ball bearings. The measured run-outs were under 1µm, same order of magnitude as the roughness of the glass disc.

Note that the presented solution, being very attractive for hard disc drive purposes (simple, precise, cheap), is not suitable for precise positioning, since the proposed air bearing is of an active nature, hence it needs important rotation speeds for its operation.

5.1.5 22 mm single side with single point bearing

For this prototype, as in the previously presented device (the 65mm diameter motor with single point bearing), the same remarks apply.
The motivation was to realize a very compact, very cheap and yet very efficient one-inch disc drive. This fast rotating device was intended to demonstrate the advantages of the electrostatic glass motor for data storage purposes. Figure 5.5 shows the realized prototype:

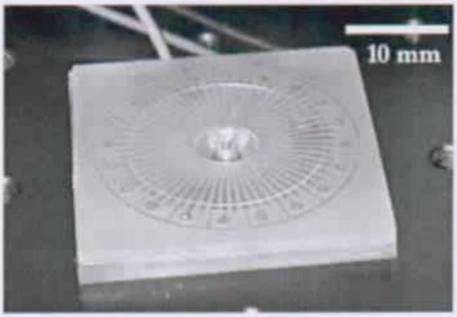

Fig. 5.5 22 mm motor, single side drive, with single point bearing. Electrode with n = 90, d = 400 um.

Figure 5.6 plots the start-up, shows the stabilization of the disc with time (and speed, since the disc continues to accelerate), and the axial run-out at 3000 rpm:

Fig. 5.6 Start-up sequence and axial run-out of the 22 mm disc drive

5.2 Prototype for precise positioning

5.2.1 Concept

The aim is a cost-effective, compact device that can operate from any commercially available PC without any upgrades, such as acquisition cards, DSPs, etc. The RS 232 serial port is a peripheral interface that all computers are equipped with; we chose to communicate with our device via this port. It seemed further necessary to develop the entire driver electronics from scratch, since the high voltage drivers needed do not exist on the market (since there are no comparable actuators on the market). The electronics could be composed out of off-the-shelf laboratory equipment, but would have the size of a full-scale mobile lab rack. This is due to the fact that most devices have too much power for our motors or too many additional features. So a compact driver with just the needed performances was developed. This circuitry drives the first operational prototype, a rotary glass motor mounted on a air bearing in order to eliminate any friction. Figure 5.7 shows the complete system.

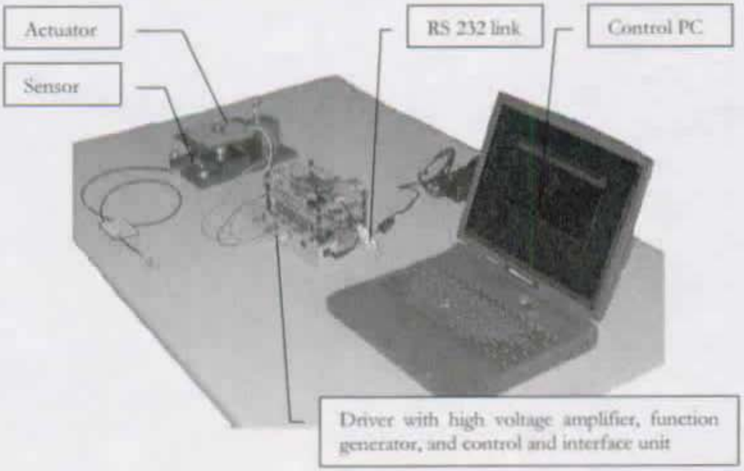

Fig. 5.7 Photo of the rotary positioning prototype

Figure 5.8 shows a schematic overview of the prototype:

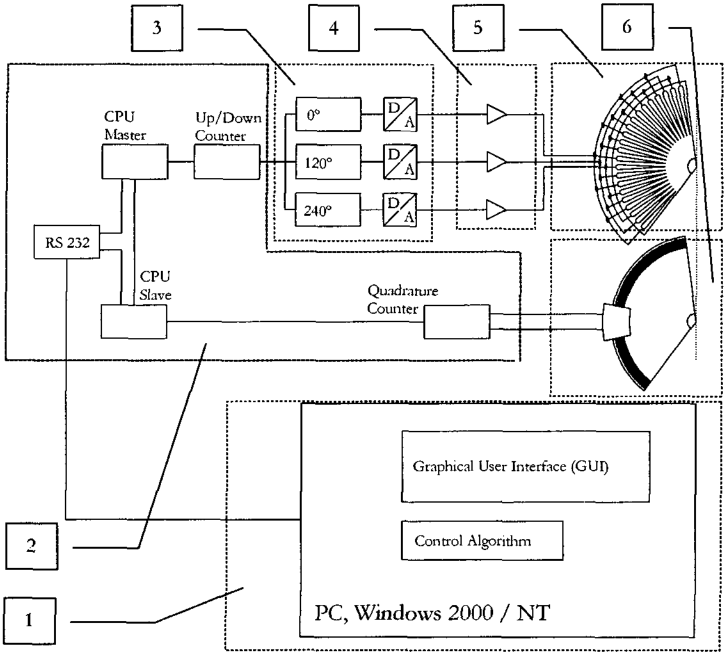

Fig. 5.8 Schema of the prototype

A Windows-based PC **1** features a graphical user interface that allows the operation of the positioning actuator. Different modi (Continuous rotation, incremental displacements, positioning) can be chosen. The PC is also hosting the control algorithm for closed loop positioning. The PC communicates via RS 232 with the interface and processor unit **2**, triggering the function generator **3** in the desired direction, with the desired speed and total displacement (user defined). The driver voltage is amplified by a three-channel high voltage amplifier **4** which drives the electrostatic glass motor **5**. The feedback loop is closed via an incremental sensor **6**, communicating the absolute position via the slave CPU to the PC.

5.2.2 Actuator and Sensor

Figure 5.9 shows the realized rotary positioner:

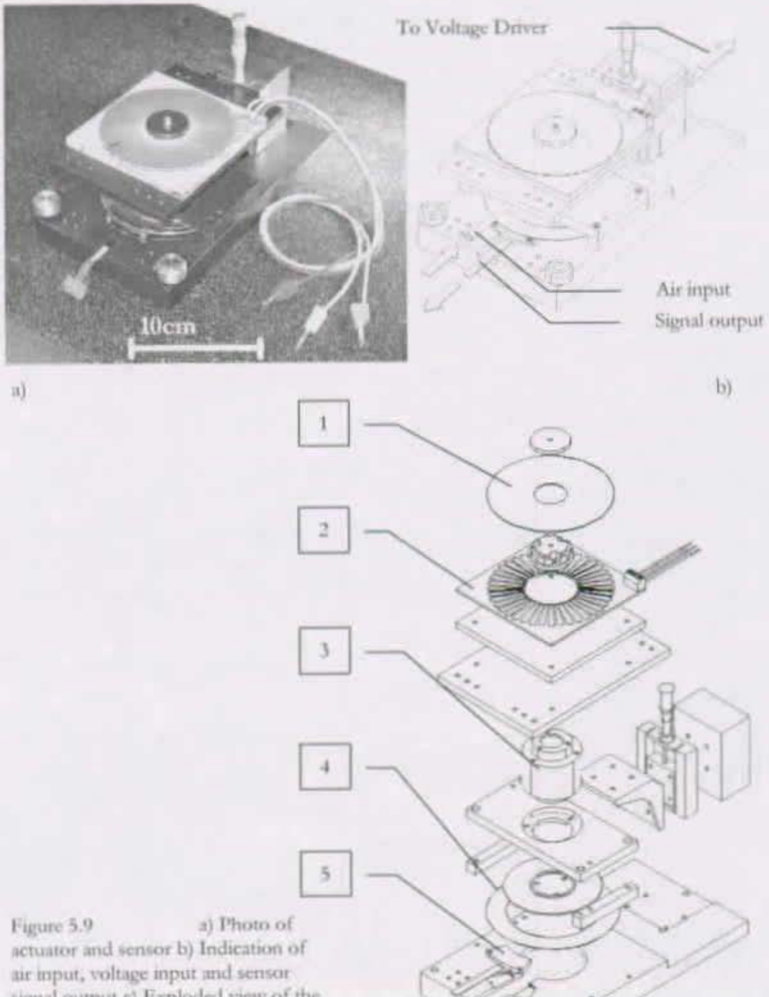

Figure 5.9 a) Photo of actuator and sensor b) Indication of air input, voltage input and sensor signal output c) Exploded view of the experimental setup

A glass disc **1** with diameter 95mm is mounted above a circular electrode array **2**, at a constant air-gap of 100μm. A static air bearing **3**, blocking all degrees of freedom except the rotation around its main axis, guarantees frictionless suspension.

The exact rotor position is determined using an incremental sensor disc **4** (Numerik Jena, 18'000 incr./rotation, 200 times interpolated → 0.35 arc-second resolution). The read out is performed with a very compact sensor head **5**. The outputs of the sensor are two signals in quadrature.

The implemented electrostatic glass motor features the following parameters (table 5.1)

Designation	Designation	Value	Unit	Reference
# tracks	n	240	-	(3.19)
# poles	m	80	-	(3.23)
Outer diameter	R_{out}	$9.5 \cdot 10^{-2}$	[m]	Fig. 3.8
Min. track width	w_{in}	$200 \cdot 10^{-6}$	[m]	Fig. 3.8
Inter-track gap	d	$400 \cdot 10^{-6}$	[m]	Fig. 3.8
Air-gap	g	$150 \cdot 10^{-6}$	[m]	Fig. 3.8
Voltage	V	900	[V]	Fig. 1.17
Sine resolution	n	16	[bit]	(2.20)
Rotor blend	TS-10 ceramic	-	-	-
Peak torque	T	1.4	[mNm]	(3.29)
Resolution	ζ	0.2	[arcsec]	(2.24)
Inertia	I	250	[gcm^2]	-

Table. 5.1 Characteristics of implemented electrostatic glass motor

5.2.3 Driver Specifications

The desired output of the driver electronics are explained using the output characteristics of a first prototype (figure 5.10):

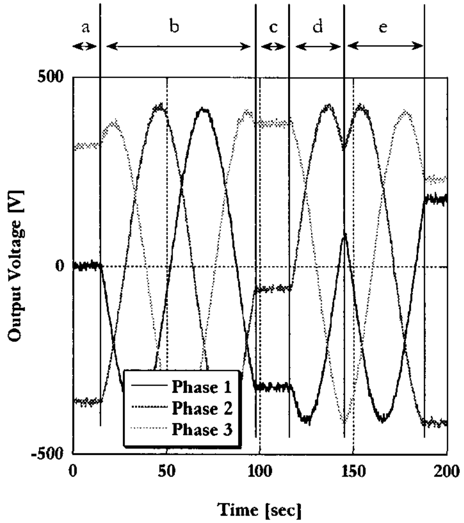

Fig. 5.10 Desired driver output characteristics, with indication of the different regimes: a) charging, b) forward rotation, c) stop, d) forward rotation and e) backward rotation

Prior to operation, the glass rotor has to be charged for several seconds (a), then the actuator is at stand-by and can be operated at any moment. A forward movement (clockwise or counterclockwise) is user-defined by displacement speed, displacement sense and displacement-amplitude (b). Once the desired position is achieved, the sine excitations are 'frozen' into DC voltages (c), in order to keep the rotor polarized, even at rest. The motor can be re-launched at any moment (d). In addition, it should be possible to change the rotation direction at any moment (e).

The sine wave excitations should be encoded with the maximal possible resolution (equation 2.20).

5.2.4 High Voltage Amplifier

Commercially available high voltage amplifiers are mostly one-channel devices and quite expensive. Bipolar amplifiers (the voltage swings around ground) are not available with voltages around ± 450V. The only commercially available bipolar high voltage amplifiers, are mainly DC devices with a bandwidth of 1kHz, having only one channel and costing around 10'000 $. This market situation imposed a custom development for a compact and cost-effective bipolar high voltage / low current AC amplifier.

The main features of the realized high voltage amplifier are:

- 3 Channels
- Input ± 10 V, Output ± 450V
- 5 Watt output power
- 10 kHz bandwidth
- Convenient 230VAC/110 VAC power supply

5.2.5 Function generator

A high-resolution function generator had to be developed for several reasons. First, commercial generators are expensive, of lower resolution (8 or 12 bit), have at maximum 2 channels and cannot 'move backward' with the output sine waves, a feature indispensable for precise positioning. Software solutions (LabView®, LabWindow® etc.) were evaluated, but are not an option since they do not allow smooth acceleration of the sine wave excitations or changing of the direction of the moving field. Their inherent jumps in the generated sine waves cause the rotor to lose the motor field and can generate electric breakdown between motor electrodes.

The main features of the realized high-resolution sine wave generator are:

- 3 Channels
- Input: digital counter input 16 bit (parallel), clock for analog conversion

- Output: 3 sine waves, 65536 levels of amplitude, 65536 points per period
- Count up/Count down capability
- Output frequency: DC to 436 Hz

The realized function generator allows, in combination with the implemented 80 pole electrode of the presented rotary prototype in figure 5.9, a maximal rotation speed of 290 rpm (theoretical value, not considering the important inertia of the air bearing). For a 80-pole electrode, we obtain a theoretical resolution of 0.2 arc-second, of course over an infinite range (rotation). On a linear system with a comparable electrode (same inter-track gap *d*, track width *w* of same size), the theoretical resolution would be 18 nm.

5.2.6 Interface and processor unit

In order to use the convenient RS 232 connection that all PCs come equipped with and to limit the computation on the host PC, a processor unit that commands the function generator and the high voltage amplifier stage is necessary. We chose two PIC16F76 CPUs, programmed in assembler-code for maximal processor speed. One CPU (master) manages the serial communication with the host computer and controls the number of displacement steps, the motor speed and the direction of rotation; the other CPU (slave) manages the sensor readout and communicates the exact position of the rotor to the host PC via RS 232 on user request.

Appropriate circuitry ensures that the control board is always counting the impulses coming from the incremental sensor, independent from the tasks performed by the master CPU.

The main features of the realized interface and processor unit are:

- RS 232 serial connection with commercial PC
- No need for data acquisition card on PC, just installed software
- Two 20 MHz PIC16F76 processors in master/slave mode
- Parallel in / parallel out 16 bit counter

The data stream through the relatively slow RS 232 line could be minimized to a three-byte word.

The first byte codes the displacement speed (256 different levels), the second byte indicates the number of desired displacement steps (0 to 255) and the third is used to define the rotation direction of the rotor and if the sensor output should be communicated to the host PC or not. The processor unit acknowledges all actions.

Figure 5.11 shows the first and the second driver prototype:

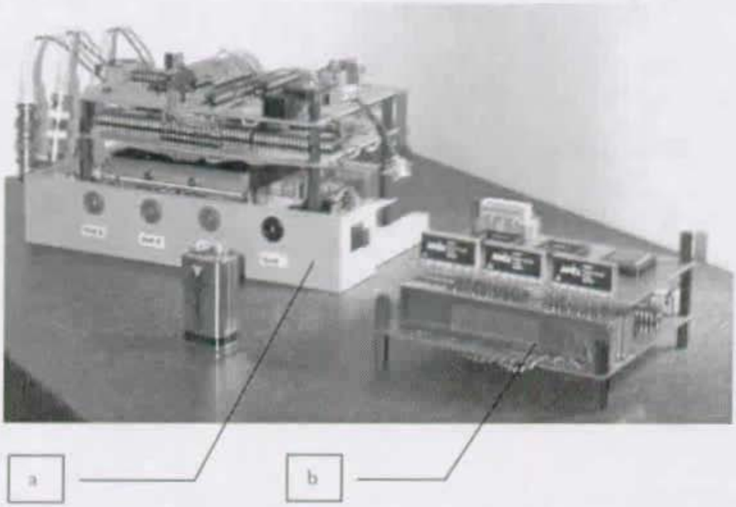

Fig. 5.11 a) First driver prototype, manually soldered, b) Second driver prototype, using SMD components. 9V battery for size indication.

The manually soldered first prototype (figure 5.11a) features 16bit technology, but due to inevitable unprecisions (ground loops, long cables, common analog and digital ground etc.), only 14 bit could be exploited.

The second prototype (figure 5.11b), based on the experience gained with the previous one, allows full 16bit operation.

5.2.7 Graphical User Interface

Positioning actuators are usually used in combination with data acquisition systems that acquire and analyze data issued from the displaced object or from a related process. Thus, it is desirable to have a relatively compact command window, without "popping-up" sub-windows that cover the other information on the screen. Figure 5.12 shows the implemented graphical user interface:

Fig. 5.12 Windows-based graphical user interface with functional sub-panel

The graphical user interface window **1** is of standard size. It hosts the functional sub-panel **2** that allows the operation of the electrostatic glass positioner in its different modi. Additional control buttons **3** allow stable launch and stopping of the program at any time.

Five functional sub-panels exist. One for each modus, e.g. continuous displacement or rotation (tunable parameters are sense, speed and smoothness), stepwise displacement (step size and displacement speed), Feed-backed position mode using the incremental sensor to ensure accurate positioning (the desired position can be manually introduced) and two for the choice of the modus and the introduction of the rotor parameters. The developed driver is apt to drive rotary as well as linear devices.

The development of complete positioning driver software is not within the scope of the present thesis, but using the developed modules (continuous movement, step movement, controlled position control), more sophisticated movement patterns can be easily implemented.
Figure 5.13 presents the various functional sub-panels:

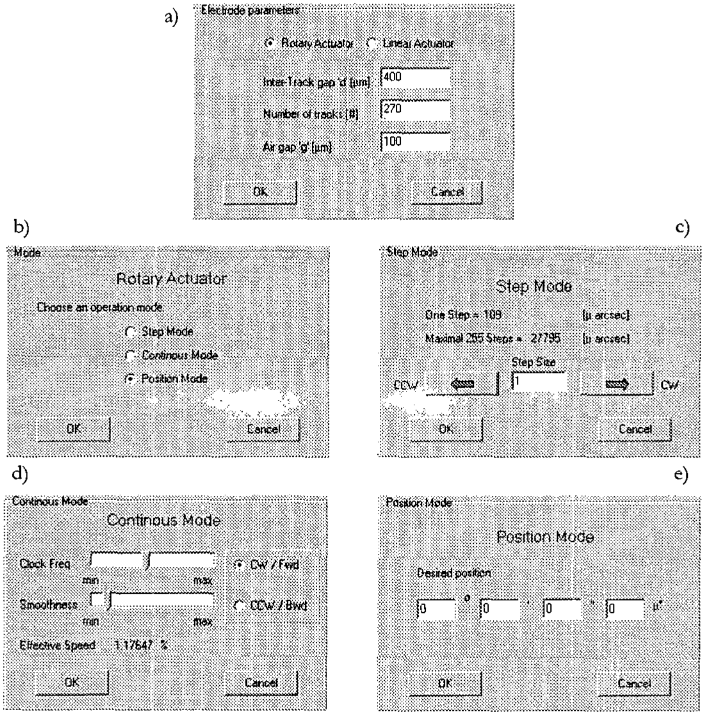
Electrode parameters
● Rotary Actuator ○ Linear Actuator
Inter-Track gap 'd' [µm] 400
Number of tracks [#] 270
Air gap 'g' [µm] 100

Mode
Rotary Actuator
Choose an operation mode
○ Step Mode
○ Continous Mode
● Position Mode

Step Mode
Step Mode
One Step = 109 [µ arcsec]
Maximal 255 Steps = 27795 [µ arcsec]
Step Size 1

Continous Mode
Continous Mode
Clock Freq
Smoothness
● CW / Fwd
○ CCW / Bwd
Effective Speed 1.17647 %

Position Mode
Position Mode
Desired position
0 ° 0 ' 0 " 0 µ"

Fig. 5.13 Functional sub-panels of the graphical user interface. a) Actuator type choice and adapted introduction of electrode parameters, b) choice of operation modus, c) step mode panel with indication step size, d) continuous mode panel with indication of effective displacement speed, e) position mode.

The various panels are self-explanatory. The indication of the 'effective speed' in the continuous mode panel is due to the fact that for a constant clock frequency, the displacement speed of the rotor varies greatly with the displacement-step size.

VI. Results

6.1 Smoothness

The charge dynamics described in equation (3.21) and measured in figure 4.5 suggest that the glass-charge distributions are still subject to changes once the motor starts to turn. Indeed, the electrostatic field seen by the glass rotor differs fundamentally between the DC charging mode and the motor mode. This is due to the fact that a sinusoidal electrostatic field is not realizable at rest (non-moving sinusoidal field), but can be achieved in motion (moving sinusoidal field) by means of multiple-phase electrodes, as proposed for the electrostatic glass motor. These multi-phase electrodes should have equal track-width *w* and inter-track gap *d*. However, the motor needs a DC period in order to build up charges that can power the rotor. During this charge build-up period ("charging"), the field is somewhat discontinuous, as sketched in figure 6.1:

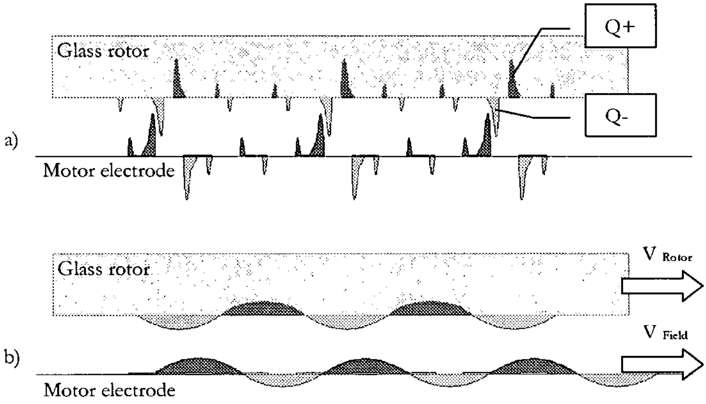

Fig. 6.1 Schematized charge distribution during a) charging mode b) motor mode. Amplitude and sign of charge distributions are indicated by color (dark gray = positive charges, light gray = negative charges) around the glass and electrode surface line.

When the electrostatic field starts to move, an observer on the glass rotor would see a sinusoidal moving field. The charges are expected to mirror the shape of the applied field, changing with the same time constant that was determined in figure 4.6. Driven by a sinusoidal field, the rotor is expected to adapt a sinusoidal charge arrangement, thus losing its speed-ripple within a couple of seconds and adopting a smooth synchronous movement.

Figure 6.2 shows the experimental verification of the theory:

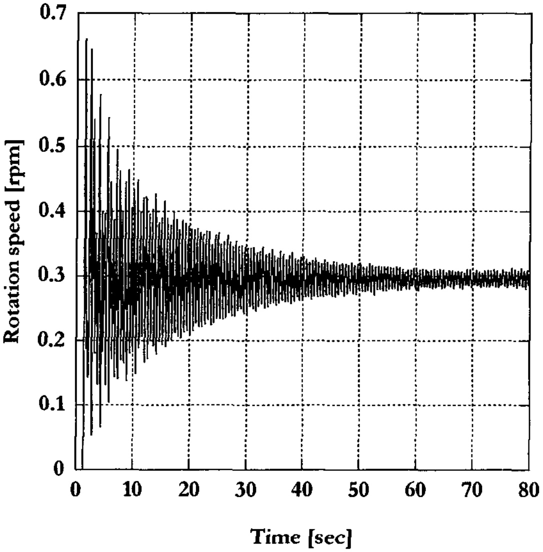

Fig. 6.2 Progressive smoothness of rotation during start-up of the electrostatic glass motor.

The experiment consisted of imposing a rotation speed of 0.3 rpm at time *t*=0. It was observed that, effectively, the cogging is reduced with time, following an exponential envelope with a time constant comparable to the charge dynamics of glass determined in figure 4.6.

This measurement was performed using the information from the incremental sensor (figure 5.9). The frequency of the impulsions (900'000 impulsions / 360°) is equivalent to the rotation speed and allows long time / long range measurements. Figure 6.2 proves that with time, the rotation is without any speed ripple.

This behavior of the electrostatic glass motor is unmatched by other electrostatic or electromagnetic actuators. The magnetic or electrostatic potentials on the rotor usually have a discontinuous distribution in the form of permanent magnets or electret charge stripes. Also in the case of reluctant electromagnetic or variable capacitance electrostatic actuators, the variation of the reluctance / capacitance is discontinuous, resulting in speed ripple. Of course, by means of position feedback, relatively smooth rotation can be achieved.

Another long-range measurement supports the assumption that the movement is truly smooth, i.e. without speed ripple: The gap between two adjacent electrode tracks *d* being 400μm for the motor electrode; we should observe a speed variation with a period in the order of the gap *d*, if there is any motor-related speed ripple. Figure 6.3 shows a measurement that gives no indication of a speed ripple related to the motor principle:

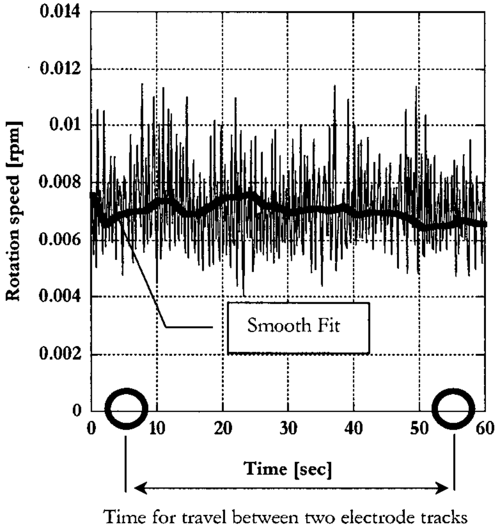

Fig. 6.3 Progressive smoothness of rotation during start-up of the electrostatic glass motor.

A relatively slow rotation speed (0.0075 rpm) is imposed on the rotor. Measuring the frequency of the sensor-impulses (e.g. the rotor speed), no periodicity synchronous to the stator can be determined. The noise observable in figure 6.3 is attributable to the measuring method (small vibrations of sensor increments around the equilibrium). Smooth fits do not indicate any periodicity that can be associated with the electrode geometry, so a perfectly smooth movement down to sensor resolution can be assumed.

A short-range measurement, performed with a capacitive probe, is presented in figure 6.4. Again, over a range of 33 arc seconds, no speed ripple was observed:

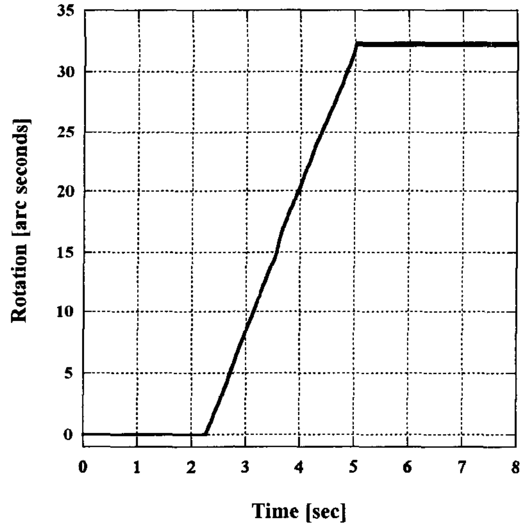

Fig.6.4 Smooth rotation of the rotor, powered by a 10 arc sec/sec moving electrostatic field.

This open loop rotation smoothness, together with a very broad speed range from 30 rpm down to 0,1 arc-second / second (for the positioning prototype presented in figure 5.9) are the main features of electrostatic glass motors, unmatched by electromagnetic or piezoelectric alternatives.

6.2 Open loop step mode positioning

One of the main advantages of the electrostatic glass motor is, besides its smooth displacement and its broad speed range, that its open loop precision is completely decoupled from mechanical aspects.
The resolution is a function of the patterns' geometric dimensions, as well as of the function generators' resolution. Exclusive of the geometric outline of the motor electrode, which we suppose to be ideal thanks to printed circuit board technology, the resolution of the function generator plays a decisive role. It will be shown that a 16bit resolution is already permitting a sub-arc second positioning. Note that in audio technology, 24bit resolution has been mastered.

Using the developed 16bit function generator, the influence of the bit-resolution can be simulated: Modifying the step size via the graphical user interface, the device behaves like a function generator with a resolution down to 8 bits. Table 6.1 shows the conversion:

Resolution	Step Size
8 bit	256
10 bit	64
12 bit	16
14 bit	4
16 bit	1

Table.6.1 Simulation of lower-resolution function generators using a 16bit device

The implemented rotary incremental sensor allows the measurement of displacement steps as small as 16 (corresponding to a 12 bit resolution as seen in table 6.1). The displacement step sizes for 8bit, 10bit and 12bit resolutions are compared in figure 6.5. The obtainable displacement resolutions using generator resolutions ranging from 8bit to 12bit allow the experimental estimation of the displacement resolution using the full 16bit capabilities. This estimation is visualized in figure 6.6. Figure 6.6 also shows the accordance of the model (equation (2.24)) with reality.
The measured displacement step resolutions range from 80 arc seconds for an 8bit function generator down to 5 arc seconds for a 12bit generator. The estimated resolution of a 16bit generator is approximately 0.3 arc seconds.

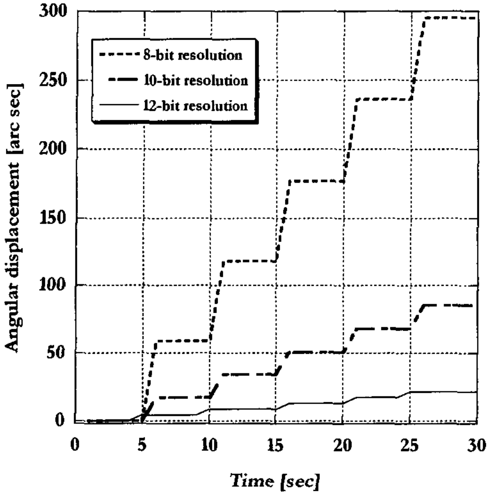

Fig.6.5 Open loop step displacement for 8bit, 10bit and 12bit function generator resolution.

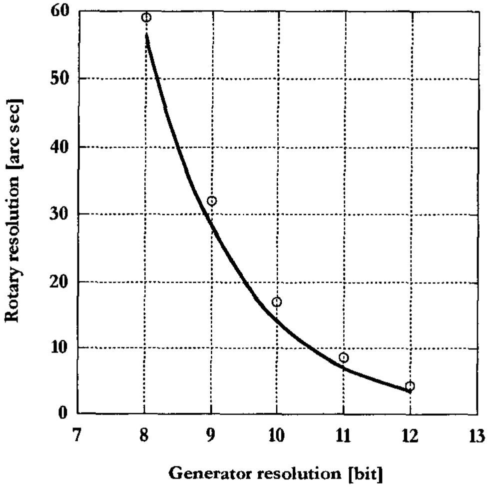

Fig.6.6 Rotary displacement resolution versus function generator resolution. Comparison between model and measurement.

The measurements were performed by counting the increments issued from the rotary encoder. Good agreement of model and measurement allow the following performance estimation (table 6.2):

Generator Resolution		**Rotary displacement**		**Linear displacement**	
14	[bit]	0.8790	[arc sec]	73.5	[nm]
16	[bit]	0.2192	[arc sec]	18.3	[nm]
18	[bit]	0.0554	[arc sec]	4.62	[nm]
20	[bit]	0.0181	[arc sec]	1.15	[nm]
22	[bit]	0.0032	[arc sec]	0.29	[nm]
24	[bit]	0.0008	[arc sec]	0.07	[nm]

Table 6.2 Theoretical displacement resolutions for comparable rotary and linear electrostatic glass actuators. Rotary actuator: m = 90, d = 400μm. Linear actuator: w = 400 μm, d = 400 μm. Parameters according to figures 2.12 and 3.8).

Since angular displacements are not as intuitive as linear displacements, the rotary actuator is compared to a linear actuator of similar characteristics.

The rotary resolution of a 14bit driver was verified using a laser displacement probe (figure 6.7):

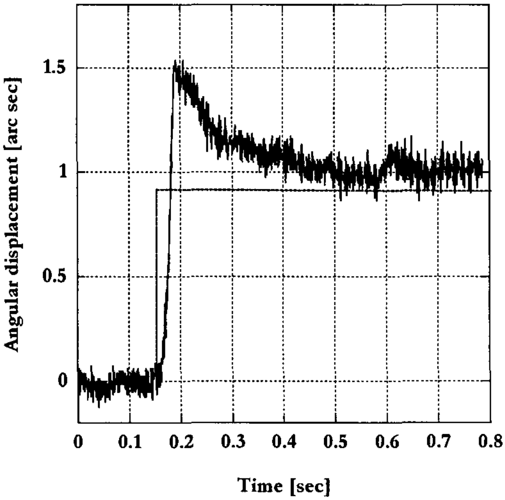

Fig. 6.7 Measurement of displacement step controlled by 14bit driver. The dashed line indicates the computed displacement step.

The resolutions theoretically possible with driver resolutions above 20bits, as presented in table 6.2, are given for the sake of completion. For comparison, the atomic radius of the H atom is 0.03 nm, the Al atom 0.143 nm and the Cs atom 0.262 nm. It can be concluded that the resolution of the driver does not constitute a technological limit (as mentioned previously, audio devices already work with 24bit signal resolution).

Expressions (2.20) and (2.24) indicate a direct relation between geometrical outline of the electrodes and the displacement resolution. It is tempting to diminish the electrode track width w and the inter-track gap d, in order to augment the resolution. Two comments apply:

The track width w can be reduced. However, depending on the employed electrode-manufacturing technology, a certain minimal width should be respected. For standard printed-circuit-board etching technology, this minimum is around 100µm. Thin electrode tracks enhance sparking due to the edge effect [30].

The inter-track gap d cannot be reduced at will. The validated hypothesis (flux follows circle trajectory) that led to equation (3.29) indicates that the gap d should be around two times the air-gap g (between glass rotor and motor electrode). A d too small with respect to g leads to flux closing underneath the glass rotor (little or no flux goes through the glass), drastically diminishing the obtainable force / torque. Since the easily realizable air-gap g is considered to be around 100µm, the minimal inter-track gap d is put between 200 and 300µm. It was experimentally verified that no usable force can be obtained with d = 100µm, validating the hypothesis that the flux describes a circular trajectory. Of course, a reduced torque / force, due to a small gap d, is partly compensated by the surplus of tracks that now fit on the electrode (higher track density). If further torque augmentation is desired, "stacking" motor layers (as described in paragraph 3.1.2) is a valid solution. Stacking is in no way affecting the displacement resolution.

A very cost effective positioning device could therefore have the following characteristics:
The driver resolution is 16bit, a resolution that that is not too delicate to master. Also, 16bit digital-to-analog converters are significantly cheaper than 24, 22 or even 18 bit devices.

The distance between rotor and stator, the air-gap *g*, is kept at 100μm for the reasons presented above.
The performance of a rotary device is linked to its radius. For a 10cm diameter glass rotor, 450 electrode tracks with a mutual spacing of 300μm seem realizable. The calculated resolution is 0.13 arc seconds.
Using a linear device with the estimated minimal electrode track width *w* of 100μm and inter track gap *d* of 300μm, the resolution would be about 9 nm.

Using a laser displacement probe, the capability of the driver in open loop step mode could be verified. Imposing a fast displacement, followed by various direction-changes at lower speeds it can be observed that the device works smoothly as expected without any hysteresis and without backlash. Figure 6.8 plots the measurement:

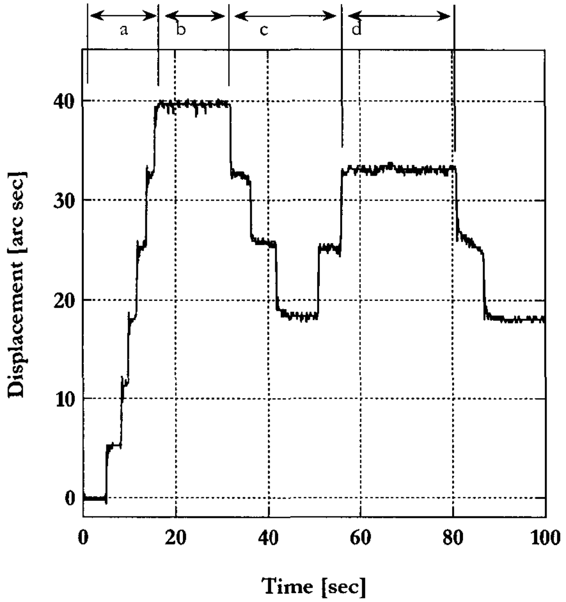

Fig. 6.8 Measurement of forward and backward rotation at different speeds. a) rapid b) steady c) direction change d) steady. Displacement steps of 5 arc seconds.

6.3 Closed loop positioning

6.3.1 Self-sensing

The electrostatic glass motor is potentially capable of position-self-sensing. This tempting and elegant solution is presented in figure 6.9:

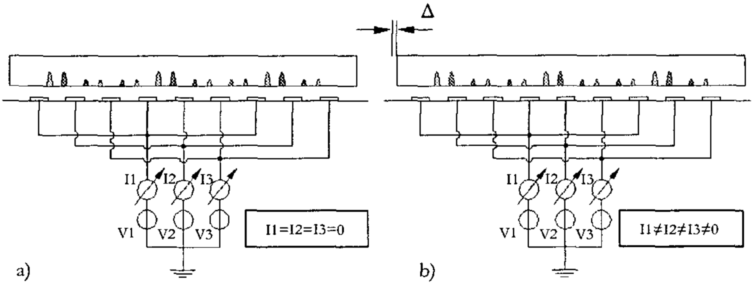

Fig. 6.9 Self-sensing. a) Rotor at rest, in equilibrium with stator field, b) observed current variation due to rotor displacement.

The three applied potentials issued from a (supposed ideal) voltage source keep the rotor in equilibrium with its stator field. The capacitance of the system remains constant, thus no current flows to and from the electrode tracks. Once the rotor is displaced by a distance Δ (by means of an external force / torque), each electrode track sees itself opposed to a higher of lower net charge (on the glass). The adaptation to this new charge situation manifests itself in current flowing to or from the electrode tracks. These currents stop once the charge distribution on the electrode tracks mirror the charge distribution on the glass rotor. Thus the displacement could be sensed without external sensor, by observation of the charge dynamics:

$$\Delta \propto \int I_i dt \qquad i = 1, 2, 3 \qquad (6.1)$$

But as the charges creep slowly through the glass (visco-elastic strain effect), there is no reference to the glass rotor. Once the rotor is displaced (figure 6.9a), the charges will 'wander' towards their old position with the usual long time constant. Hence an absolute reference would be lost; an external sensor has to be implemented.

6.3.2 Control circuit

If the rotation speed is fast with respect to the charge time constant (this is the case for all propulsion speeds, except really slow ones), the described visco-elastic effect can be neglected. However, if a precise position has to be maintained over time and there are load forces and torques acting on the actuator, the positioning actuator has to be controlled. A possible feedback loop is sketched in figure 6.10:

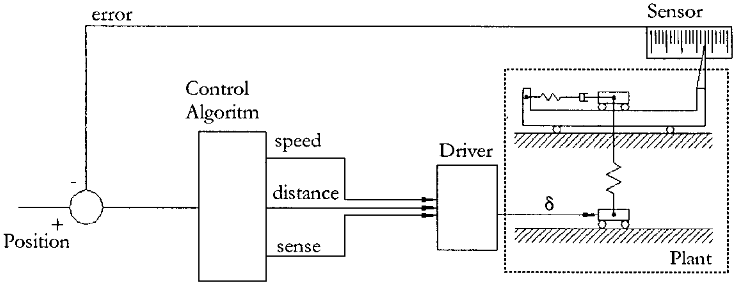

Fig. 6.10 Control circuit for electrostatic glass actuator

The transfer function of the plant is given by equations (3.41) and (3.42) for the linear and the rotary actuator, respectively.

The proposed control circuit was implemented, using a PD controller. The displacement speed of the stator field corresponds to the derivative component. Error-rejection comportment within the resolution of the sensor was observed.

The displacement speed indicates the torque as with many electrical machines and therefore stands for the proportional component, the gain. The displacement sense of the stator field opposes the rotor displacement sense.

More advanced control algorithms could be implemented. The control engineer community proposes a vast choice of solutions for the stabilization of inherently stable plants like the electrostatic glass motor; a stable and robust position control is possible and mastered.

The goal was to characterize the "plant", in order to allow control engineers to apply the correct tools for a precise positioning according to the required specifications.

6.4 Other aspects

6.4.1 Losses

The main losses in electrostatic glass motors are due to the capacitive losses in the stator (the capacitances created between the metallic electrode tracks and the dielectric substrate).
The capacitive losses between rotor and stator are neglectable since the rotor follows synchronously the stator field (so no re-polarization in the dielectric occurs).
The Joule-losses in the stator augment with the speed of the stator field:

$$P_{joule} = UI = \frac{U^2}{Z} = U^2 \omega C \tag{6.2}$$

In order to minimize the capacitive losses, the substrate of the electrodes has to be chosen with care (low relative permittivity).

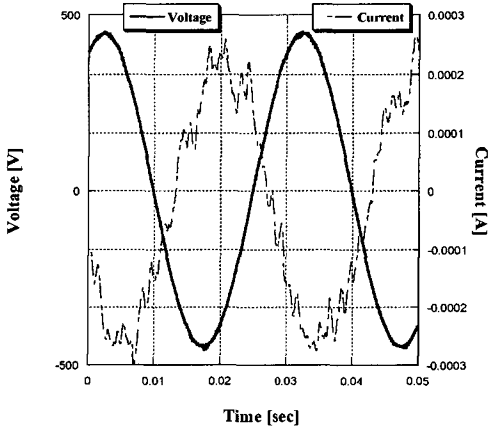

Fig. 6.11 Measured input voltage and current for a 65mm glass disc drive @ 3000 rpm for one phase. Electrode parameters: d = 400μm, g = 100μm, m = 60,. RH = 30%

In order to get an order of magnitude, the input voltage and input current for a 65mm diameter motor at 3000 rpm have been measured (figure 6.11). One phase was measured, which gives for all three phases a total average power consumption of about 0.2 Watt. Note the for a capacitive system typical phase shift of 90 degrees.

It can be concluded that the electrostatic glass motor is a low-power device per se, whereas the main losses of the overall positioning system are located in the driver electronics (generation of high voltages etc.)

6.4.2 Excitation strategy

Using three phase voltages, there are three different strategies to drive the rotor. First, only one electrode can be used. Second, using two motor electrodes, with the upper and the lower moving electrostatic field in phase and third, with the two fields out of phase by 120°. The prototype of figure 5.2 was operated in the three ways and the maximal obtainable speed was measured. This top speed, being function of the torque, gives an indication about the optimal excitation strategy. Figure 6.12 plots the rotation speed versus the zero-to-peak voltage $V_{0\text{-}Peak}$:

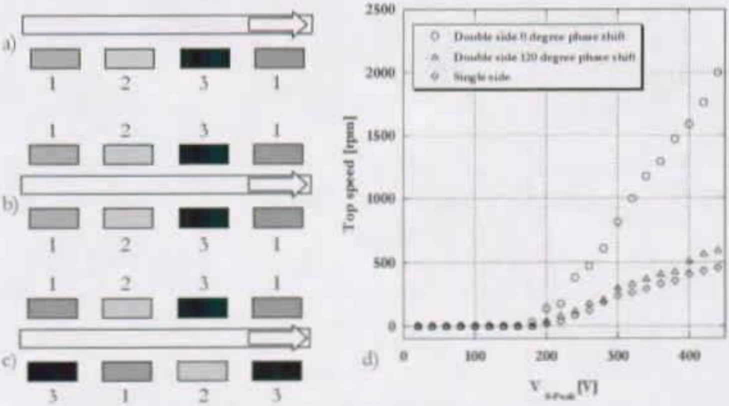

Fig. 6.12 Determination of the optimal excitation strategy. a) Schematic principle of single side, b) double side drive with 0° phase shift, c) double side drive with 120° phase shift, d) comparison between the three excitation strategies. The arrows indicate the displacement sense.

It can be observed that if the upper and the lower field are in phase, the maximum top speed is about three times higher than with only one electrode.

Note the poor performance of the 120° phase shift setup, due to crosstalk between upper and lower electrodes (the air-gap *g* is of the same order than the inter-electrode gap *d*).

This situation is simulated by finite elements simulation in figure 6.13:

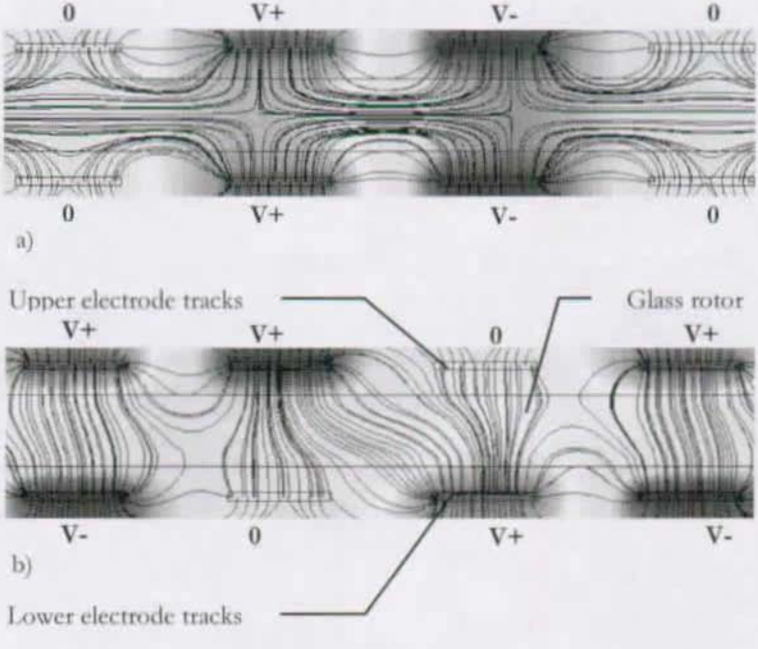

Fig. 6.13 a) Upper and lower in phase b) Out of phase by 120°

It can be seen that, if the upper and lower electrodes are out of phase, the flux lines close between the two electrode layers via the glass disc. The resulting field distribution is not optimal for motor applications: The induced charge distributions are not in the vicinity of the inter-electrode gap, resulting in a lower torque.

It can be concluded that the optimal excitation strategy is the "sandwich"-structure using two electrodes, but care has to be taken that the upper and lower field are in phase.

6.4.3 High voltage in desktop devices

It is important to note that high voltages, we talk of voltages above one kilovolt, are already common in today's everyday electronic appliances. The most common applications are drivers for liquid crystal display backlights (LCD). The usual voltages for those applications are above 2 kV and the power supplies can easily offer more than 10 Watts. Coil wound transformers or compact piezo-transformers are available. Figure 6.14 shows a of-the-shelf high voltage power supply using a piezo-transformer (from the Japanese enterprise TOKIN):

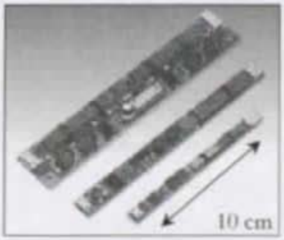

Fig. 6.14 Tokin PIT, > 2000 V power supplies for LCD displays

The high voltage part of an electrostatic glass actuator is not accessible by the user (covered by a good insulator, the glass rotor), so the only way to touch a live electrode is to disassemble the device with the power supply switched on. The electrodes are just a fraction of a millimetre apart, so it is quasi impossible to touch only one polarity. If somebody really opens the apparatus with the high voltage supply turned on, removes the disc and touches the electrode (presumably with a finger), the small current would only flow for a fraction of a millimetre through the human body (the distance along the flux lines between two electrodes) without passing any vital organs. The tiny shock, comparable to a cattle fence, will teach not to open switched on electronic appliances.

VII. Conclusion and outlook

A new concept for precise rotary and linear positioning has been proposed in this thesis.

Using a seldom-used electrical property of glasses, the relatively stable charge distributions induced by an applied electrostatic field, very smooth synchronous rotation over a wide speed range was proved to be possible. This rotation can be stopped at any time with very high precision, allowing precise rotary positioning with a theoretically infinite open loop resolution.

The smoothness of the rotation was found to be due to the rather slow dynamics of the induced charges, the same phenomenon that allows the induction of surface charges that actually make the actuator work. Since the charges on the rotor have the tendency to mirror the applied stator-field, the adaptation is completed after a characteristic time constant in the order of tens of seconds; an applied sinusoidal stator field will create a sinusoidal rotor field, allowing a smooth movement.

The open-loop resolution was found to be dependent only on the geometric outline of the motor electrode realized with printed circuit technology, and the resolution of the driver circuitry.

The smooth movement over a very broad speed range (fast for transportation, slow for approaching the desired position; depending on the motors' dimensions and on the inertia of the bearing) the high open loop resolution, absence of wear, its unlimited operation range together with the actuators' remarkably simple structure (potentially very low production cost even at small series) and compact outline is a combination of properties unmatched by other technologies.

The proposed concept of positioning produces weak forces that require low rotor inertia. However, promising applications are found in the in-line positioning of optical devices, laser machining or electron-beam operations. The weak forces are a drawback that can be improved by stacking multiple glass-electrode pairs, stacking which does not affect the positioning resolution.

A review of the state of the art in rotary precise positioning showed clearly that there is a niche for highly compact, cost effective devices with sub-arc second resolution and an infinite operation range. The usual application of the commercially available devices, the positioning of optical elements, is encouraging for an electrostatic device, since the relatively weak forces and torques are not influenced by external loads. A compact actuator that can operate open loop, e.g. without expensive high-precision sensors, would be useful for various applications.

After an introduction to electrostatic actuators in general, the physical principles that "power" the electrostatic glass motor have been analyzed. The behavior of a non-ideal dielectric in an electric field has been studied. The glasses have the most pronounced polarization, and are therefore presented as the material of choice for this kind of actuator. It actually works also with other dielectrics such as certain polymers, but the performances seem to be much weaker. Linear as well as rotary actuators have been introduced, parameterized and the theoretical expression of the open–loop resolution in function of the electronic resolution and the geometry of the electrode pattern has been established.

An analytical model of the driving forces has been established. It is based on two hypotheses:

- that the motor flux lines describe circle trajectories (verified by finite element simulation)
- that the air-gap between rotor and stator is of the same order of magnitude than the distance between two electrode tracks

This model describes the rise and decay of glass-charges with time, as well as their interaction with a moving stator field, and leads to the exploitable lateral forces (for linear actuators) and torques (for the rotary case). An attempt to approach these relatively heavy expressions using function-discussion methods proved successful and provided relatively compact expressions, which constitute the first design rules for electrostatic glass actuators.

In order to evaluate the model, a high-resolution force sensor has been developed. It allows the measure of the weak electrostatic forces. The demanding specifications (measure at constant air gap, possibility to "scan" over a range of 1 mm and the possible use in different spatial configurations) led to a custom development, based on a flexible hinge structure, actuated by a magnetic bearing. This versatile sensor allowed the verification of the model and other, not modeled but important, characteristics of the electrostatic glass actuator such as its dependency from humidity. The optimal electrode pattern was determined. As predicted by the model, contrary to electrostatic attraction of conductors (for example copper), comb shaped electrodes of alternate polarity featuring a maximum of boundaries (a high electrode track density) proved to develop the highest forces for the attraction of dielectrics (for example glass). For the attraction of conductors, a plain electrode surface is optimal.

The optimal glass composition was determined among a set of the most common glass families. It was shown that the cheap and widely used soda-lime blend has the best performances among the tested glasses. Luckily soda-lime glass can easily be machined and comes also in very thin lamellas (object covers for optical microscopes) of 0.1 mm thickness; therefore further miniaturization of electrostatic glass motors seems easily achievable. Experiments and mathematical model show that a glass rotor thickness above 0.5mm does not improve the performances. In addition, the strong influence of the air-gap between rotor and stator was documented, also in accordance with the analytical model. This air-gap should be inferior to 150µm. A parameter of utmost importance for electrostatic actuators, the humidity, also plays a key role for the glass actuator. It was shown that a maximum performance in function of humidity exists and that the actuator works well in the range of 10 to 70 % RH.

Prototypes of various sizes and designs have been operated. It was confirmed that the electrostatic forces are potent enough to spin (or convey) macroscopic glass rotors at technically interesting speeds. The enormous speed range that was observed using one-inch glass discs and light ball bearings (from over 5000 rpm down to 0.0001 rpm) led to the tempting idea to use this actuation concept for very compact, simple and cost-effective hard disc drives, an idea proposed by Higuchi at the University of Tokyo. The final prototype for precise rotary positioning is built around a compact static rotary air bearing, in order to prevent any friction.

This thesis treats both, linear and rotary actuators, but a rotary device is preferred because of the infinite motion range for research purposes. Sub arc-second resolution can easily be demonstrated without imposing any stringent manufacturing tolerances.

The requirements for the driving electronics were out of reach of commercially available components (16bit resolution, DC capabilities, the possibility to move forward and backward without loss of continuity, real time programming of frequency, rotation sense and displacement value etc.), so a compact custom high voltage driver with all the needed features was designed and realized. Controlled via a convenient graphical user interface over the RS232 port, it allows a cost-effective and compact command of electrostatic glass positioner with any Windows-based PC.

The realized prototype was characterized and proved to work satisfactorily. As predicted, the cogging of the rotation diminishes with time, so that after 30 seconds of operation no speed ripple was observable. The decrease of the speed ripple occurs with a time constant equal to the rise and decay time of the glass charges. The open loop positioning capabilities have been measured and an angular resolution of 0.3 arc-second was reported. The dependency between positioning resolution and driver resolution was measured and confirmed the model. Based on the measurements, it could be shown that by increasing the driver resolution from 16bit to 18bit (audio technology has already mastered 24bit) and by using a simple PCB-electrode, angular resolutions under 0.05 arc seconds can be obtained, a resolution unachieved by concurrent rotary positioning actuators (state of the art is 0.1 arc seconds, over a limited range of 8 degrees, using piezo-actuators). The resolution can be further increased by diminishing the geometrical parameters of the electrodes (within certain limits). An eventual loss of torque / force can be compensated by stacking of multiple electrode-glass layers. The driver proved to work very well, allowing step rotation, continuous rotation and feed-back position control. Feed-back position control is necessary for applications where a load torque or force is acting on the rotor, since the slow charge-creeping (responsible for the stable charge arrangements that make the electrostatic glass motor work) is inducing a visco-elastic strain effect into the actuator. In order to counter this charge creeping, an additional sensor was implemented, providing sub-arc second angular resolution. Using a PD controller, the angular position could be stabilized. It is also this creep that discards the tempting approach of self-sensing (As the actuator is the sensor, there is no need for expensive external sensors). The slow creeping of the charges and therefore of the rotor imposes an external sensor.

CONCLUSION AND OUTLOOK

The present thesis developed all necessary design tools for the development of rotary and linear electrostatic glass actuators. The forces, resolutions as well as control aspects and driver electronics have been examined. Based on this, future work should focus on two issues:

1. The realization of a multi degree of freedom displacement stage (x-y-θ is sufficient for many applications) [72] should be envisaged. The necessary torques and forces to drive the stage can be obtained by stacking multiple glass-electrode layers. The most challenging part in designing such a device is certainly the bearing issue: For the research presented in this thesis, powering just one rotary axis, a convenient static air spindle could be used. We made abstraction of the bearing by considering that it was ideal therefore friction was absent. It is desirable that no cables and certainly no rigid air-conducts lead to the positioning table (inducing forces, therefore errors). Already a single linear axis is not trivial, since linear air bearings always bring the air pressure to the slider, therefore connect the slider to an air-conduct. Active magnetic bearings appear to be the best alternative to linear ball or roller bearings. Electrostatic bearings or passive diamagnetic bearings are more compact, but have less load capability.

2. The control of such a stage. Although the actuator works very well open loop, this kind of operation should be reserved for applications where a constant and very smooth movement is required (e.g. scanning applications) or where mediocre precision is sufficient. For such applications, open loop operation presents a very well performing and cost effective solution. For most precise positioning applications, the well-known algorithms from the field of precision machinery tooling can be directly implemented to drive the multi-axis stage.

Finally, a first design of a potential 'product' electrostatic glass positioner can be presented. It is build around a Canon AB-30 air spindle. Figure 7.1 gives an idea about size and structure of such a device:

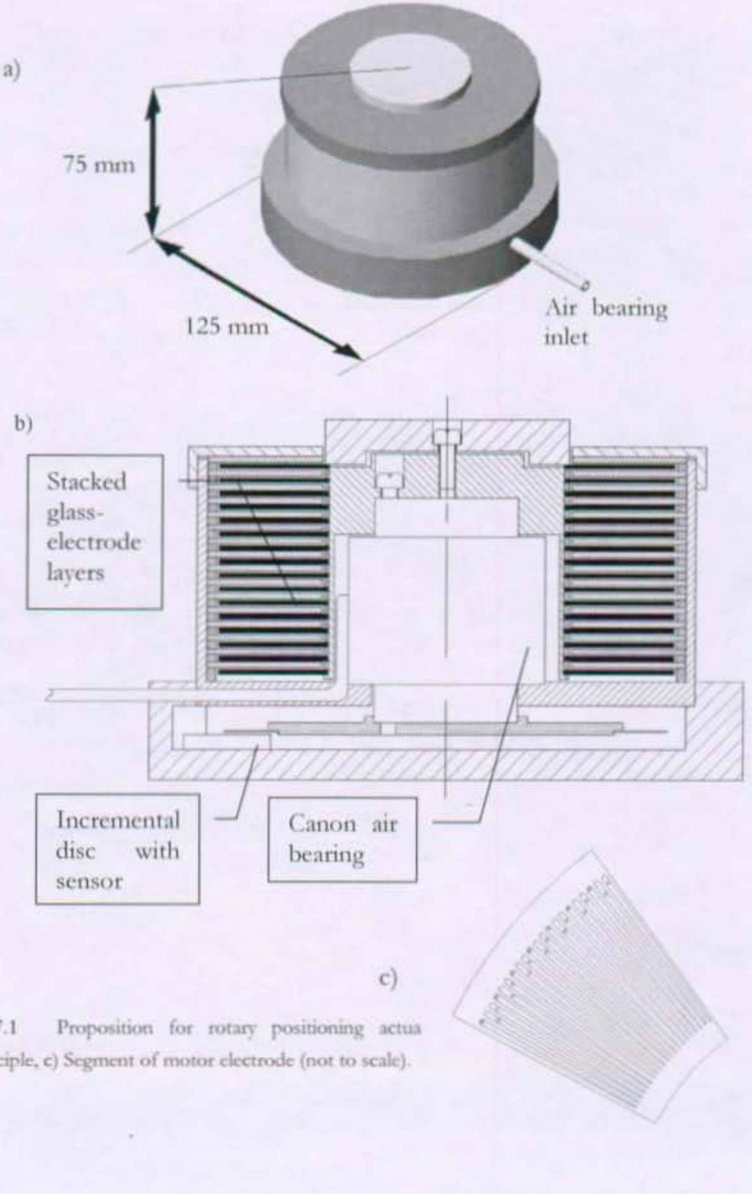

Fig.7.1 Proposition for rotary positioning actua principle, c) Segment of motor electrode (not to scale).

The specifications of such an actuator are calculated as follows:

Motor type:	16 stacked soda-lime glass discs ($Si0_2$ 72%, Na_2O 13%, CaO 11%), double side drive. Air gap g = 100μm
Electrode:	300 tracks (n=300) → 100 poles (m = 100) Inter-track gap d = 400 μm Outer radius R_{out} = 95 mm Inner radius R_{in} = 28 mm Minimal track width w_{in} = 200 μm Breakthrough voltage = 1.2 kV → Applied motor voltage peak to peak = 1kV
Weight:	600 g (estimated)
Inertia:	250 gcm^2
Torque:	44 mNm (equivalent to 4cm x 3cm ironless DC motor)
Top speed:	~ 200rpm (estimation based on top speed achieved with one single glass disc)
Slow speed:	Slower than 10 arc sec / sec (36 hours for one rotation)
Resolution:	Sensor: 0.36 arc second Actuator (open loop, 16bit driver): 0.19 arc second
Range:	Infinite

VIII. Curriculum Vitae

Roland Moser

Born on the 11th of January 1974
Swiss citizen

Education

1999 – 2002	PhD thesis « Precise positioning using the electrostatic glass motor » Laboratory of robotic systems Institute of production and robotics, EPFL
1993 – 1999	Ing. dipl. EPFL in micro-engineering Specialization in robotics, applied optics, control and production
1988 – 1992	Matura type C (science) Gymnasium Oberwil (BL)

Professional experience

2000-2002	Research assistant Laboratory of robotic systems, EPFL, Switzerland
1999 – 2000	Research assistant (Monbusho scholarship) The University of Tokyo, Tokyo, Japan
1998/1999	Master thesis (DARPA project) « Integration of panoramic camera into open agent architecture » NASA, Ames Research Center, CA, USA Stanford Research Institute (SRI), CA, USA
1997	Two months internship (IAESTE scholarship) OMRON Electronics, Kurayoshi, Japan

IX. PUBLICATIONS

Publications of the author during the thesis period.

Journals

Moser R., Higuchi T.
Precise positioning using electrostatic glass motor
Journal of precision engineering, Elsevier, Vol. 26/2, (2002), pp. 163-169

Moser R., Higuchi T.
Electrostatic rotation of glass disc
Journal of electrostatics, Elsevier, Vol. 55/1, (2002), pp. 97-108

Moser R., Sandtner J., Bleuler H.
Diamagnetic suspension system for small rotors
Journal of Micromechatronics, VSB, Vol.1, No. 2, (2001), pp. 131-137

Moser R., Bleuler H.
Precise Positioning Using Electrostatic Glass Motor with Diamagnetically Suspended Rotor
IEEE Transactions on Applied Superconductivity, Vol. 12, No. 1, pp. 937 – 939

Moser R., Barrot F., Sandtner J., Bleuler H.
Diamagnetic levitation for flywheels
International Journal of the JSME, IN PRESS

Moser R., Higuchi T.
Compact One Inch Hard Disc Drive using Electrostatic Glass Motor
Microsystem Technologies, Springer Verlag, SUBMITTED

Moser R., Wüthrich R., Sache L., Higuchi T., Bleuler H.
Characterization of Electrostatic Glass Actuators
Journal of Applied Physics, AIP, SUBMITTED

Conferences

Moser R., Sache L., Higuchi T., Bleuler H.
Advances in fast rotating electrostatic glass actuators
Proceedings of the 6th International Conference on Motion and Vibration Control, Saitama, (2002), pp. 1077 - 1080

PUBLICATIONS

Moser R., Barrot F., Sandtner J., Bleuler H.
Diamagnetic levitation for flywheels
Proceedings of the 8th International Symposium on Magnetic Bearings, Mito, (2002), pp. 599 – 603

Moser R., Barrot F., Bleuler H.
Optimization of two-dimensional permanent magnet arrays for diamagnetic levitation
Proceedings of the 17th International Conference on Magnetically Levitated Systems and Linear Drives (Maglev), Lausanne, (2002), CD-ROM

Moser R., Sandtner J., Bleuler H.
Diamagnetic suspension assisted by electrostatic actuators
Proceedings of the 6th international symposium on magnetic suspension technology, Torino (2001), pp. 241 - 245

Moser R., Sandtner J., Bleuler H.
Electrodynamic suspension for high rotation speed applications
Poster Session, International Conference on Magnet Technology (MT-17) CERN-Geneva, (2001)

Moser R., Hori S., Poh F. L., Higuchi T.
Electrostatic motor bearing combination for glass disc
Proceedings of the International Conference on Machine Automation ICMA2000, Osaka (2000), pp. 243 – 248

Moser R., Higuchi T.
Electrostatic motor bearing combination for glass disc
Proceedings of the 12th Symposium on Electromagnetics and Dynamics, Okinawa (2000), pp. 555 – 558

Hori S., Moser R., Poh F. L., Higuchi T.
Development of electrostatic dielectric disc drive
Proceedings of the 12th Symposium on Electromagnetics and Dynamics, Okinawa (2000), pp. 559 – 564

Boletis A., Vuillemin R., Aymon C., Kümmerle M., Aeschlimann B., Moser R., Bleuler H.
A six magnetic actuators integrated micromotor
Proceedings of the 7th International Symposium on Magnetic bearings, Zurich (2000), pp. 101 - 103

Moser R., Barrot F., Bleuler H.
Optimization of two-dimensional permanent magnet arrays for diamagnetic levitation
Proceedings of the 17th International Conference on Magnetically Levitated Systems
and Linear Drives (Maglev),
ACCEPTED

Moser R., Sache L., Higuchi T., Bleuler H.
Advances in fast rotating electrostatic glass actuators
6th International Conference on Motion and Vibration Control (MOVIC 2002), ACCEPTED

Moser R., Regamey Y. J., Bleuler H.
Passive Diamagnetic Levitation for Flywheels
8th International Symposium on magnetic bearings (ISMB8) 2002,
ACCEPTED

Moser R., Gassert R., Burdet E., Sache L., Woodtli H. R., Erni J., Maeder W., Bleuler H.
An MR Compatible Robotic Technology
IEEE ICRA 2003, SUBMITTED

X. Appendices

10.1 High Voltage Amplifier Stage

Figure 10.1 Photo of the three-channel high voltage amplifier stage

Output Voltage: ± 430 V
Input Voltage: ± 10 V
Bandwidth: 10 kHz
Output power: 6 Watt
Bode diagram:

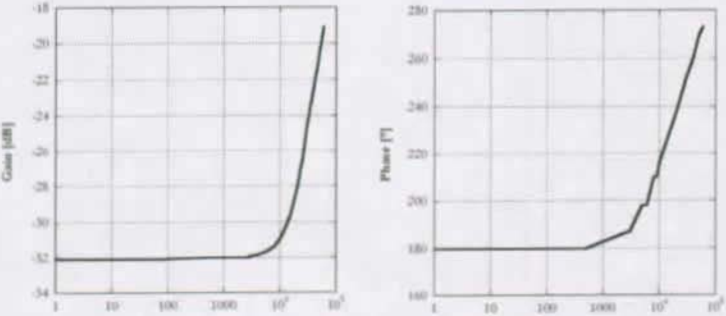

Figure 10.2 Measured Bode diagram of the high voltage amplifier stage

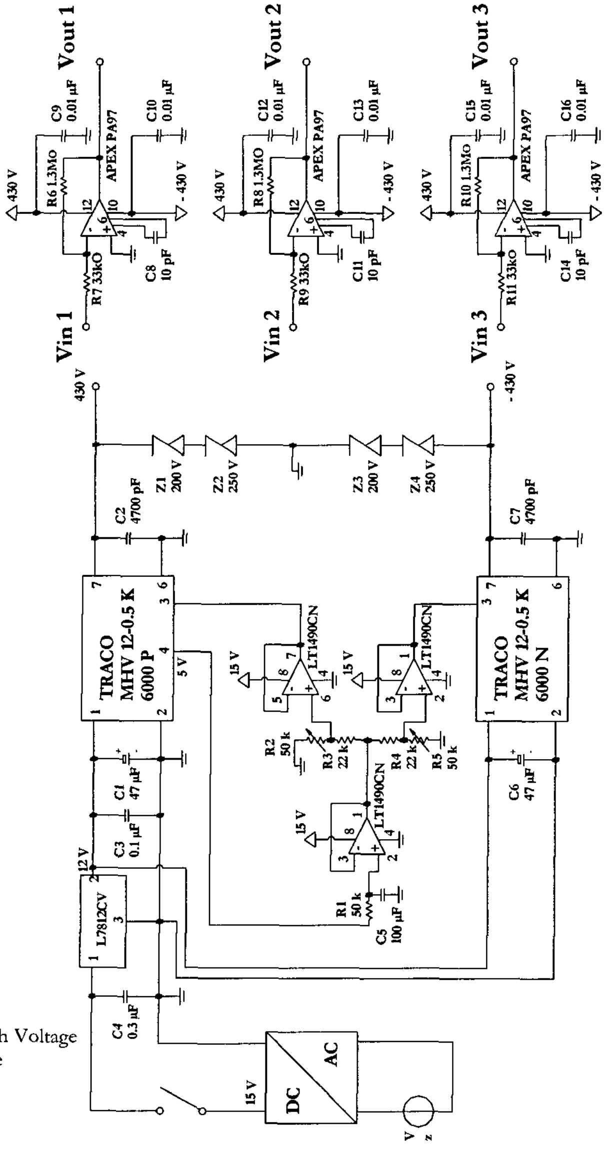

Figure 10.3
Scheme of High Voltage
Amplifier Stage

10.2 Interface and processor unit

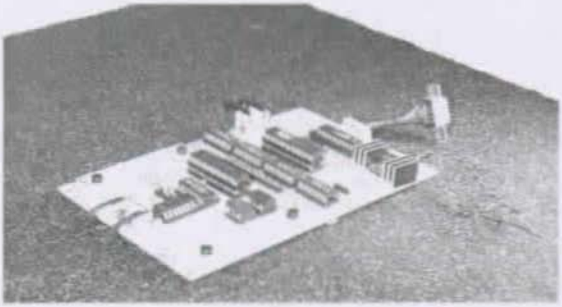

Figure 10.4 Photo of the interface and processor unit

Input: RS 232 serial connection with commercial PC @ 19200 baud

Protocol: 4-byte word: WW XX YY ZZ

WW: number of steps (hex 00-FF)
XX: rotation speed level (hex 00-FF)
YY: rotation direction (hex 00-01)
ZZ: position sensor enable (hex 00-01)

After reception, a '@' character is returned to the PC. If the exact rotor position is requested (ZZ = 01), then a 16 bit word is returned.

Numerik Jena Encoder Kit R sensor cable for position detection. Requested components:

Encoder Kit R with 50 times intepolation
Encoder Disc with 18000 increments

Output: 16 bit parallel address bus, counting up or down with the requested number of impulsions and speed. Returns the rotor position if requested with additional 4x interpolation (200x in total)

Inputs and Outputs

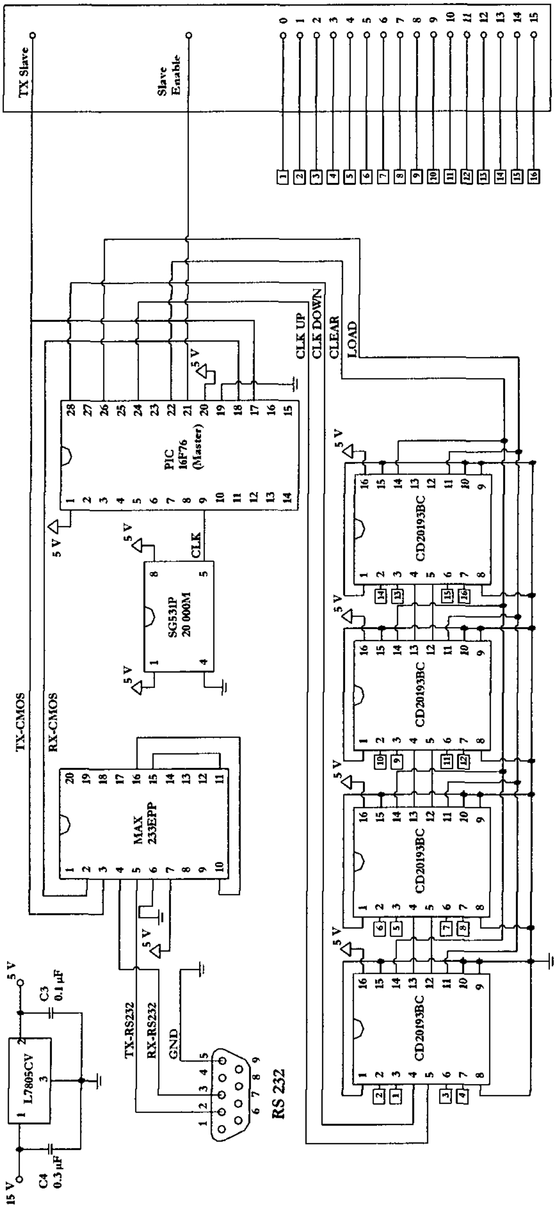

Figure 10.5
Scheme of interface and processor unit without sensor electronics

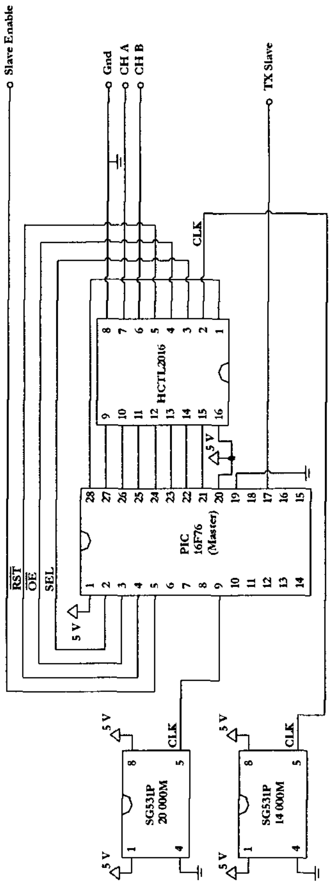

Figure 10.6 Scheme of the position sensor interface circuitry

10.3 Function generator

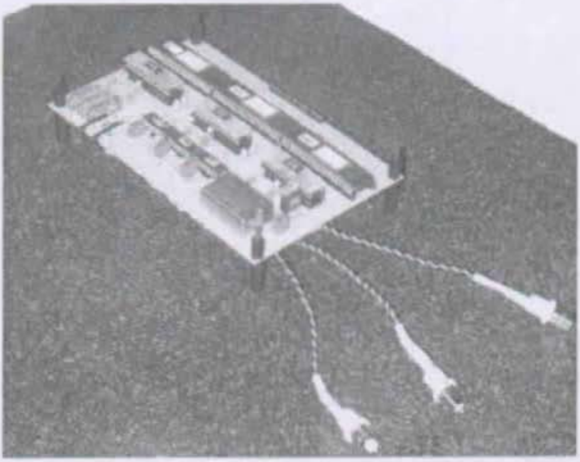

Figure 10.7 Photo of the function generator unit

Input:	16 bit parallel address bus Conversion trigger signal
Output:	3 sine waves, mutually 120° phase shifted. 65536 levels of amplitude. Amplitude ± 10 V
Bandwidth :	DC to 436 Hz
Resolution:	0.2 arc second (in combination with a 90 pole electrode)

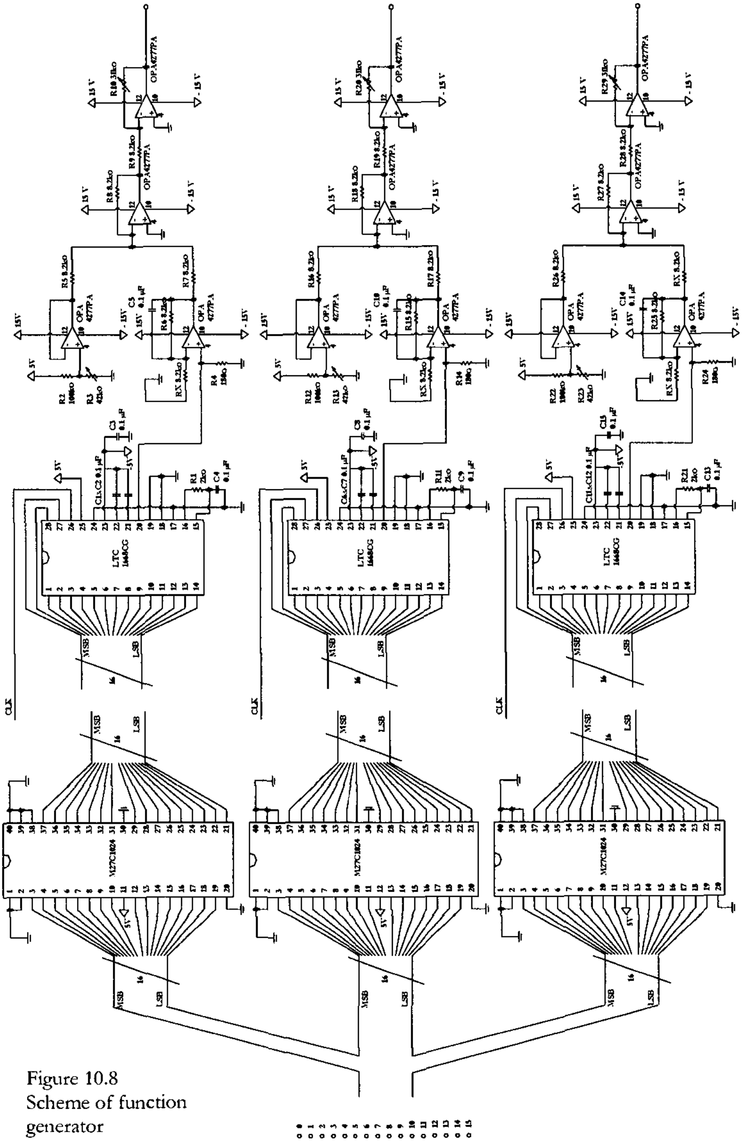

Figure 10.8
Scheme of function
generator

XI References

[1] Adamiak K.
Geometric Identification of Conductors Placed Inside Dielectric Layer Using Boundary Element Method
Boundary Elements XIV, Computation Mechanics Pulication, Elsevier Applied Science, Vol. 1, pp 449-462

[2] Aguet M., Morf J. J.
Traité d'électricité: Energie électrique
Georgi, Ecole polytechnique fédérale de Lausanne, Vol. 12, 1981

[3] Aguet M., Ianovici M.
Traité d'électricité: Haute Tension
Georgi, Ecole polytechnique fédérale de Lausanne, Vol. 22, 1982

[4] Badano F., Bétemps M., Jutard A.
Modelling and control of a robotic actuator using metal bellows
Industrial Automation, Montreal, Canada, (1992), pp. 13.29 – 13.33

[5] Bart S. F., Lang J. H.
Electroquasistatic Induction Motors
Proc. of the IEEE Microelectromechanical systems, (1989), pp. 7 – 12

[6] Bexell M., Johanson S.
A high toque miniature inchworm motor
Proc. of Eurosensors IX, (1995), pp. 69-70

[7] Bland D. R.
The theory of linear viscoelasticity
Pergamon, London, (1960)

[8] Blythe A. R.
Electrical Properties of Polymers
Cambridge University Press, (1979)

[9] Bollée B.
Electrostatic Motors
Philips Technical Review Vol. 30, pp. 178-194

[10] Breedveld P. C.
Multibond graph elements in physical systems theory
J. Franklin Inst., Vol 319, pp. 1-36.

[11] Brissaud M., Dion L., Eyraud L.
Double Action Piezoelectric Motors
4th European Frequency and Time Forum, Neuchatel, Switzerland (1990), pp. 355 – 358

[12] Büchi R., Zesch W., Codourey A., Siegwart R.
Inertial Drives For Micro- and Nanorobots: Analytical Study
SPIE's , Intelligent Systems and Advanced Manufacturing, Philadelphia, (1995)

[13] Calvaer A.
Electromegnétisme: Lois Fondamentales et Electrostatique
Derouaux, Vol.1, (1978)

[14] Cellier F. E.
World Wide Web - The Global Library: A Compendium of Knowledge About Bond Graph Research
http://www.ece.arizona.edu/~cellier/bg.html

[15] Christensen R. M.
Theory of viscoelasticity, an introduction
Academic Press, New York, (1971)

[16] Clark D. H., Clark S. P. H.
Newton's tyranny
Freeman & company, New York, (2001), pp. 156 - 159

[17] Cohen B.
Benjamin Franklin's Experiments
Harvard University Press (1941), pp. 331-338

[18] Choi S. D., Dunn D. A
A surface charge induction motor
Apl. Sci. Res., Vol. 22, (1970), pp. 442 - 448

[19] de Coulomb C. A.
Première Mémoire sur l'Electricité et Magnétisme
Histoire de l'Academie Royale des Sciences Vol. 569 (1785)

[20] Cross J. A.
Electrostatics : Principles, Problems and applications
Adam Hilger, Bristol, (1987), pp.17 – 85

[21] Cubric D., Lencova B., Read F. H.
Comparison of the Finite Difference, Finite Element and Surface Charge Methods for Electrostatic Charges Particle Optics, Electron Microscopy and Analysis.
Institute of Physics Conference Series Vol 153, pp. 91-94

[22] Davies D. K.
Charge generation on dielectric surfaces
Journal of physics, D: Applied Physics, Vol 2, (1969), pp.1533 - 1537

[23] Davis M. H.
Electrostatic field and forces on a dielectric sphere near a conducting plane
Am. J. Phys., Vol. 37, (1969), pp. 26 - 29

[24] Duong, K., Garcia, E.
Design and Performance of a Rotary Motor Driven by Piezoelectric Stack Actuators
Japanese Journal of Applied Physics, Vol. 35 (1996), pp. 6334 – 6341

[25] Durand E.
Electrostatique : Les distributions
Masson et Cie, Vol. 1, (1964)

[26] Durand E.
Electrostatique : Méthodes de calcul diélectriques
Masson et Cie, Vol. 3, (1966)

[27] Durand E.
Electrostatique : Problèmes généraux conducteurs
Masson et Cie, Vol. 2, (1966)

[28] Elliot R. S.
Electromagnetics
IEEE Press, New York, (1993), pp. 193 – 199

[29] Epstein L.
Electrostatic suspension
Am. J. Phys., Vol 22, pp. 406-407

[30] Fallou, B.
Electrostatique : Les phénomènes et leurs implications industrielles
Revue Générale de l'Electricité, No. 10/91, (1991), pp. 63 – 67

[31] Flügge W.
Viscoelasticity
Springer Verlag, Berlin (1975), pp. 21 - 33

[32] Fuhr G.
Über die Rotation dielektrischer Körper in rotierenden Feldern
Habil. Diss., Humboldt Universität zu Berlin, (1986)

[33] Fuhr G.
Linear Motion of Dielectric Particles on Living Cells in Microfabricated Structures Induced by Traveling Electric Fields
IEEE MEMS Workshop 1991, pp. 259-264

[34] von Guericke O.
The new (so-called) Magdeburg experiments
Translation: Glover-Foley, M.
Book II, Chaps. 1-4 & Book III, Individual Experiments
Kluwer Academic publishing (1993), pp. 83-91

[35] Hack T.
Mechanical Modeling and Testing of a stick slip piezoelectric actuator
Master thesis, The University of Cambridge, (1996)

[36] Hagedorn R. G. et al.
Design of Asynchronous Dielectric Micromotors
Journal of Electrostatics Vol. 33, pp. 159-185

[37] Harrison D. E., Moratis Ch. J.
Ceramics, Glasses and Mica
Handbook of Materials and Processes for Electronics
Mc Graw Hill (1970), pp. 6.26-6.34

[38] Hart J., Merrilees P. E.
The viscoelastic effect
Dielectrics, Vol. 1, (1963), pp. 58 - 62

[39] Hilczer B., Malecki J.
Electrets
Elsevier, Warszawa (1986), pp. 19 – 57

[40] Hori S., Moser R., Poh F. L., Higuchi T.
Development of electrostatic dielectric disc drive
Proceedings of the 12th Symposium on Electromagnetics and Dynamics,(2000), pp. 559 – 564

[41] Ida N., Bastos J.P.A
Electromagnetics and Calculation of Fields
Springer-Verlag, (1992)

[42] Ikuta K., Kawahara A., Yamazumi S.
Miniature cybernetic actuators using piezoelectric device
Proceedings of MEMS '91, Nara, (1991), pp. 131-136

[43] Inculet I.I, Castle G. S. P.,
Particle conveying with curvilinear electric fields generated by plane electodes
Journal of Electrostatics, Vol. 17, pp. 95 – 98

[44] Jacobsen S. C., Price R. H., Wood J. E., Rytting T. H. Rafaela M.
The Wobble Motor: An Electrostatic, planetary armature microactuator
Proc. IEEE Microelectromechanical systems (1989), pp. 17 - 24

[45] Jefeminko O. D
Electrostatics and its applications – Electrostatic motors
Chapter 7, Wiley, New York (1973)

[46] Jeon J. U., Higuchi T.
Electrostatic Suspension of Dielectrics
IEEE Transactions on Industrial Electronics Vol. 45, pp. 930-946

[47] Jeon J. U., Higuchi T.
Induction Motors with Electrostatic Suspension
Journal of Electrostatics Vol. 45, pp. 157-161

[48] Jeon J. U., Higuchi T.
Variable Capacitance Motor with Electrostatic Suspension
Sensors and Actuators, Vol. 75, (1999), pp. 289 - 297

[49] Jermendy, L., Paulusz, M.
Electric Characteristics of Ring Electrodes
IEEE Transactions of Power Apparatus and Systems, Vol. 102, (1983), pp. 1437-1444

[50] Jin J., Higuchi T., Kanemoto M.
Electrostatic Levitator for Hard Disk Media
IEEE Transactions on Industrial Electronics, Vol. 42, (1995), pp. 467 - 473

[51] Jin J., Jeon J. U., Higuchi T.
Direct electrostatic Levitation and Propulsion of Silicon Wafer
Proc. of 31st IAS conference, (1996), pp. 62 - 68

[52] Jones T. B.
Lumped parameter electromechanics of electret transducers
IEEE Trans. Acoustics, Speech and Signal Processing, (1975), pp. 141 – 145

[53] Jones T. B.
Electromechanics of paniticles
Cambridge University press, (1995), pp. 74 – 85

[54] Jones T. B., McCarthy M. J.
Electrode geometries for dielectrophoretic levitation of small spheres an shells
Journal of Electrostatics, Vol. 11, pp. 71 - 83

[55] Kingery W.D., Bowen H.K, Uhlmann D.R.
Introduction to Ceramics
Wiley, New York (1976), pp. 874 – 924

[56] Knoebel H. W.
The electric vacuum gyro
Control engineering, Vol. 11, (1964), pp. 70-73

[57] Kooy C.
Torque on a resistive rotor in a quasi electrostatic field
Appl. Sci. Res. 20 (1969), pp. 161-172

[58] Kouklan M. H., Hojat Y., Higuchi T.
Air Impact Drive for Positioning by Pulse and Continuous Air pressure
Journal of Robotics and Mechatronics Vol 11, pp. 263 – 268

[59] Kouklan M. H., Hojjat Y., Higuchi T.
Air Impulsive Drive for Positioning by Pulse Pressure
3rd International Conference on Advanced Mechatroincs ICAM (1998), pp. 626 – 631

[60] Krupp H.
Physical models of the static electrification of solids
11th Static electrification conf., (1971), pp. 1 - 17

[61] Kumar S., Cho D.
A proposal for electrically levitating micro-motor
Sensors and Actuators, Vol. 24, (1990), pp. 141 – 149

[62] Kumar S., Cho D., Carr W. N.
Experimental Study of Electric Suspension for Micro-bearing
Journal of Microelectromechanical systems, Vol. 1, (1992), pp. 23 - 30

[63] Landau L. D., Lifshitz E. M
Electrodynamics of Continuous Media
Addison-Wesley, Reading, MA (1960)

[64] Lawyer J. E., Dyrenforth W. D
Electrostatics and its industrial applications
Wiley, (New York), (1973), chapter 10

[65] Lee E. H.
Viscoelastic stress analysis
Proceedings of 1st symposium on naval structure mechanics, Stanford, (1958), pp. 456 - 482

[66] Mascart M. E.
Traité D'Électricité Statique
Libraire de L'Adémie de Médecine, Paris, (1976)

[67] Matsubara T., Yamaguchi M., Minami K. Esahi M.
Stepping electrostatic microactuator
Proc. 7th Int. Conf. On Solid State Sensors and Actuators, (1995), pp. 50 - 53

[68] Maxwell J. C.
The Scientific Papers of the Honorable Henry Cavendish
Cambridge University Press (1921), pp. 118 et seq.

[69] Mizuno T., Araki K..,
Frequency feedback electric suspension
Proceedings of the 32nd SICE annual conference, (1993), pp. 1369 – 1372

[70] Montgomery D. J.
Static electrification of solids
Solid State Physics, Vol. 9, (1959), pp. 139 - 196

[71] Morita T., Yoshida R., Okamoto Y., Kurosawa M., Higuchi T.
A Smooth Impact Rotation Motor Using a Multi-Layered Torsional Piezoelectric Actuator
IEEE Transactions on Ultrasonics, Vol. 46 (1999), pp. 1439 – 1445

[72] Moser R., Higuchi T.
Precise positioning using electrostatic glass motor
Journal of precision engineering, Elsevier, Vol. 26/2, pp. 163-169

[73] Moser R., Higuchi T.
Electrostatic rotation of glass disc
Journal of electrostatics, Elsevier, Vol. 55/1, pp. 97-108

[74] Moser R., Sandtner J., Bleuler H.
Diamagnetic suspension assisted by electrostatic actuators
Proceedings of the 6th international symposium on magnetic suspension technology, Turin, (2001), pp. 241 - 245

[75] Moser R., Hori S., Poh F. L., Higuchi T.
Electrostatic motor bearing combination for glass disc
Proceedings of the International Conference on Machine Automation ICMA2000, (2000), pp. 243 – 248

[76] Moser R., Higuchi T.
Electrostatic motor bearing combination for glass disc
Proceedings of the 12th Symposium on Electromagnetics and Dynamics,(2000), pp. 555 – 558

[77] Niino T., Egawa S., Kimura H., Higuchi T.
Electrostatic Artificial Muscle : Compact, High-Power Linear Actuators with Multiple-Layer Structures
Proc. IEEE Micro Electro Mechanical Systems Workshop, (1994), pp. 130-135

[78] Niino T., Higuchi T., Egawa S.
Dual Excitation Multiphase Electrostatic Drive
Conference Record of the 1995 IEEE Industry Applications Society Annual Meeting, (1995), pp. 1318-1325

[79] Osakabe M., Kurosawa T., Higuchi T., Shinoura O.
Surface acoustic wave linear motor using silicon slider
Industrial Automation, Montreal, Canada, (1992), pp. 13.29 – 13.33

[80] Osakabe M., Kurosawa T., Higuchi T., Shinoura O.
Surface acoustic wave linear motor using silicon slider
Proc. of IEEE Workshop on MEMS, Heidelberg, (1998)

[81] Otter den M.W.
Approximate expressions for the capacitance and electrostatic potential of interdigitated electrodes
Sensors and Actuators, Vol. A 96, (2002), pp. 140-144

[82] Paschen F.
Electrostatic breakdown in gases
Ann. Physik, vol 37, (1889), p. 69

[83] Péclat C.
Conception et realization d'un micro-moteur piezoelectriqe
Thèse No. 1434, EPFL, 1995

[84] Poh F. L.
Research on electrostatic suspension and propelling of glass plate
PhD thesis, Department of precision engineering
The University of Tokyo (1999)

[85] Ragulski K., Bansevicius R., Baraukas R., Kulvietis G.
Vibromotors for precision microrobots
Hemisphere publishing corporation, New York, (1998)

[86] Robert P.
Traité d'Electricité : Matériaux de l'Electrotechnique
Georgi, Ecole polytechnique fédérale de Lausanne, Vol. 2, (1979)

[87] Rhim W.K, Collender M. T., Hyson M. T., Simms W. T., Elleman D. D.
Development of an electrostatic positioner for space material proccessing
Rev. Sci. Instrum. Vol 56, pp. 301-317

[88] Salvino D.J, Rogge S., Tigner B, Osheroff D.D.
Low Temperature AC Dielectric Response of Glasses to High DC Electric Fields
Physical Review Letters, Vol. 73, pp. 268 – 271
[89] Secker P. E., Scialom N.
A simple liquid-immersed dielectrid motor
Journal of applied physics, Vol. 39, (1968), pp. 2957 - 2961

[90] Sezako M, Nagayasu I., Sato H.
Electrostatic holding device for recording paper
GB Patent Specification 1224155, (1971)

[91] Schurmann P. F.
Historia de la Fisica
Editorial Nova, Buenos Aires, (1945)

[92] Sessler G.M., West J. E.
Electret transducers : a review
J. Acoust. Soc. Am. 35 (1973), pp. 1589 - 1595

[93] Shames H.
Mechanics of fluids
Mc Graw Hill, Tokyo (1969), pp. 300-377

[94] Shinbrot T.
A look at charging mechanics
Journal of electrostatics, Vol. 17, pp. 117 - 125

[95] Tada Y.
Electret motor having rotor employing plastic substrate
Jpn. Journal of applied physics, Vol. 33, (1994), pp. 1394 - 1396

[96] Trimmer W., Jebens R.
An operational harmonic electrostatic motor
Proc. IEEE Microelectromechanical systems (1989), pp. 13-16

[97] Ubink J.
Optimization of the rotor surface resistance of the asynchronous electrostatic motor
Appl. Sci. Res. 22 (1969), pp. 161-172

[98] Umé M.
Modélisation tridimensionnelle du champ électrique dans les structures non-linéaires
Thèse, (1995), Université de Liège

[99] Woodson H. H., Melcher J. R.
Electromechanical Dynamics
Chapter 3, Wiley, New York (1968)

[100] Yamamoto A., Niino T, Higuchi T.
High Power Electrostatic Actuator with Novel Electrode Design
Proc. IEEE Micro Electro Mechanical Systems Workshop '98, (1998), pp. 408-413

XII. Notations

Symbol	**Description**	**MKS unit**	
A	Surface of glass		[m^2]
B	Magnetic flux density	[Tesla]	[Wb/m^2]
C	Capacitance	[Farad]	[C/V]
D	Electric displacement vector		[C^{2}V/Nm^3]
D	Damping coefficient		[Ns/m]
D	Width of electrode pole		[m]
E	Electric field		[V/m]
F	Force		[N]
H	Height of actuator		[m]
I	Current	[Amp]	[C/s]
K	Stiffness		[N/m]
K	Width of glass slider		[m]
K	Constant		
L	Length of electrodes		[m]
N	Number of dipoles per volume		[1/m^3]
P	Power	[Watt]	[kgm^2/s^3]
P	Electric polarization		[C^{2}V/Nm^3]
Q	Charge		[C]
R	Resistance	[Ohm]	[s/cm]
R	Radius		[m]
T	Torque		[Nm]
T	Specific time		[s]
V	Voltage		[V]
W	Energy	[Joule]	[kgm^2/s^2]
d	Inter-electrode gap		[m]
f	Force density		[N/m^2]
f	Clock frequency	[Hertz]	[1/s]
g	Air gap		[m]
h	Thickness of glass rotor		[m]
k	Displacement coefficient		
m	Number of poles		
m	Mass		[kg]
n	Number of electrode tracks		
n	Number of stacked electrodes		
n	Digital resolution		[bit]

NOTATIONS

q	Charge		[C]
r	Radius		[m]
t	Time		[s]
v	Speed		[m/s]
w	Energy density		[kg/ms^2]
x	Distance		[m]
x	Horizontal Cartesian displacement		[m]
y	Horizontal Cartesian displacement		[m]
z	Vertical Cartesian displacement		[m]
α	Power law constant		
δ	Displacement		[m]
ε	Permittivity		[C^2/Nm^2]
ϕ	Multiplication factor		
γ	Length of flux line trajectories		[m]
η	Multiplication factor		[m]
η	Viscosity		[Ns/m^2]
η	Efficiency		[%]
κ	Relative dielectric constant		
μ	Magnetic permeability		[Wb/Am]
θ	Approximated function		
ρ	Density		[kg/m^3]
σ	Stress	[Pascal]	[N/m^2]
τ	Time constant		[s]
ζ	Resolution		[m]
Γ	Characteristic length		[m]
ϑ	Angular deviation		[deg]
Λ	Constant		